Development of High Power CEP-Stable Light Sources

Maximilian Fabian Seeger

München 2023

Development of High Power CEP-Stable Light Sources

Maximilian Fabian Seeger

Dissertation
an der Fakultät für Physik
der Ludwig–Maximilians–Universität
München

vorgelegt von
Maximilian Fabian Seeger
aus Baden-Baden

München, den 01.08.2023

Erstgutachter: Prof. Matthias F. Kling
Zweitgutachter: Prof. Caterina Vozzi
Tag der mündlichen Prüfung: 11.09.2023

Zusammenfassung

Die Erzeugung und Verstärkung von Lichtpulsen mit Pulsenergien von mehreren mJ, Pulsdauern von wenigen Zyklen und einer stabilen Träger-Einhüllenden-Phase (CEP) ist eine Schlüsseltechnologie der modernen Laserphysik. In der Starkfeld- und Attosekundenphysik werden solche Pulse benötigt, um die effiziente Erzeugung von höheren Harmonischen und isolierten Attosekundenpulsen zu ermöglichen. Die verbreitetsten Treiber-Lichtquellen für Attosekundenexperimente sind dabei Laser basierend auf Titan-dotiertem Saphir als Lasermedium. Diese Lasersysteme sind jedoch auf eine mittlere Leistung von wenigen zehn Watt begrenzt. Attosekundenexperimente basierend auf diesen Lasern können daher nur bei niedrigen Wiederholraten im Bereich von einigen kHz betrieben werden. Diese Einschränkung beförderte die Entwicklung von Hochleistungslasern auf Basis von Ytterbium-dotiertem Yttrium-Aluminium-Granat (Yb:YAG). Diese können Leistungen im Bereich von kW liefern. Daher ermöglichen sie eine effiziente Erzeugung von Attosekundenpulsen selbst bei Wiederholraten ≥ 100 kHz. Systeme, die eine ausreichende Pulsenergie, hohe Wiederholraten und CEP-stabile Pulse vereinen, sind jedoch kaum verfügbar, was einen flächendeckenden Einsatz zur Erzeugung von Attosekundenpulsen verhindert. Dagegen sind Yb:YAG-Laser gepumpte, optisch-parametrische Verstärker weit verbreitete Systeme für Attoskeundenexperimente. Sie ermöglichen eine breitbandige Verstärkung von Pulsen zu Energien von mehreren mJ. Die erreichbare Leistung dieser Systeme ist allerdings durch die niedrige Konversionseffizienz des parametrischen Prozesses beschränkt.

Diese Arbeit behandelt die genannten Einschränkungen für den Einsatz von Yb:YAG basierten Lichtquellen für Attosekundenexperimente bei hohen Wiederholraten. Für den direkten Einsatz in der Erzeugung von Attosekundenpulsen wurde ein nichtlinearer regenerativer Yb:YAG Scheibenlaser für die direkte Verstärkung von CEP-stabilen Pulsen entwickelt. Dieses Lasersystem erreicht Pulsenergien von über 2 mJ bei einer Wiederholrate von 100 kHz und Pulsdauern von unter 200 fs. Die CEP-Stabilität der Pulse geht jedoch beim Verstärkungsprozess verloren. Diese Arbeit befasst sich mit der Untersuchung der Mechanismen die zum Verlust der CEP-Stabilität beitragen.

Des Weiteren wurde ein Hochleistungs-OPCPA-Aufbau entwickelt, der von einem Yb:YAG Scheibenlaser gepumpt wird. Dieses Lasersystem mit eine Zentralwellenlänge von 2.1 μm liefert Lichtimpulse mit einer Dauer von 20 fs, einer Pulsenergie von mehr als 5 mJ bei einer Wiederholrate von 10 kHz. Durch passive und aktive Stabilisierungsmechanismen wird das CEP-Rauschen in diesem System auf 100 mrad begrenzt. Diese Parameter, in Verbindung mit der exzellenten Leistungsstabilität, machen dieses Lasersystem zu einer hervorragenden Treiberquelle für Attosekundenexperimente mit Photonenenergien im Bereich der weichen Röntgenstrahlung.

Abstract

The generation and amplification of light pulses with multiple mJ of pulse energy, few-cycle pulse durations, and a stable carrier-envelope-phase (CEP) is a key aspect of modern laser science. In strong-field and attosecond science, these pulses are required for efficient high-harmonic generation, and for the generation of isolated attosecond pulses. The most commonly used driving light sources for attosecond experiments are lasers based on titanium-doped sapphire as active laser medium. However, these lasers systems have limited output power capabilities of a few tens of watts. Therefore, the pulse energies required for efficient generation of attosecond pulses can only be achieved at low repetition rates typically in the few kHz range. This limitation promoted the development of infrared pump lasers based on ytterbium doped yttrium-aluminum-garnet (Yb:YAG). These systems can provide kW-level output powers allowing for high pulse energies even at repetition rates beyond 100 kHz. However, their direct use for isolated attosecond pulse generation is not common. The few existing experiments are limited to low repetition rate systems. This is due to a lack of CEP-stable few-cycle sources delivering sufficiently high pulse energies at repetition rates $\geq$ 100 kHz. Yb:YAG pumped optical parametric chirped pulse amplification (OPCPA) setups, however, are common driving sources for attosecond experiments. These systems provide broadband amplification to multi-mJ pulse energies but their output power is limited due to the low pump-to-signal conversion efficiency.

The research and development work that was part of this thesis addresses these two major limitations for the use of Yb:YAG based driving lasers for attosecond science at high repetition rates. I present two infrared laser sources based on Yb:YAG meant to drive experiments with isolated attosecond pulses. The first light source is a nonlinear regenerative Yb:YAG thin-disk amplifier for the direct amplification of CEP-stable pulses. This setup delivers pulse energies of more than 2 mJ at 100 kHz repetition rate with pulse durations below 200 fs. The CEP-stability of the seed pulses, however, was lost during the amplification process. In this thesis, the CEP-distortion mechanisms in nonlinear regenerative thin-disk amplifiers are investigated.

The second light source is a self-seeded, high power OPCPA setup, which is pumped by a kW-class regenerative Yb:YAG thin-disk amplifier. This short-wavelength infrared (SWIR) source, centered at 2.1 μm delivers 20 fs pulses with up to 5.1 mJ energy at 10 kHz repetition rate. The CEP of the pulses is stabilized to an rms CEP noise of 100 mrad with a hybrid concept relying on a passively CEP-stable seed generation and an active slow-loop CEP control. These parameters in conjunction with the excellent average power stability make this SWIR setup an outstanding driving source for HHG with photon energies in the water window region.

Contents

List of Figures

List of Tables

Acronyms

ASE amplified spontaneous emission. 2

ATI above-threshold ionization. 34

BBO β-barium borate. 27, 34, 41, 43, 44, 48, 61, 62, 70, 71, 73, 74, 86

BiBO bismuth triborate. 29, 69, 71, 73, 74, 81, 82

CEO carrier-envelope-offset-frequency. 13

CEP carrier-envelope-phase. v, 3, 4, 13, 14, 23, 25, 34, 35, 37, 39–43, 47–57, 59–66, 69, 70, 72, 83, 86–93

CM chirped-mirror. 47

CPA chirped pulse amplification. 1, 13, 17, 18, 25, 39, 40, 42, 43, 48, 64, 66, 91

DFG difference frequency generation. 4, 24, 25, 65, 69, 71, 90

EOS electro-optic-sampling. 14

FBG fiber-Bragg-grating. 67

FROG frequency-resolved optical gating. 33, 34, 83–85

FWHM full-width-half-maximum. 10, 18

GDD group delay dispersion. 12, 18, 83

GVD group velocity dispersion. 12, 31, 35, 83

HCF hollow-core fibers. 47, 93

HHG high harmonic generation. 2–4, 14, 39, 42, 65, 77–79, 83, 84, 90, 93

HNF highly nonlinear fibers. 23, 48, 49

KTA potassium titanyle arsenate. 71, 74, 75

LASER Light Amplification by Stimulated Emission of Radiation. 1

LBO lithium triborate. 70, 71, 83

LNB magnesium doped lithium niobate. 27, 32, 69, 71, 74, 75, 79–82, 84, 85, 88, 90

MASER Microwave Amplification by Stimulated Emission of Radiation. 1

MIR mid infrared. 66

NIR near infrared. 64

OPA optical parametric amplification. 3, 25–27, 29–32, 65, 68, 69, 71, 73–86, 88–92, 94

OPCPA optical parametric chirped pulse amplification. 3, 4, 23, 25, 32, 35, 65–73, 75, 80, 81, 86, 90–94

OPO optical parametric oscillators. 1

rms root mean square value. 4, 37, 38, 44, 45, 49, 51, 52, 54–56, 58, 65, 67, 68, 75, 76, 86–89, 92

RTP rubidium titanyl phosphate. 41, 67

SC supercontinuum. 69–71

SFG sum-frequency generation. 24

SHG second harmonic generation. 1, 24, 33–35, 46, 48, 68, 69, 71, 83–86

SI silicium. 44

SPM self-phase-modulation. 21–23, 44–46, 61

SWIR short-wavelength infrared. 3, 4, 23, 25, 32, 35, 65, 66, 68–79, 81–86, 88, 90–94

SXR soft x-ray. 2, 3, 65, 86, 91–93

TD thin-disk. 2

TEM transversal electromagnetic modes. 7

TFP thin-film-polarizer. 41

Ti:sapphire titanium doped sapphire. 1–3, 15, 17, 39, 93

TOD third order dispersion. 13, 83, 90

XUV extreme ultraviolet. 2

YAG yttrium-aluminum-garnet. 15, 63

Yb:YAG ytterbium doped yttrium-aluminum-garnet. 2–4, 9, 15, 16, 39–43, 45, 48, 57, 61, 63–68, 91

YCOB yttrium calcium oxyborate. 71, 74, 75, 90

ZnSe zinc selenide. 77, 83

List of Publications

- M. F. Seeger, D. Kammerer, J. Blöchl, M. Neuhaus, V. Pervak, T. Nubbemeyer and M. F. Kling, "49 W Carrier-Envelope-Phase-Stable Few-Cycle 2.1 μm OPCPA at 10 kHz", Optics Express 31.15 (2023): 24821-24834
- M. F. Seeger, D. Kammerer, J. Blöchl, T. Nubbemeyer and M. F. Kling, "35W Carrier-Envelope-Phase-Stable Few-Cycle Mid- Infrared OPCPA at 10 kHz", CLEO: Science and Innovations, STu4H–3, Optica Publishing Group, (2023)
- M. Neuhaus, H. Fuest, M. F. Seeger, J. Schötz, M. Trubetskov, P. Rusbueldt, H. Hoffmann, E. Riedle, Z. Major, V. Pervak, M. F. Kling and P. Wnuk, "10 W CEP-stable few-cycle source at 2 μm with 100 kHz repetition rate". Opt. Exp. 26, 16074–16085. (2018)

Chapter 1

Introduction

Few technological advancements in recent history can rival the impact the development of the laser had on science and our society as a whole. The stimulated emission of radiation was first predicted by Albert Einstein in 1917 [1]. However, it took more than three decades before a source of coherent radiation based on Microwave Amplification by Stimulated Emission of Radiation (MASER), was first experimentally realized by C. H. Townes et al. [2] in 1954. In the year 1960, Maiman demonstrated a flash-lamp pumped ruby crystal, emitting coherent radiation at optical frequencies [3]. This device was the first light source based on Light Amplification by Stimulated Emission of Radiation (LASER). The significance of the laser quickly became evident. Following the first demonstration, laser technology quickly began to spread. It initiated a multitude of scientific discoveries and technological innovations in medicine [4], biology [5], astronomy [6], chemistry[7] and material science [8, 9]. Today, there is hardly a field of science and technology imaginable without laser technology and its applications reach far beyond the field of optics and photonics. Laser technology also considerably transformed the world we live in. It constitutes the back-bone of our glass fiber based digital infrastructure [10]. Laser based material processing and diagnostics tools, such as extreme ultraviolet lithography, are a driving source behind the ever decreasing size of semiconductor transistor elements [11].

With the laser, for the first time in history, light fields of sufficient intensity to drive a multitude of nonlinear processes were available. In 1961, shortly after the first laser systems were developed, Franken et al. investigated second harmonic generation (SHG) from quartz crystals [12]. This experiment marks the birth of the field of nonlinear optics. Soon, a whole variety of nonlinear processes became available allowing e.g. light sources based on optical parametric oscillators (OPO) [13]. Henceforth, the field of nonlinear optics coevolved with ultrafast laser science. Ultrafast science benefited from nonlinear frequency-mixing, parametric amplification and spectral broadening techniques. In turn, the high intensities available from ultrashort light pulses made driving higher order nonlinear processes viable. Modern ultrafast science was shaped by three major developments. With the invention of chirped pulse amplification (CPA), multi-mJ pulse energies became available at repetition rates > 1 kHz [14]. The development of titanium doped sapphire (Ti:sapphire) based laser systems [15], enabled direct generation of pulses with $\sim$ 20 fs duration due to the large gain bandwidth of the active medium[16]. Ultrafast science based on Ti:sapphire technology enabled experiments with unprecedented temporal resolution

in physics, chemistry, and biology [17, 18]. Finally, the development of nonlinear spectral broadening techniques made a pulse compression to few-cycle durations viable. Ultrashort light pulses emitted from laser systems relying on these technologies are among the shortest events ever created by human kind. The high pulse energies and near-single-cycle durations available from these systems allowed to drive highly nonlinear multi-photon processes in gas targets which resulted in high harmonic generation (HHG)[19, 20]. The photon energies of these harmonics can reach into the soft x-ray (SXR) region. The fundamental physics behind the process of HHG with light pulses at optical frequencies was explained in terms of a simple three step model[21, 22]. According to this model, electrons from a gas target get tunnel-ionized by the strong electric field of an intense ultrashort light pulse. The free electrons are then accelerated by the light field. In the strong electric field of the light pulse, the electrons can reach very high kinetic energies. Due to the periodic nature of the light field, the trajectories of these high kinetic energy electrons can bring them close to their parent ions. Upon recombination a high energy photon is emitted. The cutoff energy of the photons generated by this process depends on the ponderomotive energy $U_\mathrm{p} = E^2/4\omega^2$ of the driving light pulse where E is its field strength and ω its frequency. In 2001, evidence was found that the extreme ultraviolet (XUV) light produced by HHG was emitted in form of a train of attosecond pulses [23]. In the same year, the first isolated attosecond (1 as $= 1 \cdot 10^{-18}$ s) pulse was generated by HHG [24], heralding the field of attosecond science [25]. Nowadays, pulses with spectral coverage ranging from the XUV to the SXR region and pulses as short as 43 attoseconds [26] have been generated. These pulses allow for the study of electron dynamics in gases, solids and nanostructures with unprecedented temporal resolution [27]. Gaining insight into fundamental electronic motion on these time scales might pave the way for a further revolution in digital information processing in PHz-electronics [28, 29].

For many years, Ti:sapphire based laser systems constituted the back-bone of ultrafast and attosecond science. However, power scaling of Ti:sapphire-lasers beyond few tens of Watts proved to be challenging. The large quantum defect [30], short laser level lifetime and parasitic amplified spontaneous emission (ASE) [31] limit its output power capabilities. Last but not least, further power scaling is impeded by a lack of suitable high power pump sources for the laser material. Thus, high pulse energies are achievable only at lower repetition rates. The limitations of Ti:sapphire laser systems have recently promoted the development of high power lasers based on ytterbium doped yttrium-aluminum-garnet (Yb:YAG). These laser systems are capable of delivering kW-scale power levels based on regenerative thin-disk (TD) amplifier [32], Innoslab [33], or large mode area fiber [34] approaches. However, Yb:YAG lasers exhibit a low gain bandwidth [35]. Thus, the achievable pulse duration is typically limited to $\geq$ 400 fs [36]. This limitation can be overcome by nonlinear spectral broadening techniques which increase the spectrum of the output pulses beyond the limited gain bandwidth of Yb:YAG-sources. Thus, a reduction of the pulse duration to the few-cycle-regime is viable[37, 38]. The advent of Yb:YAG laser sources also offered new prospects to attosecond science. The high pump powers available from these systems allow for multi-mJ pulse energies at repetition rates beyond 100 kHz. Therefore, higher flux and faster data acquisition rates could be achieved by employing Yb:YAG driver sources in attosecond experiments. However, the pulses from Yb:YAG oscillators or amplifiers are not widely used directly for the generation of isolated attosecond

pulses. This is partially due to the less straightforward compression to near-single-cycle durations as compared to Ti:sapphire-based systems. One main reason, however, is the general lack of CEP stable sources with multi-mJ pulse energies which prevents the generation of isolated attosecond pulses [39]. Pushing towards the development of high pulse energy, high repetition rate, CEP-stable Yb:YAG amplifiers is one of the purposes of this work.

Despite being rarely used directly as a pump source for HHG in attosecond beam lines, Yb:YAG lasers are commonly used in attosecond science. The high average powers and pulse energies achievable with this technology makes Yb:YAG lasers well suited to pump optical parametric chirped pulse amplification (OPCPA) setups. In a degenerate optical parametric amplification (OPA) process, the picosecond pulses from an Yb:YAG-amplifier can be used to amplify short-wavelength infrared (SWIR) pulses close to the degeneracy point at 2.06 μm with amplification bandwidth supporting few-cycle pulses. Typically, only 10 to 20 % of the available pump energy can be converted to the amplified beam. Therefore, the achievable output power from OPCPA setups is considerably reduced in comparison to the output directly from Yb:YAG sources. However, the large average power potential of Yb:YAG lasers makes power scaling of the OPCPA concept beyond the capabilities of Ti:sapphire based systems feasible. Furthermore, the OPCPA approach offers an additional benefit of having a higher central wavelength. This can be especially beneficial for attosecond spectroscopy experiments as it allows for generating high harmonics with higher photon energies due to the λ^2-scaling of the cutoff energy. This makes experiments with SXR photon energies in the water window between the carbon K-edge at ~ 280 eV and the oxygen K-edge at ~ 530 eV viable.

The development of driving laser sources for the next generation of attosecond experiments was the main goal of this thesis. I will first discuss the fundamental properties of light relevant for this thesis in chapter 2. This chapter, will give a brief introduction into the physics of propagating beams of light and ultrashort light pulses. I will proceed by describing its linear and nonlinear interaction with matter and the means by which ultrashort pulses of light can be generated and characterized. A special focus will be on the amplification of light pulses in Yb:YAG thin-disk amplifiers as well as by parametric amplification.
Following the discussion of the fundamental theoretical framework, I will present two laser systems based on Yb:YAG technology which were developed as part of this thesis. These laser systems are meant to drive attosecond experiments and thus require multi-mJ pulse energies, few-cycle durations and a stable CEP. In chapter, 3.2 I will present a nonlinear Yb:YAG thin-disk regenerative amplifier for the direct amplification of ultrashort CEP-stable pulses at 100 kHz repetition rate. This laser system is capable of delivering 200 fs pulses with $>$ 2 mJ pulse energy at a center frequency of 1030 nm. Therefore, these pulses are well suited for further nonlinear compression to few-cycle pulse durations. However, the CEP stability of the seed pulses is lost during the amplification process. Using this laser setup in attosecond and strong field experiments would thus require tagging of the CEP. After discussing its characteristic output performance, I will elaborate on the CEP distortion mechanisms limiting CEP-stability in the nonlinear amplifier approach. The insight gained from this investigation might contribute to the future development of CEP-stable high pulse energy, high repetition rate Yb:YAG amplifiers.

In chapter 4, a self-seeded CEP-stable, few-cycle SWIR OPCPA setup based on an Yb:YAG thin-disk pump source is presented. This light source delivers pulses with energies beyond 5 mJ at 10 kHz repetition rate. The an average power exhibits root mean square value (rms) fluctuations of $\leq$0.8 % for multiple hours of operation. On the basis of the results achieved with this laser setup, I analyse the limiting factors and the scaling potential of high power SWIR OPCPA setups. The CEP of the amplified SWIR-pulses is stabilized in a hybrid concept relying on passive and active stabilization mechanisms. The passively CEP-stable seed generation by difference frequency generation (DFG) is complemented by an active slow-loop CEP-drift compensation. The active stabilization relies on a highly stable 3f-4f-interferometer for the measurement of the relative CEP. This device has been developed as part of this thesis and proved to exceed the performance of commonly used f-2f-interferometers. The excellent stability performance in terms of average power and CEP-stability make this laser setup an outstanding driving source for HHG and the generation of isolated attosecond pulses.
The findings of the previous chapters are summarized in chapter 5. Furthermore, I will discuss future applications and the prospects for further scaling of the pulse energy and bandwidth of the presented OPCPA setup.

Chapter 2

Theory of Ultrashort Light Pulses

In this chapter I will discuss the fundamental laws of the propagation of light and the linear and nonlinear interaction of ultrashort light pulses with matter relevant for this thesis. I will start by introducing the general propagation equation and its most relevant solutions.

2.1 Fundamental Properties of Light

The behaviour of electromagnetic waves is generally described by Maxwell's equations. From this set of equations one can deduce a partial differential equation called the wave-equation, which describes the propagation of traveling or standing waves in space and time. For electro-magnetic waves in vacuum, this equation takes the form shown in Eq. 2.1 [40, p.78 ff.]

$$\nabla \mathbf{E}(\mathbf{r},t) - \frac{1}{c^2}\frac{\partial^2 \mathbf{E}(\mathbf{r},t)}{\partial t^2} = 0\ . \tag{2.1}$$

Here, c denotes the velocity of light in vacuum, ∇ is the Nabla-operator. Assuming wave propagation along the z-axis, the most simple solution to the wave equation are plane waves with an electric field given by $E(\mathbf{z},t) = A_0 \exp i(\mathbf{kz} - \omega t + \phi)$. Many properties of light can be described in terms of these simple harmonic oscillations with amplitude A_0, wave-vector k, oscillation frequency ω and phase ϕ.

Notably, the sum of an arbitrary number of solutions to Eq. 2.1 is again a solution to the wave equation. This property of electro-magnetic waves is called the superposition principle [40, Sec. 7]. The superposition principle allows to construct other solutions to the wave equation from sums of harmonic waves.

Especially relevant for this thesis are wave packets in time, called light pulses. Such light pulses can be described by an integral over harmonic waves (see Eq. 2.26). According to the superposition principle, these pulses are therefore also solutions to Eq. 2.1.

Another important property of light when considering the sum of electro-magnetic fields is interference. This effect is caused by the phase term ϕ in the description of the harmonic waves. The superposition of two harmonic waves $\mathbf{E}_1(\mathbf{r},t) = A_1 e^{i(\mathbf{k}_1\cdot\mathbf{r}_1 - \omega_1 t + \phi_1)}$ and $\mathbf{E}_2(\mathbf{r},t) = A_2 e^{i(\mathbf{k}_2\cdot\mathbf{r}_2 - \omega_2(t+\tau_\mathrm{d}) + \phi_2)}$ is generally described by Eq. 2.2 [40, p.628 ff.]

$$I = I_1 + I_2 + 2\sqrt{I_1 I_2}\cos\left(\mathbf{k}_1\cdot\mathbf{r}_1 - \omega_1 t + \Phi_1 - \mathbf{k}_2\cdot\mathbf{r}_2 + \omega_2(t+\tau_\mathrm{d}) - \Phi_2\right)\ . \tag{2.2}$$

Here, $I_1 = |\mathbf{E}_1|^2$ and $I_2 = |\mathbf{E}_2|^2$ denote the intensities of the initial waves. Assuming both waves propagate collinearly along the z-axis and both initial waves have the same oscillation frequency Eq. 2.2 can be simplified to

$$I = I_1 + I_2 + 2\sqrt{I_1 I_2}\cos\left(\Phi_1 - \Phi_2 - \omega\tau_\mathrm{d}\right) = I_1 + I_2 + 2\sqrt{I_1 I_2}\cos\left(\Phi_1 - \Phi_2^*\right) . \quad (2.3)$$

The term $\omega\tau_\mathrm{d}$ describes a phase difference due to a temporal delay τ_d between the two waves. In case of plane waves which extend infinitely in time, this term is equivalent to a phase shift and has been included into ϕ_2^*. This term, however, will be relevant when looking at the interference of pulses in Sec. 2.7.2. It is evident from Eq. 2.3 that the intensity I of the superposition can take any value between $I_1+I_2-2\sqrt{I_1 I_2}$ (destructive interference) and $I_1 + I_2 + 2\sqrt{I_1 I_2}$ (constructive interference). The intensity of the superposition is determined by the phase difference between the two pulses. The interference between real laser beams is often shaped by a phase which depends on the frequency (spectral phase), temporal delay or a spatial dimension. Therefore, two interfering laser beams often show a fringe pattern in space or frequency domain.

If a light wave is traveling in a medium other than vacuum it induces a response in the material. This material response can be expressed in terms of the polarization $P(t)$. The modified wave-equation in the presence of such an induced polarization is given by

$$\nabla\mathbf{E} - \frac{1}{c^2}\frac{\partial^2\mathbf{E}}{\partial t^2} = \frac{1}{\epsilon_0 c^2}\frac{\partial^2}{\partial t^2}P(t) . \quad (2.4)$$

Under the assumption of a low intensity and an instantaneous material response, the induced polarization is a linear function of the electric field given by

$$P(t) = \epsilon_0\chi^{(1)}\mathbf{E}(t) . \quad (2.5)$$

Here, ϵ_0 denotes the free space permittivity and $\chi^{(1)}$ is a material property called the linear susceptibility [41, p.2].

By inserting Eq. 2.5 into Eq.2.4 and using the definition $n = \sqrt{1+\chi^{(1)}}$, it can be shown that the velocity v_ph of the light waves is modified by the material response and given by

$$v_\mathrm{ph} = \left|\frac{dx}{dt}\right| = \frac{\omega}{k} = \frac{c}{n} . \quad (2.6)$$

If light waves travel in a transparent medium, the speed of light is augmented by the material reducing the velocity of the light waves. This effect is expressed by the materials refractive index which then assumes values of $n > 1$. Typically the refractive index of a material depends on the wavelength and intensity of the wave. The effects of these dependencies are discussed in Sec. 2.3.1 and Sec. 2.5, respectively.

2.2 Gaussian Laser Beams

In the previous chapter, plane waves have been discussed as a solution to the wave equation determining the propagation behaviour of light (Eq. 2.1). However, these plane waves are characterized by a singular oscillation frequency ω and expand infinitely in space, both of these properties are not achievable in real world light fields.

Therefore, a different set of solutions to Eq. 2.1 with finite spatial dimensions is required to describe laser beams.

As this Section is concerned with the spatial properties of laser beams, it is convenient to separate the temporal and spatial dependencies in the wave-equation 2.1. Additionally, we will consider monochromatic beams at a distinct frequency ω and an electric field given by $E(\mathbf{r},t) = Re\,[A_0(\mathbf{r},\omega)e^{i\omega t}]$. A field of this form can only be a solution to the wave equation if the term depending on $\mathbf{r}$ satisfies the paraxial Helmholtz-equation. Assuming again that the field is propagating in z-direction and making *slowly varying envelope approximation* defined by

$$\lambda \left| \frac{\partial \left(\frac{\partial A}{\partial z}\right)}{\partial z} \right| \ll 2\pi \left| \frac{\partial A}{\partial z} \right| \tag{2.7}$$

,the Helmholtz equation takes the form given in Eq. 2.8 [42, p.94]

$$\nabla_\perp^2 A_0 - 2i\frac{\partial A_0}{\partial z} = 0\ . \tag{2.8}$$

A complete set of orthogonal solutions to Eq. 2.8 is given by the Gauss-Hermitian beams. With $\tilde{A_0} = A_0/(jz_0)$, this set of solutions is given by

$$\begin{aligned} E(\mathbf{r}) = \tilde{A_0} H_n\left(\frac{\sqrt{2}x}{w(z)}\right) H_m\left(\frac{\sqrt{2}y}{w(z)}\right) e^{i(n+m)\zeta(z)} \\ \cdot \quad \frac{w_0}{w(z)} e^{-\frac{r^2}{w^2(z)}} e^{-ik\frac{r^2}{2R(z)}} e^{-ikz+i\zeta(z)}\ . \end{aligned} \tag{2.9}$$

In this equation, $w(z)$ and $R(z)$ describe the spot size parameter of the beam and the curvature of the wave fronts, respectively. I note here, that the spot size in this context is defined as the radial position at which the intensity of the light field has a value of $1/e^2 \cdot I_0$. It is thus often called the $1/e^2$-waist size. $\zeta(z) = arctan(z/z_0)$ is called the *Gouy phase*. $r = \sqrt{x^2+y^2}$ is the radial coordinate. The functions H_n and H_m are the Hermitian polynomials of order $n \in \mathbb{N}$ and $m \in \mathbb{N}$, respectively. These polynomial functions are given by the recursive series [42, p.114] in Eq. 2.10

$$\begin{aligned} H_0(x) &= 1 \\ H_1(x) &= 2x \\ H_{l+1} &= 2xH_l(x) - 2lH_{l-1}(x)\ . \end{aligned} \tag{2.10}$$

In isotropic media, where the electric field components in propagation direction vanish, the set of eigenfunctions given by Eq. 2.9 are called transversal electromagnetic modes (TEM). An especially important solution is the case of $n = m = 0$, a case called the TEM_{00} mode. Due to its relevance in laser amplifiers and beam propagation, the most important properties of such TEM_{00} modes are discussed below.

The spatial field distribution for this case can be deduced by inserting the appropriate Hermite polynomials and values for n and m in Eq. 2.9

$$E(\mathbf{r}) = \tilde{A_0}\left(\frac{\sqrt{2}x}{w(z)}\right)\left(\frac{\sqrt{2}y}{w(z)}\right)\frac{w_0}{w(z)} e^{-\frac{r^2}{w^2(z)}} e^{-ik\frac{r^2}{2R(z)}} e^{-ikz+i\zeta(z)}\ . \tag{2.11}$$

The associated intensity profile is given by

$$I(\mathbf{r}) = \tilde{I}_0 \left(\frac{\sqrt{2}x}{w(z)}\right)\left(\frac{\sqrt{2}y}{w(z)}\right)\left(\frac{w_0}{w(z)}\right)^2 e^{-2\frac{r^2}{w^2(z)}} . \tag{2.12}$$

It is apparent from the equation, that the TEM_{00} mode has a Gaussian transversal intensity distribution radially symmetric around the axis of propagation. A beam with a TEM_{00} mode is thus often called a Gaussian beam (see [42, Sec. 3.1.2-3.1.5]). Note that this is a purely spatial description and should not be confused with a temporal Gaussian profile.

The laser amplifiers built as part of this thesis are designed to deliver laser beams with near Gaussian profiles. Therefore, the propagation behaviour of Gaussian beams is highly relevant for the design of the amplifier resonators. The evolution of the spatial intensity profile of a propagating Gaussian beam along the z-direction can be described in terms of the wavelength of the laser beam λ and the size w_0 and position z_f of its minimum waist [42]

$$w^2(z) = w_0^2 + \left(\frac{\lambda}{\pi\omega_0}\right)^2 \cdot (z - z_\mathrm{f}) . \tag{2.13}$$

An alternative description of the waist size $w(z)$ is given by

$$w(z) = w_0\sqrt{1 + \left(\frac{z}{z_\mathrm{R}}\right)^2} . \tag{2.14}$$

where $z_\mathrm{R} = \frac{\pi w_0^2}{\lambda}$ denotes the Rayleigh length. z_R is the distance from the minimum waist position at which the beam waist increased to $\sqrt{2}w_0$. It is apparent from Eq. 2.14, that $w(z)$ approaches a linear increase for $z >> z_\mathrm{R}$ which has a finite divergence angle $\Theta_0 = \frac{\lambda}{\pi w_0}$. With the Rayleigh length z_R, the radius of curvature of the Gaussian beam wavefront can be described as

$$R(z) = z_0\left[\frac{z}{z_\mathrm{r}} + \frac{z_\mathrm{r}}{z}\right] . \tag{2.15}$$

It is useful to define a complex beam parameter $q(z)$, which describes the propagation behaviour of the Gaussian modes [43, p.80 ff.]

$$\frac{1}{q(z)} = \frac{1}{R(z)} - \frac{i\lambda}{\pi w(z)} . \tag{2.16}$$

This parameter allows for a straightforward description of beam propagation in arbitrary optical systems via the ray transfer matrix formalism. In this formalism, the interaction of the beam with an optical element such as a lens or a free-space propagation of length L is described by a 2x2 transfer matrix M where

$$M = \begin{pmatrix} A & B \\ C & D \end{pmatrix} . \tag{2.17}$$

The properties of the Gaussian beam after interaction with the optical system described by M is given by q_2 with

$$q_2 = \frac{Aq + B}{Cq + D} . \tag{2.18}$$

The values of the parameters A, B, C and D are determined by the nature of the optical system. A ray transfer matrix for arbitrary systems can be generated by matrix multiplication of the individual elements it contains. As part of this work, the ray transfer matrix formalism was used to calculate the beam parameter inside the Yb:YAG-amplifiers resonator and to judge its stability behaviour. A more thorough description of the matrix formalism with examples for the transfer matrices for specific optical elements can be found in [43, Sec. 1.2].

2.2.1 The Beam Quality Parameter

An important parameter for characterizing the focusability of a laser beam is the *M^2-parameter* often called the beam quality factor. The M^2-parameter offers a measure for how close a laser beam is to a TEM_{00} mode. This is a relevant in laser development, since the observation of a Gaussian intensity profile at one point in space does not suffice to identify a TEM_{00} mode. There are superpositions of higher order modes which also exhibit a Gaussian intensity profile but have different beam divergence. The M^2 parameter is defined by the product of the beam divergence θ and beam width w_0 as [44, p.482]

$$M^2_{x/y} = \frac{\pi}{\lambda}\theta_{x/y} \cdot w_{0,x/y} \; . \tag{2.19}$$

For a TEM_{00} mode the M^2 parameter is equal to one in both the x and y direction. Higher order modes, however, have M^2 values > 1. It can be shown that for a Gauss-Hermitian TEM_{nm} mode described by Eq. 2.9 the modified beam waists and divergences are given by [43, p. 100]

$$\begin{aligned} w_\mathrm{x} &= w_{0,\mathrm{x}}\sqrt{2n+1} & \qquad \theta_\mathrm{x} &= \theta_{0\mathrm{x}}\sqrt{2n+1} \\ w_\mathrm{y} &= w_{0,\mathrm{y}}\sqrt{2m+1} & \qquad \theta_\mathrm{y} &= \theta_{0\mathrm{y}}\sqrt{2m+1} \end{aligned} \; . \tag{2.20}$$

Therefore, the beam quality parameter in x and y direction is given by $M^2_\mathrm{x} = (2n+1)$ and $M^2_\mathrm{y} = (2n+1)$. Considering the M^2 value for a real laser beam, the evolution of the laser beam size along the propagation axis z is determined by [45]

$$W^2(z) = W_0^2 + \left(M^2 \frac{\lambda}{\pi W_0}\right)^2 \cdot (t - z_\mathrm{f}) \; . \tag{2.21}$$

If superpositions of Gauss-Hermitian modes are considered, the M^2 value can be calculated by the following equations [45]

$$M^2_\mathrm{x} = \sum_{n=0}^{\mathrm{inf}} \sum_{m=0}^{\mathrm{inf}} (2n+1)|\tilde{C}_\mathrm{nm}|^2 \tag{2.22}$$

and

$$M^2_\mathrm{y} = \sum_{n=0}^{\mathrm{inf}} \sum_{m=0}^{\mathrm{inf}} (2m+1)|\tilde{C}_\mathrm{nm}|^2 \; . \tag{2.23}$$

The coefficients $\tilde{C}_\mathrm{nm}$ are the relative amplitudes of the respective TEM_{nm} modes. For experiments it is often crucial to achieve focusability of the involved laser beams close to the diffraction limit. Therefore, amplifying beams with close to TEM_{00} modes is

required. These modes can be identified by measuring the M^2 parameter. As arbitrary superpositions of higher order modes do not necessarily have a (radially) symmetric spatial profile, a $1/e^2$ definition of the beam size is no longer viable. Thus, for a meaningful measurement of the M^2 parameter, the so-called *D4σ beam diameters* have to be measured. This diameter can be obtained from a camera image of the beams intensity $I(x, y)$ according to Eq.2.24

$$D4\sigma = 4\sqrt{\frac{\int_{-\infty}^{\infty}\int_{-\infty}^{\infty} I(x,y)(x-\bar{x})^2 dxdy}{\int_{-\infty}^{\infty}\int_{-\infty}^{\infty} I(x,y)dxdy}} \tag{2.24}$$

where $\bar{x}$ is the centroid of the intensity profile.

2.3 Properties of Ultrashort Pulses

The properties discussed in the previous sections have treated the laser beams as monochromatic waves and neglected the temporal dimensions. Modern optics, however, relies on the creation and application of trains of ultrashort pulses of light. The confinement of the laser beam's energy to ultrashort wave packets enables experiments with time-resolution down to the attosecond level. Furthermore, high intensities can be reached within the duration of short pulses of light. This gives rise to nonlinear effects and light-matter interactions not achievable with monochromatic beams. These trains of light pulses are typically characterized by the electric field envelope $A(t)$, a carrier frequency ω_0 and the repetition rate f_{rep}. Each pulse in a beam with average power P_{avg} carries a pulse energy of $E_{\mathrm{p}} = P_{\mathrm{avg}}/f_{\mathrm{rep}}$. Such light pulses can be created by a superposition of monochromatic waves

$$E(t) = \frac{1}{2\pi}\int_{-\infty}^{\infty} A(\omega) * e^{i(\mathbf{kr}-\omega t)+\phi(\omega)} d\omega \ . \tag{2.25}$$

The repetition rate $f_{\mathrm{rep}} = 1/T$ describes how many pulses the pulse train contains per unit time and is defined as the inverse of the time T between the pulses. The repetition rate is an important property in laser development as it determines the average power of a beam of pulses with a given energy E_{p}. It also determines the maximum data acquisition rate in experiments. However, it is not relevant for the light-matter interactions and pulse properties discussed below. Therefore, the repetitive nature of the pulse train will be neglected and the pulses will be regarded as singular events in the further discussion.

The electric field of the light pulse in the time domain resulting from Eq.2.25 is given by

$$E(t) = A(t) \cdot e^{i(kz-\omega_0 t+\phi(t))} \ . \tag{2.26}$$

Here, the electric field envelope is a Gaussian function $A(t) = A_0 \exp\left(-4\ln(2)\cdot t^2/\tau^2\right)$ with full-width-half-maximum (FWHM) pulse duration of τ and amplitude A_0. The pulse duration in this description is directly related to the spectral bandwidth $\Delta\nu$ of the pulses as the frequency- and time domain representation of the light field are connected by the Fourier-transformation. This relation can be expressed in terms of

the time-bandwidth product p_{tb}

$$\tau\Delta\nu = \tau\frac{c\Delta\lambda}{\lambda_{\mathrm{min}}\lambda_{\mathrm{max}}} = p_{\mathrm{tb}} = \text{const.}\,. \tag{2.27}$$

Here, $\Delta\lambda = \lambda_{\mathrm{max}} - \lambda_{\mathrm{min}}$ denotes the spectral bandwidth in terms of wavelengths. From Equation 2.27 it is apparent that a short pulse duration requires a large spectral bandwidth. The constant to the right side of the equation is a scalar parameter depending on the shape of the light pulse. For a pulse with a Gaussian temporal profile the time-bandwidth product satisfies $p_{\mathrm{tb}} \approx 0.44$.

The minimum pulse duration τ_0 a light pulse can have is thus determined by its spectral bandwidth $\Delta\nu$ via the time-bandwidth product. If a pulse exhibits this minimum duration it is referred to as bandwidth limited or Fourier-transform-limited pulse. Typically, the duration of laser pulses is larger than τ_0 due to material dispersion or other effects influencing the spectral phase of the pulses.

The propagation speed of light pulses in a transparent medium is no longer adequately described by the phase velocity. Due to the spectral bandwidth of the pulse and the frequency dependence of the refractive index, the light pulse travels at a speed called the group velocity v_{g} with

$$v_{\mathrm{g}} = \left(\frac{\mathrm{d}k}{\mathrm{d}\omega}\right)^{-1}_{\omega_0} = \frac{c}{n} - \frac{k\cdot c}{n^2}\frac{\mathrm{d}n}{\mathrm{d}k}\,. \tag{2.28}$$

Therefore, the group velocity describes the propagation speed of the energy contained in the light pulse. It is also the relevant velocity in regard to information transfer e.g. in fiber-based communication. The influence of the frequency dependent linear refractive index will be discussed in more detail in Sec. 2.3.1.

In contrast to plane waves, the average power is not a sufficient description of a train of short light pulses. In a beam oformed by a number of wave-packets, all the energy in the beam is confined into the light pulses. Therefore, the power inside the pulse intensity envelope can exceed that of a plane wave of identical average power by many orders of magnitude. To account for this effect, the peak power P_{peak} and peak intensity I_{peak} are introduced. These parameters can be calculated from the pulse energy E_{p} and the pulse duration τ_{p} by

$$P_{\mathrm{peak}} = f_{\mathrm{s}}\frac{E_{\mathrm{p}}}{\tau_{\mathrm{p}}} \qquad \text{and} \qquad I_{\mathrm{peak}} = 2\frac{P_{\mathrm{peak}}}{A} \tag{2.29}$$

where f_{s} is a numerical factor which depends on the temporal shape of the pulse. The parameter in case of a Gaussian temporal shape, takes the value $f_{\mathrm{s}} = 2\sqrt{\ln 2/2} \approx 0.94$. A denotes the effective area size of the beam.

2.3.1 Dispersion

A train of laser pulses can be described by a superposition of continuous waves each having a different oscillation frequency. This has been shown in Eq. 2.25 of the previous section. If such a light pulse is traveling through a transparent medium the light waves induce a material response resulting in a refractive index n. This refractive index, however, generally depends on the frequency $\omega = 2\pi c/\lambda$ of the light

wave. From Eq. 2.6 it can be shown, that the absolute value of the wave-vector satisfies $k = \frac{\omega n}{c}$ when the wave is traveling throu a medium with refractive index n. The most common quantitative expression for the refractive index depending on the oscillation parameters of the electro-magnetic wave is the Sellmeier equation [40, p.181]

$$n^2(\lambda) = 1 + \sum_{\mathrm{j}=1}^{N} \frac{A_\mathrm{j}\lambda^2}{\lambda^2 - B_\mathrm{j}^2} \,. \tag{2.30}$$

Here, the material response is expressed in terms of the wavelength λ of the electromagnetic waves. The Sellmeier coefficients A_j and B_j are empirically determined parameters.

For a pulse covering the wavelength range $\Delta\omega_\mathrm{p} = [\omega_\mathrm{min}, \omega_\mathrm{max}]$, $n(\omega)$ is typically not equal for all frequencies forming the pulse. Hence different frequencies in the pulse travel at different speeds and a pulse with an initially bandwidth-limited duration will spread out in time. To illustrate the effect of the frequency dependent refractive index, it is convenient to expand the wavevector k in a Tailor-series around the carrier frequency of the pulse ω_0. With $\Omega = (\omega - \omega_0)$, $k(\omega)$ is given by

$$k(\omega) = k(\omega_0) + \Omega \left(\frac{\partial k}{\partial \omega}\right)_{\omega_0} + \frac{1}{2}\Omega^2 \left(\frac{\partial^2 k}{\partial \omega^2}\right)_{\omega_0} + \frac{1}{6}\Omega^3 \left(\frac{\partial^3 k}{\partial \omega^3}\right)_{\omega_0} + \cdots \,. \tag{2.31}$$

The first term in the series determines the phase velocity at the carrier frequency $v_\mathrm{ph} = \frac{k(\omega_0)}{\omega_0}$ and is independent of frequency. Thus it leads to a phase shift of the whole frequency spectrum of the pulse. This results in a shift of the carrier-envelope phase which is discussed in Sec. 2.3.2. The remaining terms all depend on the frequency Ω and each describe different orders of dispersion.

The term linear in Ω describes an overall displacement in time and is connected to the group velocity $v_\mathrm{g}(\omega_0) = \left(\frac{\partial k}{\partial \omega}\right)^{-1}_{\omega_0}$ of the pulse. In contrast to the phase velocity, the group velocity is the propagation speed of the whole wave packet. Therefore, it describes the speed at which the energy contained in the light field travels through the medium.

The higher order terms describe dispersion effects which reshape the temporal pulse and result in a redistribution of instantaneous frequencies inside the wave packet. For this work only the first two of these higher dispersion terms are relevant and will be discussed in detail.

The quadratic term $\left(\frac{\partial^2 k}{\partial \omega^2}\right)_{\omega_0}$ describes the second order dispersion often referred to as group velocity dispersion (GVD). This term leads to a separation of the frequency components called frequency chirp and to an increasing temporal width of the light pulse. A closely related quantity is the group delay dispersion (GDD) which is often used to describe the dispersion introduced by an optical element. The GVD corresponds to the GDD per unit length. For GVD > 0, higher frequency components travel slower than low frequency components. This situation is referred to as normal dispersion. Accordingly, anomalous dispersion describes the case when GVD < 0 and the low frequency components have a higher propagation speed. The effects of the second order dispersion are illustrated in Fig. 2.1

In both normal and anomalous dispersion, the propagation inside the material leads to an increase in pulse duration and a linear shift in the instantaneous fre-

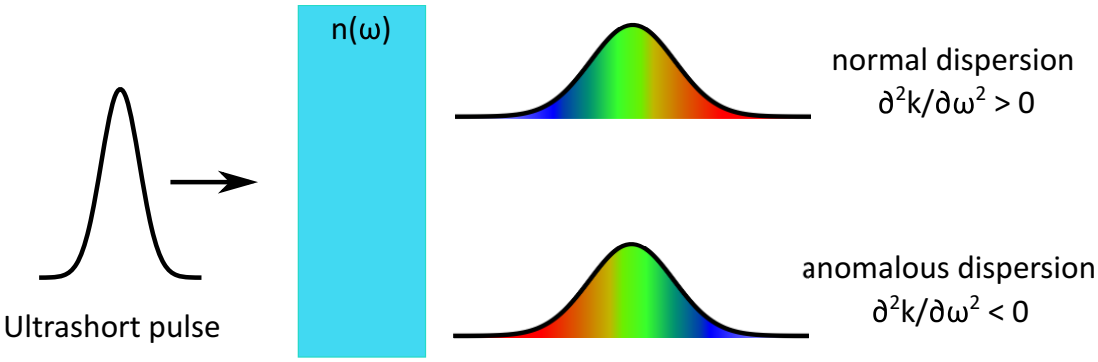

Figure 2.1: The effect of normal and anomalous dispersion on short light pulses.

quency $\omega(\tilde{t})$ throughout the pulse. In ultrafast science, this effect often leads to an unwanted increase of the pulse duration which needs to be compensated to achieve pulse durations close to the Fourier-transform limit. However, many applications also utilize the pulse stretching or chirp induced by second order dispersion. Therefore, only the ability for a precise control of the second order dispersion makes applications such as CPA viable.

The term which is cubic in Ω contains the third order dispersion (TOD) determined by $\left(\frac{\partial^3 k}{\partial \omega^3}\right)_{\omega_0}$. This term becomes relevant for pulses with a large bandwidth $\Delta\omega$ and needs to be taken into account in the compression of broadband pulses. The effects of TOD on the light pulse are the formation of pre- or post pulses.

2.3.2 The Carrier-Envelope-Phase

The CEP of a light pulse is defined as the phase difference between the envelope and the carrier wave of the pulse. It is closely related to the carrier-envelope-offset-frequency (CEO) defined by $f_{\mathrm{ceo}} = \frac{d}{dt}\varphi_{\mathrm{ce}}$. The stabilization of the CEO led to a revolution in frequency metrology [46, 47] and allowed for the generation of CEP-stable pulses. This section, however, will be limited to the description of the CEP.

The CEP of a laser pulse plays an important role in many interactions of few-cycle laser pulses with matter especially as pulse durations approach the single-cycle regime. For a pulse as described by Eq. 2.26 it is defined by the delay Δt between the maximum of the field envelope and the nearest maximum of the carrier oscillation. The structure of the electric field under the pulse envelope is repetitive after a full 2π phase shift. Therefore, the CEP is typically defined on interval of $[0, 2\pi]$. Fig. 2.2 illustrates the electric field oscillations for pulses with different CEP-values φ_{ce}.

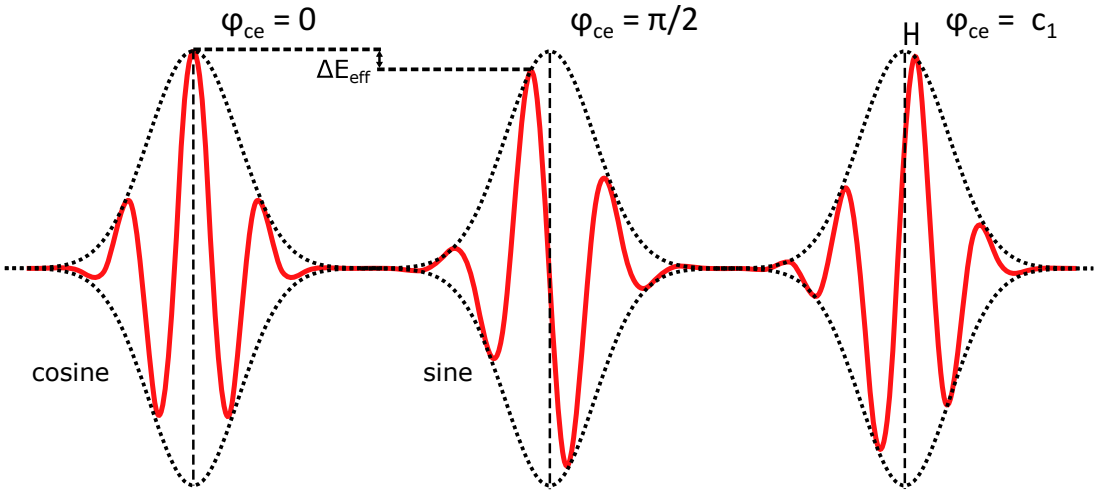

Figure 2.2: Schematic drawing of few-cycle-pulses illustrating the electric field evolution in time for a pulse with a CEP of $\varphi_{ce} = 0$ (left), $\varphi_{ce} = \pi/2$ (center) and $\varphi_{ce} = c_1$ with an arbitrary constant c_1 (right). A clear difference in the maximum electric field strength can be observed between the $\varphi_{ce} = 0$ and $\varphi_{ce} = \pi/2$ case.

Two distinct features can be identified in the electric field oscillation of a few-cycle laser pulse. Especially interesting for experiments studying field sensitive effects is the fact that the effective field strength E_{eff} of a few-cycle laser pulse depends on the CEP. From Fig. 2.2 it is evident, that the electric field strength is assuming a higher value for a cosine-like ($\varphi_{ce} = 0$) field oscillation than for a sine-like oscillation ($\varphi_{ce} = \pi/2$). Furthermore, there is an asymmetry in the field strength between the oscillation cycles pointing in x-direction (upwards in Fig. 2.2) and in -x-direction (downwards) if $\varphi_{ce} = 0$. This property is utilized to generate isolated attosecond pulses via amplitude gating in HHG-setups [48].

If a pulse is propagating in vacuum, its CEP is static. However, if the pulse is travelling through a dispersive medium, its CEP is affected by the material dispersion. From Eq.2.31, the phase velocity of the carrier wave and the group velocity of the pulse envelope can be deduced. These two velocities are not generally equal. The difference between phase and group velocity directly implies a change in CEP of $\Delta\varphi_{ce} = (1/v_g - 1/v_p) \cdot \omega_0 L$ [49]. If the peak intensity of the pulses is high enough, the CEP is also subject to changes due to the nonlinear propagation in the medium. This leads to a nonlinear phase change of ω_0 $\Delta\varphi_{NL} = -B\omega_0(dn/d\omega)/n_2$ for a pulse with carrier frequency ω_0 propagating in a medium with a nonlinear refractive index n_2 [50]. The shift in CEP thus depends on the nonlinear phase shift B, also called the B-integral (see. Eq. 2.44).

An important attribute when a whole train of pulses is concerned, is CEP stability which means that all pulses share a common CEP-value. A train of laser pulses is not inherently CEP-stable. Often, the CEP takes a random value for each pulse. Consecutive pulses have a well-defined phase relation only if the source of the laser pulses is actively or passively CEP-stabilized. Many experiments involve techniques such as electro-optic-sampling (EOS) or strong field ionization, which rely on field sensitive effects and require stable field transients. CEP-stable pulse trains are essential for such experiments and thus highly desirable for modern optics.

2.4 Amplification of Ultrashort pulses

Amplification of ultrashort pulses is one of the key elements of modern optics. Without means to generate energetic pulses with picosecond or even femtosecond pulse durations, whole fields of science like optical material processing, strong field or attosecond physics would be unimaginable. In this section, I will discuss the fundamentals of light amplification by stimulated emission from an active laser material, such as Ti:sapphire or Yb:YAG. Pulse amplification based on nonlinear parametric processes is discussed in Sec. 2.6. Amplifiers based on stimulated emission come in various geometries such as bulk crystals [51, 52], fibers [53, 52], slabs [54, 52] or disks [55, 52] which all offer distinct advantages and disadvantages. The fundamental principles behind the amplification process, however, is common among all of them. In these types of amplifiers, an active laser material is illuminated by a powerful pump light beam, which is absorbed by the material. The pump beam excites electrons creating a population inversion between an upper and a lower energy level. Population inversion is reached, when the higher energy level has a larger electron population than the lower energy level. The two levels are referred to as the upper and lower laser level. I note here, that population inversion cannot be achieved in a simple two level system. At least three energy levels have to be involved to achieve population inversion. In real laser materials, often 4 or more levels contribute. Because of its relevance for this thesis, Fig. 2.3 shows the energy level configuration for Yb:YAG.

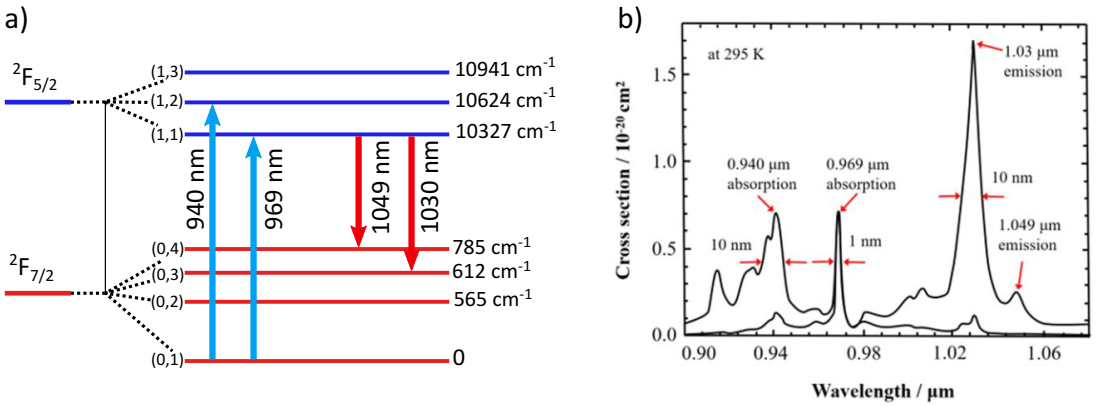

Figure 2.3: a) Energy level structure of the Yb^{3+} ion in yttrium-aluminum-garnet (YAG). The most important pump and emission transitions are marked. b) Absorption and emission cross section of Yb:YAG at 295 K. The graph was taken from [56].

In multi-level amplification materials, there are typically multiple sets of energy levels which can be involved in the amplification process. Yb:YAG for example can be pumped by light with a wavelength of 941 nm or 969 nm. In both cases, electrons are excited from the lowest energy $^2F_{7/2}$ sub-level, however, the final energy levels of the excitation process are different. At a pump wavelength of 969 nm, the electrons are pumped directly into the upper laser level. This pump schemes is therefore called the *phonon free*, as no non-radiative transfer between upper energy levels is involved in the process. This is especially beneficial for high power amplifiers as the thermal load on the active medium is significantly lower in this case.

If a beam of photons with energy of $\hbar\omega$ equal to the energy difference between

the upper and lower laser level propagates through the active medium, it stimulates transitions between the two energy levels. In a thermal equilibrium, this will lead to an absorption of the beam, exciting electrons from the lower to the upper laser level. In the presence of population inversion, however, the photons will stimulate a deexcitation of the electrons in the upper laser level. This deexcitation process results in the coherent emission of an additional photon with an energy of $\hbar\omega$ [1]. The incoming light beam is therefore amplified by the stimulated emission from the upper laser level. The gain G a laser beam experiences while traveling through an active medium is determined by the absorption and emission cross sections σ_{abs} and σ_{em} and the difference in the population of the upper and lower laser level $\Delta N = N_{\text{upper}} - N_{\text{lower}}$. Thus, the amplification gain assuming quasi-plane waves propagating along th z-axis through an active medium of length L is given by Eq. 2.32[57, p.280].

$$G = \frac{I(L))}{I(0))} = e^{(2\alpha_{\text{m}} L)} \ . \tag{2.32}$$

Here $I(L)$ and $I(0)$ denote the final and initial intensity of the amplified beam and $2\alpha = N_2\sigma_{\text{em}}(\lambda) - N_1\sigma_{\text{abs}}(\lambda)$ denotes the small signal amplification gain coefficient. The formula also assumes a lossless propagation through the medium. In the case of low gain, the intensity increases exponentially inside the material. However, in high power amplifiers, one typically has to take the high energy extraction into account. The pumped active medium contains a finit energy given by

$$E_{\text{am}} = (N_2 - N_1))AL\hbar\omega \ . \tag{2.33}$$

Here, AL describes the effective volume of the active medium. Srong energy extraction leads to a time dependent level of population inversion $\Delta N(t)$ Therefore, gain saturation is an important effect for high power amplifiers and is typically described by the saturation intensity I_{sat} and saturation fluence F_{sat}. Notably, with the emission cross section σ_{em} and transition energy $\hbar\omega$ these saturation parameters depend only on material properties [57, p.293, p.367] and are given by

$$I_{\text{sat}} = \frac{\hbar\omega}{\sigma_{\text{em}}\tau_{\text{eff}}} \qquad \text{and} \qquad F_{\text{sat}} = \frac{\hbar\omega}{2\sigma_{\text{em}}} \ . \tag{2.34}$$

In this context, I_{sat} describes the intensity at which the amplification gain coefficient is reduced to half of the small signal value and τ_{eff} is the effective life time. The saturation fluence F_{sat} determines the pulse energy per unit area that leads to an analogous reduction in amplification gain and is relevant when the amplification of laser pulses is considered. For high power amplifiers, these saturation parameters have to be considered in the design of the setup.

As part of this thesis, multiple laser amplifiers based on Yb:YAG thin disks have been built. The thin disk geometry for the active laser medium offers two major advantages relevant for amplifying pulses with high pulse energy. Both of these advantages are connected to the low thickness of the active medium. The Yb:YAG disks used to built the amplifiers relevant for this thesis have a thickness of only 100 μm to 200 μm with diameters of 9 mm to 13 mm. The disks are bonded to a diamond/copper heat sink which is backside cooled by a water. The low aspect ratio of the disk allows for an efficient heat removal and a quasi-one-dimensional heat flow from the active medium. Therefore, thermal stress to the medium and thermally induced distortions

to the amplified beam are mitigated [58]. This makes thin disk amplifiers especially suitable for the amplification to high average powers. The second advantage of the thin gain medium is the low nonlinear interaction length. The B-integral accumulated by propagating through a disk of a thickness below 500 μm can be kept small even when large pulse energies are involved. Thus, thin disks are most suitable amplification of pulses to energies beyond the mJ level. In accordance with Eq. 2.32, the low thickness of the active medium in thin disk amplifiers, however, results in limited single pass gain. Therefore, thin disk active media have to be inserted into resonators or multi-pass setups, to allow for high amplification gain.

2.4.1 Chirped Pulse Amplification

The development of the CPA was one of the most impactful technological advancements in optics since the development of the laser itself [14]. Together with the development of broadband solid-state lasers based on Ti:sapphire, CPA paved the way for strong field and attosecond science. But also biomedical and material processing applications benefit from pulsed laser sources with high pulse energy enabled by the CPA concept. Due to the wide range of applications and its high relevance for many fields of science the inventors of this technique were awarded the Nobel prize in physics in the year 2018. The concept behind CPA is surprisingly simple and is shown schematically in Fig. 2.4 b). To avoid optical damage and nonlinear beam distortions in laser amplifiers due to high peak intensities, the pulses are stretched in time prior to amplification.

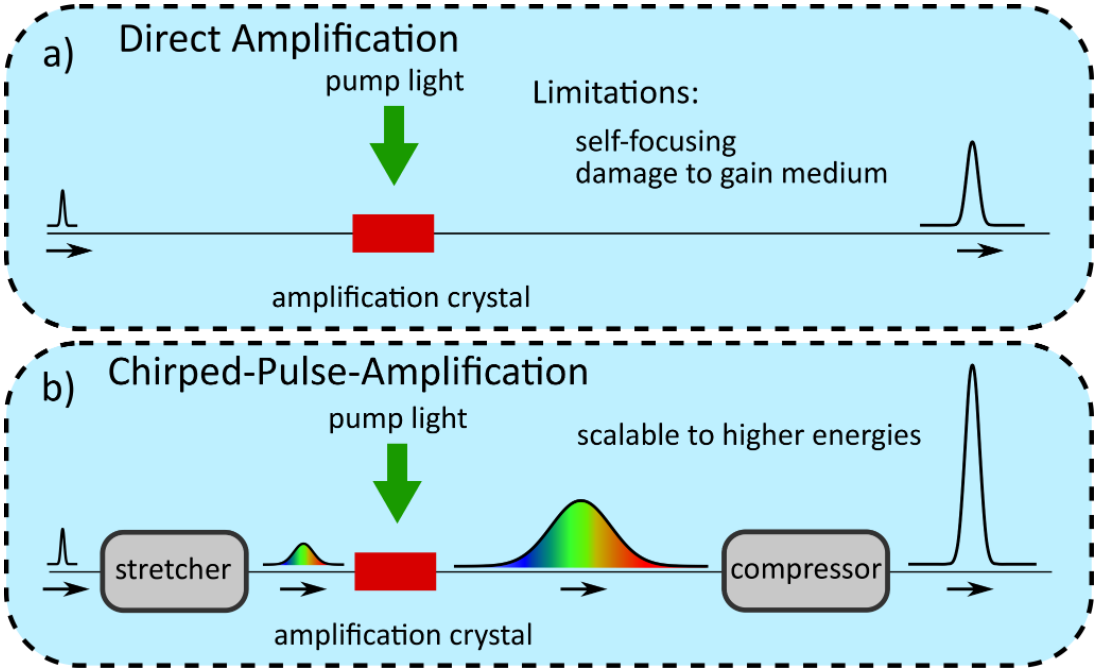

Figure 2.4: Schematic illustration of the amplification process in direct pulse amplifiers (a) and chirped pulse amplification (b).

The peak power scales proportional to E_p/τ with pulse energy E_p and pulse duration τ. Therefore, the pulse energy of the amplified pulses can be scaled up by the

stretching ratio τ^{s}/τ, where τ^{s} is the duration of the stretched pulse. Typically, the pulses are stretched and compressed with stretcher- and compressor units based on reflection gratings, which have to apply matched amounts of GDD to the pulse. Due to the large pulse energies achievable in CPA-setups, the gratings in the compressor need to be very large to accommodate for the beam sizes necessary to avoid laser induced damage once the beam is compressed. Therefore, these compressor units are expensive and require large amounts of space to set up.

2.4.2 Gain Bandwidth and Gain Narrowing

From Eq. 2.32 we can see that the single pass amplification gain depends on the population N_2 and N_1 of the upper and lower laser level as well as the emission cross section σ_{em} and absorption cross section σ_{abs}. In real materials, energy levels are not infinitely sharp but have a certain width in energy. Therefore, any kind of laser transposition is associated with a certain linewidth $\Delta\omega_{\mathrm{a}}$ around a *midband* frequency ω_{a}. The transition cross section is typically depending on the frequency and takes the largest value for $\omega = \omega_{\mathrm{a}}$

Due to the frequency dependency of the transition cross section, the amplification gain is likewise frequency dependent. Assuming a Lorentzian line shape which is common for radiative transitions in real materials and a FWHM linewidth $\Delta\omega_{\mathrm{a}}$, the amplification bandwidth of a laser amplifier is given by [57, p.282]

$$\Delta\omega = \Delta\omega_{\mathrm{a}}\sqrt{\frac{3}{10\log_{10}\left(G(\omega_{\mathrm{a}})\right) - 3}}\,. \tag{2.35}$$

Notably, the amplification bandwidth decreases with the total gain at the midband frequency $G(\omega_{\mathrm{a}})$. This effect of bandwidth reduction is called *gain narrowing* and often limits the achievable output bandwidth and compressed pulse duration in high gain amplifiers [53].

2.5 Nonlinear Light-Matter Interactions

If matter interacts with an intense light field, the properties of the material are augmented by its presence. This augmentation of material properties gives rise to a vast amount of interesting effects, which depend nonlinearly on the involved field strengths. Therefore, the study of these effects is called nonlinear optics. Due to the nonlinear dependence on field strength, nonlinear optical effects are especially relevant for ultrashort pulses with high pulse energy. In this section, I will introduce the effects most relevant for this thesis.

In analogy to the linear case discussed previously, the nonlinear material response to the presence of a strong electro-magnetic field is generally described by the induced polarization $P(t)$. When intense fields are involved, the linear polarization term in Eq. 2.5 has to be extended by a power series of the electric field. Assuming an isotropic medium, the polarization can then be described by Eq. 2.36 [41, p.2]

$$P(t) = \epsilon_0\left[\chi^{(1)}\vec{E}(t) + \chi^{(2)}\vec{E}^2(t) + \chi^{(3)}\vec{E}^3(t) + \cdots = P^{(1)}(t) + P^{(2)}(t) + P^{(3)}(t)\right]\,. \tag{2.36}$$

For $n = 2, 3, 4, ..$, the quantities $\chi^{(n)}$ are known as the n-th order nonlinear susceptibility and ϵ_0 denotes the permittivity of free space. I note here that the susceptibilities $\chi^{(n)}$ are not scalars but tensors of rank $n + 1$. Therefore, the strength of the nonlinear susceptibilities in unisotropic media depends on the polarization direction of the involved light fields with respect to the relevant optical axis of the medium. If the material response is separated into its linear and nonlinear contributions, the polarization can be written as $P(t) = P^{(1)}(t) + P^{\mathrm{NL}(t)}$. By inserting this definition into Eq. 2.1 wave-equation describing the propagation of light waves in the material is now given by

$$\nabla^2 E(t) - \frac{n^2}{c^2}\frac{\partial^2 E(t)}{\partial t^2} = \frac{4\pi}{c^2}\frac{\partial^2 P^{\mathrm{NL}}(t)}{\partial t^2} \,. \tag{2.37}$$

Here, we made use of the results from Sec. 2.3.1 and expressed the linear response by the refractive index n. It is apparent that the equation takes the form of a driven wave equation, with the polarization acting as a source term. We can thus directly see from Eq. 2.37 that the nonlinear response of the medium can result in the generation of new frequency components.

Notably, even order nonlinearities only appear in noncentrosymmetric materials. This is due to the symmetry properties of the second-order nonlinear susceptibility tensor vanishing for symmetric potential energy functions of the medium [41, Sec. 1.4]. In the context of this work, the relevant nonlinear effects are of second or third order, which means that they result from the terms $P^{(2)}(t)$ and $P^{(3)}(t)$, respectively. These two types of light-matter interactions will now be discussed in more detail. In the discussion below the involved electric fields will be treated as monochromatic plane waves of the form $E(t) = A_0 \exp(-i\omega t)$ for simplicity. However, the descriptions remain valid when A_0 is replaced by $A_0(\mathbf{r}, t)$. Throughout Sec. 2.5, an instantaneous response of the medium is assumed, which results in nonlinear susceptibilities which are independent of the frequency ω of the light field. In applications with ultrabroadband pulses, e.g. supercontinuum generation, the frequency dependence of the nonlinear response can become relevant.

2.5.1 Third Order Nonlinear Effects

Third order nonlinear effects generally appear in any kind of material independent of the material symmetry. Therefore, these effects are highly relevant for all applications and experiments involving intense light pulses. Third order nonlinear effects can be used to increase the spectral bandwidth of ultrashort pulses to allow for compression to even shorter durations. However, they can also lead to unwanted beam distortions.

The effects described below are all discussed in terms of a laser pulse with electric field $E(t) = A_0(t) \exp(i\omega_0 t)$ interacting with a medium. However, the description is still valid when superposition of multiple pulses are considered. Then the electric field is given by $E(t) = E_1(t) + E_2(t)$ and the third-order nonlinear polarization contains mixing-terms of the two fields which result in effects like cross-phase-modulation (XPM).

The Optical Kerr-Effect

Assuming a material exhibiting only third-order nonlinear effects, the nonlinear material polarization in response to the electric field is given by [41, p. 207 ff.]

$$P^{\mathrm{NL}}(t) = 3\epsilon_0\chi^{(3)}E(t)E^*(t)E(t) = 3\epsilon_0\chi^{(3)}|E(t)|^2E(t) \ . \tag{2.38}$$

Identifying $|A_0(t)|^2$ with the intensity I_0 of the light field, we can now describe the total response of the material by the polarization $P(t)$ as

$$P(t) = P^{(1)}(t) + P^{\mathrm{NL}}(t) = \epsilon_0\chi^{(1)}E(t) + 3\epsilon_0\chi^{(3)}I_0E(t) \ . \tag{2.39}$$

This result has an astonishing similarity with the case of a purely linear material response (see. Eq. 2.5). In analogy to the linear case, the refractive index can now be defined by

$$n^2 = 1 + \chi^{\mathrm{eff}} = 1 + \chi^{(1)} + 3\chi^{(3)}I_0 \ . \tag{2.40}$$

Therefore, the linear refractive index n_0 of the material is modified by an intensity dependent term due to the third order nonlinear response. The augmented refractive index is given by

$$n = n_0 + 2\tilde{n}_2I_0 \ . \tag{2.41}$$

Here the second-order index of refraction $\tilde{n}_2$ was introduced which is given by

$$\tilde{n}_2 = \frac{3\chi^{(3)}}{4n_0} \ . \tag{2.42}$$

This intensity dependent augmentation of the linear refractive index in the presence of an intense light field is called the optical Kerr-effect. It is easy to imagine how this effect can lead to distortions in Gaussian light pulses where I_0 is not a constant scalar. However, Eq. 2.41 is still valid in this case. By inserting the spatio temporal intensity envelope of the pulses $I(\mathbf{r}, t)$ it is possible to deduce the spatio-temporal distribution $n(\mathbf{r}, t)$ of the refractive index. Due to the refractive index depending on time and space, a light pulse traveling through a medium will experience a nonlinear phase shift given by

$$\Phi_{\mathrm{NL}}(\mathbf{r}, t) = -\tilde{n}_2\frac{\omega_0 L}{c}I(\mathbf{r}, t) \ . \tag{2.43}$$

Here, L is the propagation distance of the light pulse in the nonlinear medium and ω_0 is its center frequency. The amount of the accumulated nonlinear phase, is typically quantified by the B-integral [57, p.368]

$$B = \frac{2\pi}{\lambda}\int_0^L \tilde{n}_2I(z)dz \ . \tag{2.44}$$

The B-integral often serves as a measure for the strength of the accumulated nonlinearity and of the induced beam distortions.

Self-Focusing

The effects of the spatially varying refractive index are now discussed, considering a monochromatic Gaussian beam. In this case, there is no time-dependent shift in the

refractive index. The Gaussian beam exhibits a radially symmetric intensity distribution around the propagation axis (see Eq. 2.9 for $n = m = 0$). According to Eq. 2.41, this results in a radially symmetric augmentation of refractive index by the nonlinear response of the medium. The deviation from the linear refractive index will be higher in the center of the beam and lower the further one gets from the propagation axis. Therefore, the nonlinear response to the intense light beam essentially forms a lens. The form of this lens depends on the shape of the intensity profile of the pulses and is thus non-spherical for Gaussian beams. Therefore, compensating the nonlinear lense by insertion of optical elements is often not possible in practice. Typically, the second-order refractive index $\tilde{n}_2$ is positive and the pulse is thus focused by the nonlinear lens due to the intensity dependent refractive index. This effect is therefore called self-focusing. Self-focusing often leads to unwanted beam distortions and damage to optics in laser amplifiers and can even lead to the complete collapse of the beam when the focusing due to the nonlinear lens overcomes the natural divergence of the beam. The beam will focus until diffraction effects balance the self-focusing resulting in propagation at a constant size. This effect is also called *self-trapping* or *filamentation*. Such a collapse can happen whenever the peak power of a traveling light field at (center-)wavelength λ_0 exceeds the critical power of the material given by

$$P_{\text{crit}} = \frac{\pi\lambda^2}{8n_0\tilde{n}_2} \tag{2.45}$$

In this case, the light will reach its focus after a propagation distance of [57, p.329-331]

$$z_{\text{sf}} = w_0\sqrt{\frac{n_0}{2\tilde{n}_2 I_0}} \tag{2.46}$$

The detrimental effects of self-focusing clearly increase for higher intensities, higher values of $\tilde{n}_2$ and longer propagation distances in the medium. This makes them a limiting factor especially for high pulse energy amplifiers relying on long active materials such as fibers or slabs. Self-focusing, however, also has applications, for example in the supercontinuum generation by bulk filamentation discussed below.

Self-phase-modulation

I have discussed the effects of the nonlinear phase shift in the spatial domain. Let's now take a look at what happens in time. A short, intense light pulse with temporal intensity profile $I(\tilde{t})$ will introduce a nonlinear refractive index according to Eq. 2.41. Here, $\tilde{t}$ denotes the local time variable inside the envelope function. This results in a deviation from the linear refractive index n_0 which is the strongest in the center of the pulse at $\tilde{t} = 0$. This leads to a time dependent deviation of refractive index deviation from the linear value $\delta n(\tilde{t}) = 2\tilde{n}_2 I(\tilde{t})$. Fig. 2.5 shows the nonlinear refractive index deviation $\delta n(\tilde{t})$ induced by a pulse with a Gaussian temporal intensity distribution (blue curve). This time dependent refractive index leads to a nonlinear phase shift of

$$\Phi_{\text{NL}}(t) = -\tilde{n}_2\frac{\omega_0 L}{c}I(t)\ . \tag{2.47}$$

This introduction of a nonlinear phase caused by the intensity envelope of the short light pulse is called self-phase-modulation (SPM).

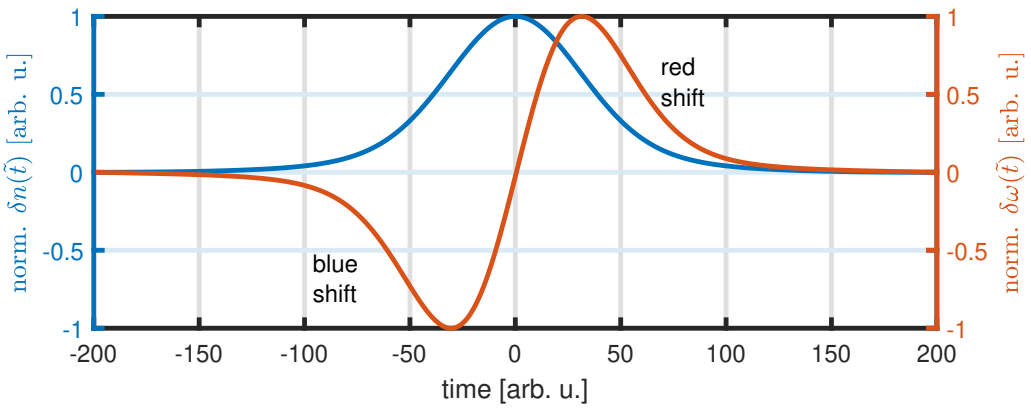

Figure 2.5: Depicted in red is the nonlinear refractive index $\delta n(t)$ induced by an ultrashort light pulse propagating in a χ^3-material with $\tilde{n}_2 > 0$. The time axis represents a copropagating reference frame with time zero in the center of the pulse. Depicted in blue is the self induced change in instantaneous frequency due to the nonlinear refractive index profile. The leading edge experiences a red shift while the trailing edge is blue shifted.

For $\tilde{n}_2 > 0$ this results in a higher refractive index in the center of the pulse and a lower refractive index on the trailing and leading edges. Thus the frequencies contained in this short pulse will experience a phase shift depending on time which is modifying the instantaneous frequency by $\delta\omega(\tilde{t})$.

$$\omega(\tilde{t}) = \omega_0 + \delta\omega(\tilde{t}) \ , \tag{2.48}$$

In the slowly-varying-envelope approximation, the change in instantaneous frequency can be expressed by

$$\delta\omega(\tilde{t}) = \frac{d}{d\tilde{t}}\Phi_{\mathrm{NL}}(\tilde{t}) = -\tilde{n}_2\frac{\omega_0 L}{c}\frac{d}{d\tilde{t}}I(\tilde{t}) \ . \tag{2.49}$$

The frequency shift $\delta\omega$ along the envelope of the light pulse is illustrated in Fig. 2.5 (red curve). It is apparent, that for $\tilde{n}_2 > 0$, the shift in the instantaneous frequency is positive at the trailing edge of the pulse and negative at the leading edge. Thus, the laser pulse experiences a blue shift on the trailing side and a red shift on the leading side. This effect is therefore associated with a symmetric spectral broadening of the pulse. The maximum frequency shift due to SPM can be estimated by Eq. 2.50

$$\delta\omega_{\max} \simeq \frac{\Delta\Phi_{\mathrm{NL}}^{\max}}{\tau_0} \qquad \text{where} \qquad \Delta\Phi_{\mathrm{NL}}^{\max} = \tilde{n}_2\frac{\omega_0}{c}I_0 L \ . \tag{2.50}$$

The maximum frequency shift thus depends on the intensity I_0, duration τ of the light pulse as well as length and nonlinear refractive index of the nonlinear medium L. Spectral broadening due to SPM will be relevant whenever $\delta\omega_{\max}$ exceeds the spectral width of the incident laser pulse. For a near bandwidth limited pulse, this means, that SPM results in significant spectral broadening when $\Delta\phi_{\mathrm{NL}}^{\max} \gtrsim 2\pi$. Spectra broadened purely by SPM show a characteristic symmetric quasi-periodic modulation around the initial laser wavelength [59, p.10].

Supercontinuum Generation by Bulk Filamentation

The term *supercontinuum generation* generally refers to the generation of an ultra-broadband, often more than octave-spanning spectrum by means of nonlinear broadening. Supercontinua can be generated from picosecond or shorter pulses in highly nonlinear fibers (HNF) [60], gas filled hollow-core waveguides [61] or bulk crystals [62]. The exact processes involved in the generation of the supercontinuum depend on the respective type.

Here, I will discuss the super continuum generation by filamentation in a bulk crystal. This approach is relevant for the seed-generation setup of the high-power SWIR-OPCPA setup and the f-2f-device for measuring the relative CEP used to characterize the phase stability of the pulses from both amplifiers presented in this work.

Supercontinuum generation by bulk-filamentation is mainly driven by the previously discussed effects of self-focusing and self-phase-modulation. If a short, intense pulse of light is incident on a nonlinear medium, it induces a nonlinear response. If the peak power of the pulse exceeds the critical power for self-focusing in the medium (see Eq. 2.45) the pulse collapses to a filament. Here I assume the focal spot is still located within the medium. The drastic reduction of the pulse dimensions leads to a strong increase in the peak intensity of the pulse. The high intensity in the filament gives rise to a strong nonlinear phase shift in the time domain duration of the pulse. Thus, the spectrum is broadened by strong SPM. Since the pulse is *self-trapped* and travels in the filament without expanding, the high intensity can be maintained for a long travel distance. Thus $\delta\omega_{\max}$ can reach extremely high values.

The SPM broadening process is further enhanced by several effects which lead to fast changes of the nonlinear refractive index in time. Self-steepening is an intrinsic property of the SPM process in materials with $\tilde{n}_2 > 0$. Due to its intensity dependency, the peak of the pulse experiences a higher refractive index than the edges. Therefore, the central part of the pulse travels slower than its trailing and leading parts. Thus, the trailing edge catches up with the peak of the pulse, resulting in a sharp intensity edge on the backside of the pulse. On the leading edge, however, the intensity gradient flattens out as it moves further and further ahead of the peak [59, p.82]. The sharp edge on the trailing edge results in a strong increase of the generated spectral bandwidth on the high frequency side of the spectrum. Other effects increasing the spectral bandwidth of the supercontinuum are connected to multi-photon excitation and plasma generation [63]. The complex interplay between nonlinear broadening and linear dispersion can, however, lead to pulse-splitting and thus the formation of multiple pulses. Generating stable supercontinua from pulses with durations longer than ~ 1 ps gets increasingly difficult. The high intensities necessary to initiate the filamentation process require either high pulse energies or tighter focusing. While the first is prone to generate multiple filaments, the latter increases the probability for laser induced damage [64].

2.5.2 Second Order Nonlinear Effects

While third order nonlinear effects happen in basically any material light can travel in, this is not true for effects caused by the second order nonlinear polarization. The nonlinear response of a medium can be described as an anharmonic oscillator. A second order nonlinearity can only arise, if the potential energy function of this

anharmonic oscillator is asymmetric. The potential energy function is given by [41, p.22, p.29]

$$U(\tilde{x}) = \frac{1}{2} m_{\mathrm{e}} \omega_0^2 \tilde{x}^2 + \frac{1}{3} m_{\mathrm{e}} a \tilde{x}^3 - \frac{1}{4} m b \tilde{x}^4 + \cdots \tag{2.51}$$

with an electron displacement $\tilde{x}$ and electron mass m_{e}. The parameters a and b characterize the strength of the respective nonlinearity. In this description, the term cubic in $\tilde{x}$ leads to an asymmetric potential energy with $U(\tilde{x}) \neq U(-\tilde{x})$. This cubic term vanishes in centrosymmetric media. Therefore, second-order nonlinearity is only observed in materials which are not centrosymmetric. I note here, that second order nonlinear effect can also be observed if the material symmetry is broken by other means. This can happen for example at a surface between two media with different refractive index.

As the second-order nonlinear susceptibility is much stronger than that of the third-order, second-order effects are typically dominant in noncentrosymmetric crystals. Therefore, the contribution of the third-order nonlinear polarization is neglected for now.

To achieve a general description of nonlinear effects it is convenient to investigate the nonlinear polarization induced by a superposition of two monochromatic light fields $E_1(t)$ and $E_2(t)$ at frequencies ω_1 and ω_2

$$E(t) = A_1 \exp(-i(\omega_1 t + \phi_1)) + A_2 \exp(-i(\omega_2 t + \phi_2)) + \text{c.c.}\ . \tag{2.52}$$

In this definition of the field, scalar phases ϕ_1 and ϕ_2 have been introduced to the two individual fields. Inserting this electric field into the second-order term of the polarization shown in Eq. 2.36 yields a second-order polarization $P^{(2)}(t)$ of

$$\begin{aligned} P^{(2)}(t) = \chi^{(2)} \vec{E}^2(t) = & \chi^{(2)} [E_1^2 \exp(-2(i\omega_1 t + \phi_1)) + E_2^2 \exp(-2(i\omega_2 t + \phi_2)) \\ & + 2E_1 E_2 \exp(-i(\omega_1 + \omega_2)t + \phi_1 + \phi_2) \\ & + 2E_1 E_2^* \exp(-i(\omega_1 - \omega_2)t + \phi_1 - \phi_2)] \\ & + 2\chi^{(2)} \left[E_1 E_1^* + E_2 E_2^*\right] \ . \end{aligned} \tag{2.53}$$

As discussed before, this second-order polarization acts as a source term in the wave-equation for the electromagnetic waves. All the second order nonlinear processes relevant for this thesis are contained in the polarization $P^{(2)}(t)$ shown in Eq. 2.53. The first two terms depending on $2\omega_1$ and $2\omega_2$, describe the SHG of the two incident light fields. The third term depends on $\omega_1 + \omega_2$ and thus describes the sum-frequency generation (SFG). The fourth term likewise describes the DFG, resulting in new spectral components at a frequency of $\omega_1 - \omega_2$. The last term is often called optical rectification. This term does not have a time dependence and therefore does not generate new field components, as its second time derivative is zero. The three-wave-mixing character of second-order nonlinear processes is also revealed in Eq. 2.53. In all of the time dependent terms, there are two photons from the incident field which are mixed to create one photon at a new frequency.

Notably we can see from the polarization that the phases ϕ_1 and ϕ_2 add up in the sum-frequency and second-harmonic fields. By contrast, in the difference frequency process, the phase difference $\Delta\phi = \phi_1 - \phi_2$ appears. This means that the phase of the generated frequency components will be determined by the phase of the incident light

waves and the generation process. This property is applicable to the CEP of ultrashort pulses. Therefore, it plays an important role in the generation of passively CEP-stable pulses by DFG. It is also crucial for the functionality of spectral interference devices for the measurement of the relative CEP, discussed in Sec. 2.7.2.

While these second-order nonlinear effects in principle can happen all at once, typically, only one of them is driven efficiently by a laser beam. Which new frequencies are generated is determined by two fundamental laws of physics.

The first of them is the law of energy conservation which allows only the creation of frequencies appearing in Eq. 2.53. The second fundamental law is momentum conservation, which limits efficient generation of new frequency components to the case $\Delta k = k_1 + k_2 - k_3 = 0$. Here, I assumed $k_1 < k_2 < k_3$. This condition is referred to as the *phase matching* condition. Phase matching will be discussed in more detail in Sec. 2.6 in the context of OPA. This process is the basis of nonlinear amplifiers such as the high-power SWIR-OPCPA-setup developed as part of this thesis which is presented in chapter 4.

2.6 Theory of Optical Parametric Amplification

Optical parametric amplification is a three-wave-mixing process relying on the second-order susceptibility $\chi^{(2)}$ of a nonlinear medium and is equivalent to DFG. Typically, an intense pump beam is used to amplify a weaker signal beam at lower frequency. Often, high pulse energy picosecond laser systems are used as a pump in optical parametric chirped pulse amplification (OPCPA). The concept of OPCPA is, however, fundamentally different from the CPA discussed previously. The chirp in this case is not meant to suppress nonlinear effects or laser induced damage. As there is no energy storage in the nonlinear medium, amplification can only occur in the spatio-temporal overlap region of the signal and pump beams. Therefore, efficient amplification can only be achieved if the pump and signal pulses have similar durations. This requires the introduction of chirp to the signal pulses which typically have much larger bandwidths. The principle mixing process is displayed in Fig. 2.6 a). In this process a third beam called the idler is generated.

Due to the large achievable amplification bandwidths and the flexibility in terms of emission wavelength, parametric amplifiers are complementing traditional ultrafast laser systems. OPA systems are especially useful for amplification of ultrashort pulses in frequency ranges where no suitable active laser crystals are available. Additionally, the OPA process does not rely on absorption of energy by an active medium. Thus, low absorption nonlinear crystals can be used reducing the thermal load in the amplification medium. The most simple description of the process can be given in a photonic picture. Due to the nonlinear polarization of the medium, a photon from the intense pump beam is broken up into two photons at the lower frequency. One of the photons contributes to the amplification of a copropagating signal beam. The second photon contributes to the generation of the idler. Due to the law of energy-conservation, the frequencies ω_1, ω_2 and ω_3 of the signal, idler and pump wave have to satisfy the condition $\Delta\omega = \omega_3 - \omega_2 - \omega_1 = 0$. This is illustrated in 2.6 b) for a signal beam containing multiple frequency components.

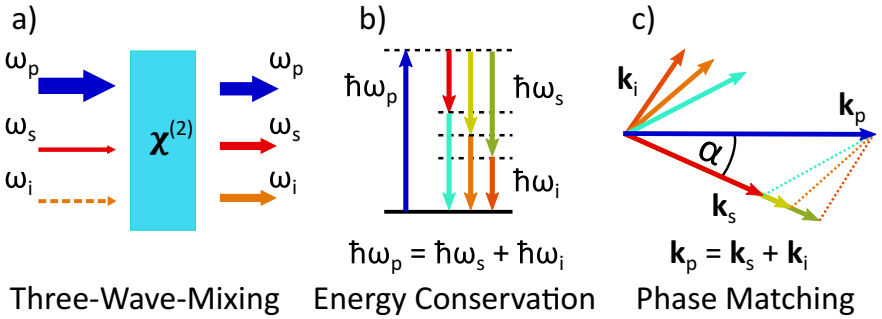

Figure 2.6: Schematic illustration of the OPA process. a) Principle geometry of the process. b) Energy level description illustrating the energy conservation condition. c) Wave vector addition diagram illustrating the phase matching condition $\Delta k = 0$. The diagram shows the general case with an angle α between the wave vectors of signal and pump.

2.6.1 The Coupled-Amplitude Equations for OPA

I will now discuss the fundamental equations describing the OPA process. The electric fields of the signal, idler and pump wave are given by

$$\begin{aligned} E_1(t) &= A_1 \exp(i(k_1 z - \omega_1 t) + \phi_1) && \text{(signal)} \\ E_2(t) &= A_2 \exp(i(k_2 z - \omega_2 t) + \phi_2) && \text{(idler)} \\ E_3(t) &= A_3 \exp(i(k_3 z - \omega_3 t) + \phi_3) && \text{(pump)} \\ &. \end{aligned} \tag{2.54}$$

Here, I assume a collinear propagation in z-direction for the three waves. Other spatial dependencies are neglected. The field amplitudes A_1, A_2, A_3 can take arbitrary values. In real applications, however, typically the inequality $A_3 >> A_1 > A_2 \approx 0$ applies. The combined electric field of the waves is then given by

$$\begin{aligned} E(t) = &\frac{1}{2}\left(A_3(z)e^{(i(k_3 z-\omega_3 t)+\phi_3)} + A_1(z)e^{(i(k_1 z-\omega_1 t)+\phi_1)} + A_2(z)e^{(i(k_2 z-\omega_i t)+\phi_2)}\right) \\ &+ c.c. \; . \end{aligned} \tag{2.55}$$

The electric field induces a second order nonlinear polarization $P_{\mathrm{NL}}^{(2)}$ according to Eq. 2.53 in the $\chi^{(2)}$-material. Assuming only terms with contributions from all three waves are taking place efficiently, a set of coupled equations can be derived. First the polarization is calculated from $E(t)$ according to Eq. 2.53, then the result is inserted into the wave-equation 2.37. This approach can be applied separately for the fields and polarization terms with common frequency. The results are the three coupled differential equations for the field along the propagation direction below

$$\begin{aligned} \frac{\partial A_1}{\partial z} &= -i\sigma_1 A_2^* A_3 \cdot e^{-i\Delta k z - e^{i(\phi_3 - \phi 2)}} \\ \frac{\partial A_2}{\partial z} &= -i\sigma_2 A_1^* A_3 \cdot e^{-i\Delta k z} e^{i(\phi_3 - \phi 1)} \\ \frac{\partial A_3}{\partial z} &= -i\sigma_3 A_1 A_2 \cdot e^{i\Delta k z} e^{i(\phi_2 - \phi 1)} \; . \end{aligned} \tag{2.56}$$

From these equation, it is apparent, that the change of the amplitude in each of the light fields depends on the strength of the other two. This property can be expressed by the Manely-Rowe-relations which, for the intensities I_1, I_2 and I_3 of signal, idler and pump beam taking the form [41, p.88]

$$\frac{d}{dz}\left(\frac{I_1}{\omega_1}\right) = \frac{d}{dz}\left(\frac{I_2}{\omega_2}\right) = -\frac{d}{dz}\left(\frac{I_3}{\omega_3}\right) . \tag{2.57}$$

2.6.2 Phase Matching

From Eq. 2.56, it is evident, that the amplitude of the involved fields will exhibit an oscillatory behaviour along the propagation axis z if the wave-vector mismatch Δk is non-zero. Therefore, in the presence of a wave-vector mismatch, energy conversion from the pump beam to the signal and idler beams slows down. Eventually the direction of energy flow is even reversed for longer propagation distances. This can be understood in terms of interference. If the phase-mismatch Δkz gets large enough, newly generated photons in the signal and idler waves interfere destructively and thus, energy is converted back to the pump beam. For an interaction length L, efficient amplification is only possible if the phase-mismatch satisfies $\Delta kL < \pi$. This is called the phase matching condition.

Perfect phase matching is achieved when the following condition is satisfied

$$\Delta\mathbf{k} = \mathbf{k}_3 - \mathbf{k}_2 - \mathbf{k}_1 = 0 \qquad \text{(phase matching)} . \tag{2.58}$$

Note here, that $\mathbf{k}$ is generally a vector. The vector-nature of $\mathbf{k}$ becomes relevant if the direction of the wave-vectors is not parallel for all three beams. This general situation is displayed in Fig. 2.6 c). In Sec. 2.1, I established the relation between the wave-vector, the oscillation frequency and the propagation speed of light $k = \frac{\omega n}{c}$. Using this identity and the phase-matching condition in Eq. 2.58, an equivalent description of the phase matching condition can be found

$$n_3\omega_3 - n_2\omega_2 - n_1\omega_1 = 0 \qquad \text{(phase matching)} . \tag{2.59}$$

It is evident from this equation, that phase matching cannot be achieved in materials with normal dispersion where the inequalities $n_3 > n_1$ and $n_3 > n_2$ apply, unless birefringence is involved. In a birefringent crystal, the additional degree of freedom of a polarization dependent refractive index allows to satisfy the condition in Eq. 2.59. To illustrate the principle behind birefringent phase matching, the phase matching conditions and refractive indices in case of an uniaxial and biaxial crystal are displayed in Fig. 2.7. For the sake of clarity, I consider a degenerate OPA involving monochromatic waves with $\omega_1 = \omega_2 = \omega$ and $\omega_3 = 2\omega$ in Fig. 2.7. Additionally, I consider collinear beam propagation. The characteristic property of birefringent crystals is that their refractive index depends on the polarization of the light propagating through them. For this thesis both uniaxial as well as biaxial birefringent crystals are relevant. In case of a uniaxial crystal such as β-barium borate (BBO) or magnesium doped lithium niobate (LNB) the material can be characterized by two different refractive indices and one optical axis c_o. Light polarized perpendicular to the optical axis experiences a refractive index n_o called the *ordinary refractive index*. Light polarized along the optical axis experiences the refractive index n_e referred to

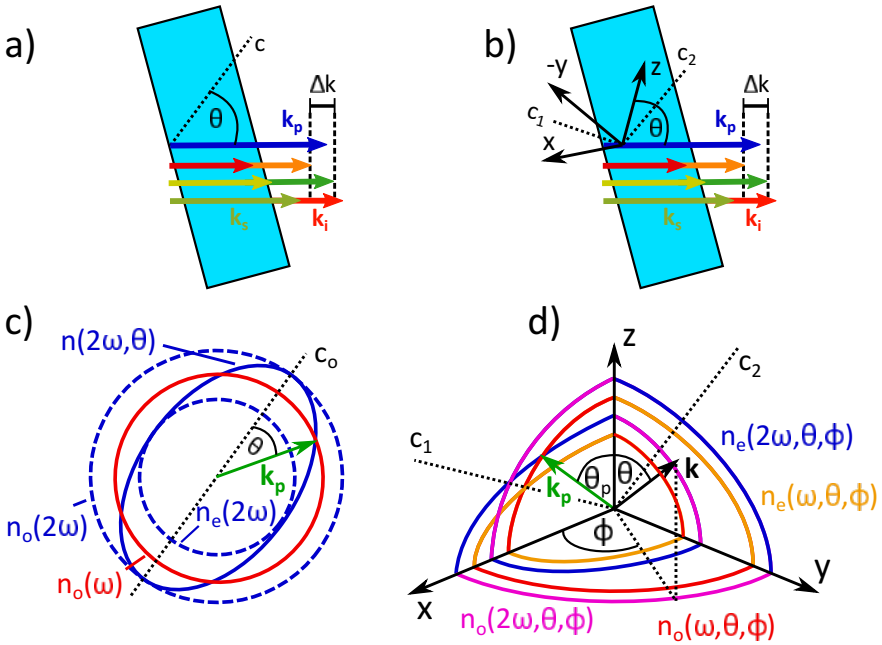

Figure 2.7: Refractive indices for a negative uniaxial a) and a biaxial crystals with $n_z > n_y > n_x$ b). In both cases, the values for the refractive indices do not represent a real crystal but were chosen to illustrate the phase matching conditions in the respective crystal type as clear as possible.

as the *extraordinary refractive index*. In Fig. 2.7 the case where $n_\mathrm{o}(\omega) > n_\mathrm{e}(\omega)$ is displayed. Such crystals are called negative uniaxial crystals. In positive uniaxial crystals $n_\mathrm{o}(\omega) < n_\mathrm{e}(\omega)$ applies. Often the terms *slow-axis* and *fast-axis* are used to refer to the direction of lower and higher refractive index, respectively. This description is independent of the type of crystal. In bi axial crystals, it depends on the plane of propagation whether the ordinary or extraordinary axis is the fast axis.

Phase matching can be achieved in uniaxial crystals by having one of the involved beams travel through the medium with a polarization perpendicular to that of the other two beams. Phase matching in the case where signal and idler are both polarized along the slow-axis and the pump beam is polarized along the fast axis are called *type-I phase matching*. Situations where either signal or idler are polarized perpendicular to the other two beams are referred to as *type-II phase matching*. To explain the phase matching in uniaxial crystals in more detail, let's assume a type-I phase matching process in a negative uniaxial crystal as shown in Fig. 2.7 a) and c). This is the case most relevant for this work. Both signal and idler are polarized perpendicular to the optical axis and experience the larger refractive index $n_\mathrm{o}(\omega)$. However, the pump beam is polarized in the plane set by the optical axis and the wave-vector of the pump beam. At an angle Θ between the optical axis and the wave-vector, the pump beam can experience any refractive index $n(2\omega)$ with $n_\mathrm{o}(2\omega) \geq n(2\omega) \geq n_\mathrm{e}(2\omega)$, depending on the value of Θ. These two boundaries are depicted as dashed blue lines in Fig. 2.7 c). The refractive index of the idler and signal wave is independent of Θ and is depicted as the red circle. In general, the refractive index for the pump wave can be described by

$$\frac{1}{n^2(\Theta)} = \frac{\cos(\Theta)}{n_\mathrm{o}^2(2\omega)} + \frac{\sin(\Theta)}{n_\mathrm{e}^2(2\omega)} \,. \tag{2.60}$$

The refractive index derived from this equation is displayed as a solid blue line in Fig. 2.7 c). The phase matching condition is met when all three waves experience the same refractive index. This is the case for phase matching angles Θ where $n(2\omega, \Theta)$ and $n_{\mathrm{o}}(\omega)$ have a crossing point.

For biaxial crystals such as bismuth triborate (BiBO), the situation is a bit more complicated. These type of crystals are characterized by three different refractive indices n_{x}, n_{y} and n_{z} along the crystals principle axis and have two relevant optical axis. The situation for the case of $n_{\mathrm{x}} < n_{\mathrm{y}} < n_{\mathrm{z}}$ is illustrated in Fig. 2.7 d). The figure displays the projections of the refractive indices on the three principle planes of the crystal. Those are the XZ-, XY-, and YZ-planes. Additionally to the phase matching angle Θ, another angle Φ is relevant in this case. The general principle of the phase matching, however, is the same as in the more simple case of a uniaxial crystal. Phase matching is achievable when there is a set of angles Θ and Φ where the refractive indices of all waves are equal. The refractive index n_3 of the pump light in the case of a biaxial crystal is determined by Eq. 2.61 [65]

$$\frac{\sin^2(\Theta)\cos^2(\Phi)}{n_3^{-2} - n_{\mathrm{x}}^{-2}} + \frac{\sin^2(\Theta)\sin^2(\Phi)}{n_3^{-2} - n_{\mathrm{y}}^{-2}} + \frac{\cos^2(\Theta)}{n_3^{-2} - n_{\mathrm{z}}^{-2}} = 0 \,. \tag{2.61}$$

In the example shown in Fig. 2.7 d), this is only possible if the waves travel in the XZ-plane ($\Phi = 0$). This situation is similar to the phase matching conditions in real BiBO crystals. I note here that the situation gets even more complex when considering nondegenerate and noncollinear OPA, however, the fundamental principle behind the birefringent phase matching is equivalent to the simple case discussed here.

2.6.3 Optical Parametric Gain

If the phase matching conditions are met, OPA allows for high gain signal amplification. Under the assumption of an undepleted pump beam and no incident idler wave, a simple description of the OPA gain after an interaction length L can be derived from the coupled amplitude equations in 2.56 [66]

$$G(L) = \frac{I_1(L)}{I_1(0)} = \left[1 + \left(\frac{\Gamma}{g}\sinh(gL)\right)^2\right] \simeq \left(\frac{\Gamma}{g}\right)^2 \frac{e^{2gL}}{4} \,. \tag{2.62}$$

I note here, that the second equality in Eq. 2.62 is only valid for the large gain limit where $gL \gg 1$. In the Equation, the gain coefficient g and the nonlinear coefficient Γ were introduced. Γ is given by

$$\Gamma^2 = \frac{2d_{\mathrm{eff}}^2 \omega_1 \omega_2}{c_0^3 \epsilon_0 n_1 n_2 n_3} I_3 \,. \tag{2.63}$$

and describes the strength of the nonlinear response. Therefore, it depends on the intensity of the pump light driving the process I_3 and the effective nonlinear coefficient d_{eff}. The parameter d_{eff} is determined from the second-order nonlinear tensor elements of the crystal and the propagation and polarization direction of the involved electromagnetic waves.

The gain coefficient g is now given by

$$g = \sqrt{\Gamma^2 - \frac{\Delta k^2}{4}} \,. \tag{2.64}$$

Evidently, the gain coefficient and therefore the gain depend strongly on Δk. Thus, strong amplification gain is only achieved under phase matching conditions. In case of birefringent phase matching, the amplification gain thus strongly depends on the phase matching angle Θ. For high gain amplifiers, the energy transfer from the pump to the signal and idler beams can lead to pump depletion and to the saturation of the gain effect. Eventually, a back-conversion process can set in transferring energy from signal and idler back to the pump beam. Those effects lead to strong spatio-temporal distortions as the gain depends on the spatial and temporal intensity distribution of the pulse. Therefore, saturation is not reached at the same interaction distance for all areas of the beam.

2.6.4 Amplification Bandwidth

Following the argumentation in [67], the amplification bandwidth $\Delta\nu$ of the OPA process is determined by the phase matching condition. Essentially, a high amplification bandwidth can be achieved if the phase matching condition $\Delta k \approx 0$ is fulfilled for a large frequency range. To determine, how this can be achieved, it is insightful to expand Δk in a Taylor-series around the center frequency ω_0 of the signal pulse

$$\begin{aligned}\Delta k = k_3(\omega_3) - k_1(\omega_0) - k_2(\omega_{20}) - \left(\frac{\partial k_1}{\partial \omega_1} - \frac{\partial k_2}{\partial \omega_2}\right)_{\omega_0} \Omega - \frac{1}{2!}\left(\frac{\partial^2 k_1}{\partial \omega_1^2} - \frac{\partial^2 k_2}{\partial \omega_2^2}\right)_{\omega_0} \Omega^2 \\ - \frac{1}{3!}\left(\frac{\partial^3 k_1}{\partial \omega_1^3} - \frac{\partial^3 k_2}{\partial \omega_2^3}\right)_{\omega_0} \Omega^3 - \frac{1}{4!}\left(\frac{\partial^4 k_1}{\partial \omega_1^4} - \frac{\partial^4 k_2}{\partial \omega_2^4}\right)_{\omega_0} \Omega^4 - \cdots \\ = \Delta k^{(0)} + \Delta k^{(1)}\Omega + \Delta k^{(2)}\Omega^2 + \Delta k^{(3)}\Omega^3 + \Delta k^{(4)}\Omega^4 + \cdots \,.\end{aligned} \tag{2.65}$$

Here, I introduced $\Omega = \omega_1 - \omega_0$ for the sake of brevity. The amplification bandwidth of the OPA is thus determined by the dominant term in the Taylor series. These terms $\Delta k^{(n)}$ satisfy the following condition

$$\Delta k^{(0)} > \Delta k^{(1)} > \Delta k^{(2)} > \Delta k^{(3)} > \Delta k^{(4)} > \cdots \,. \tag{2.66}$$

Therefore, the amplification bandwidth is determined by the lowest order term in the Taylor expansion which is not vanishing. To achieve broadband amplification it is required to reduce as many terms to zero as possible, starting at the lowest order. The Taylor-coefficients are now investigated individually. This provides insight into their nature and which conditions need to be met for them to vanish. Assuming the OPA process is phase matched at ω_0, the zeroth-order term $\Delta k^{(0)}$ will always be zero. The amplification bandwidth beyond the frequency of perfect phase matching is thus determined by the higher order Taylor-coefficients.

In general, the phase matching bandwidth is determined by $\Delta k^{(1)} = \left(\frac{\partial k_1}{\partial \omega_1} - \frac{\partial k_2}{\partial \omega_2}\right)$ and $\Delta\nu$ is given by

$$\Delta\nu^{(1)} = \frac{2(\ln 2)^{1/2}}{\pi}\left(\frac{\Gamma}{L}\right)^{1/2} \frac{1}{\left|\frac{\partial k_1}{\partial \omega_1} - \frac{\partial k_2}{\partial \omega_2}\right|} = \frac{2(\ln 2)^{1/2}}{\pi}\left(\frac{\Gamma}{L}\right)^{1/2} \frac{1}{\left|\frac{1}{v_{g1}} - \frac{1}{v_{g2}}\right|} \,. \tag{2.67}$$

It is evident from Eq. 2.67, that $\Delta\nu^{(1)}$ increases if $\Delta k^{(1)}$ gets small. According to the findings from Sec. 2.3.1, $\Delta k^{(1)}$ can be identified as the difference between the

inverse group velocities of the signal and idler pulse. The amplification bandwidth can therefore be increased if the group velocities of the signal and idler pulses are matched.

In this thesis, this is done by operating the OPA at the degeneracy point. With a pump beam at a wavelength of 1.03 μm and a signal beam centered at ~ 2.1 μm, group velocity matching is inherently achieved. Due to energy conservation, the generated idler pulse essentially contains the same frequencies as the signal pulse in degenerate OPA.

Another method to achieve group-velocity matching for nondegenerate OPA systems is the noncollinear OPA. In this approach, the three involved light fields are not copropagating. The k-vectors of the signal beam which is getting amplified and the pump beam are separated by an angle α. This angle is often referred to as the noncollinearity angle. Due to the law of momentum conservation, this also leads to an angle between the signal and idler wave-vectors. This situation is displayed in Fig. 2.6 c). Group-velocity matching can essentially be achieved under these conditions if the projection of the idler group-velocity v_{g2} on the propagation axis of the signal beam is equal to v_{g1}.

Interestingly, $\Delta\nu$ also depends on $\left(\frac{\Gamma}{L}\right)^{1/2}$ and therefore has a square-root-like dependence on the gain-coefficient and the inverse of the crystal length. However, the amplification bandwidth $\Delta\nu^{(1)}$ is dominated by the contribution from the group velocity mismatch.

If the group-velocities of signal and idler are matched, Eq. 2.67 is no longer a valid description of the amplification bandwidth. $\Delta\nu$ is now dominated by the second-order Taylor-coefficient from Eq. 2.65. It therefore can be described by

$$\begin{aligned}\Delta\nu^{(2)} &= \frac{2(\ln 2)^{1/4}}{\pi}\left(\frac{\Gamma}{L}\right)^{1/4}\frac{1}{\left|\frac{\partial^2 k_1}{\partial\omega_1^2}-\frac{\partial^2 k_2}{\partial\omega_2^2}\right|^{1/2}} \\ &= \frac{2(\ln 2)^{1/4}}{\pi}\left(\frac{\Gamma}{L}\right)^{1/4}\frac{1}{|(GVD)_1)-(GVD)_2)|^{1/2}}\,.\end{aligned} \tag{2.68}$$

This equation has been used to determine the amplification bandwidths for the different OPA crystals displayed in Tab. 4.1. If the group velocities of the signal and idler beams are matched, the amplification bandwidth is thus inversely proportional to the square root of the sum of the GVDs of the signal and idler pulses.

Ultra-broadband OPA can be achieved under conditions where $\Delta k^{(2)}$ also vanishes. However, this cannot be achieved universally. Only certain combinations of signal and pump wavelength which depend on the crystal in usage allow this condition to be met in a noncollinear geometry [68]. It is evident from both Eq. 2.67 and 2.68, that the amplification bandwidth also depends on the amplification gain coefficient and the inverse of the crystal length. Nonlinear applications with ultra-broadband pulses are often limited by the bandwidth of the nonlinear process. Therefore, a reduction of the crystal thickness in such applications can result in a significant increase in amplification bandwidth, if the associated reduction in the gain-coefficient can be compensated.

To illustrate the interplay between phase matching and amplification gain and amplification bandwidth, the small signal gain was calculated for three different crystals in a type-I phase matching geometry. The crystal properties were chosen to

match those of the crystals built into the three OPA stages of the high power SWIR OPCPA setup developed as part of this thesis. Fig. 2.8 shows the results depending on the wavelength and the phase matching angle Θ. The graphs in the top row show the calculated gain map for the three crystals. The graphs in the bottom row show the gain curves achieved at the phase matching angles marked by the blue, red and yellow lines. Generally, the behaviour is equivalent for all three crystals. However, the results show that the amplification bandwidth is the largest for the LNB crystal. Furthermore, it is evident from the results, that high gain can only be achieved when Δk is small (yellow areas in the top row) and that a high amplification bandwidth can only be achieved around the degeneracy point at 2.06 μm. If the phase matching angle is significantly detuned from phase matching at the degeneracy point, narrow band phase matching is achieved at two wavelengths to either side of the degeneracy wavelength.

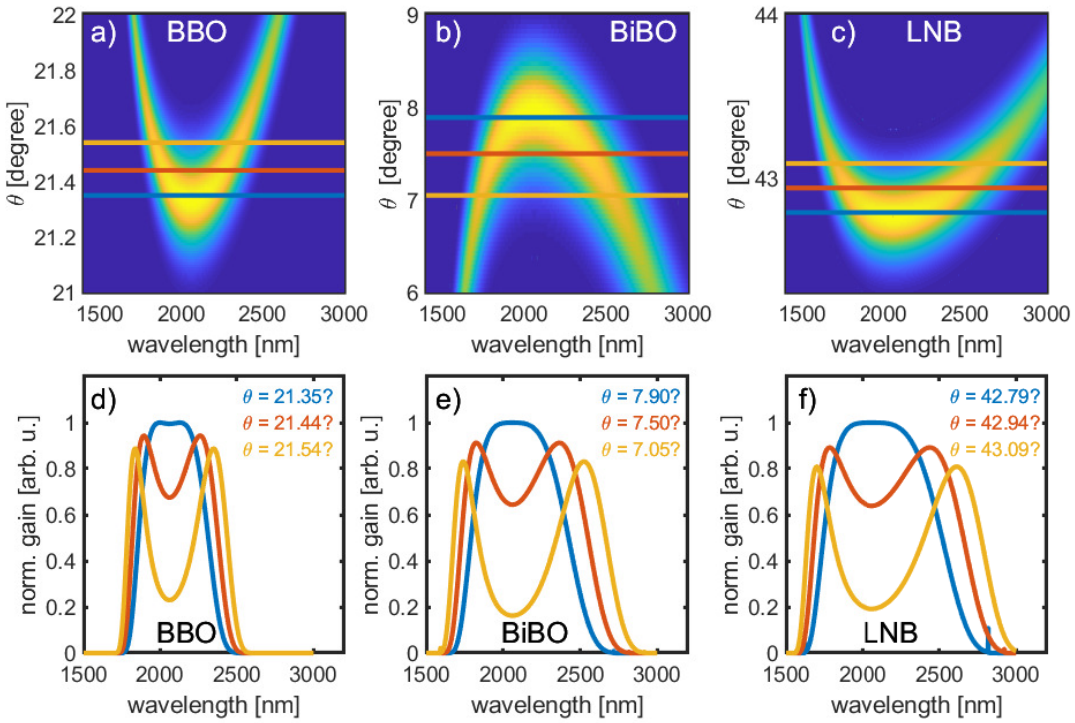

Figure 2.8: Amplification gain of a 1030 nm driven OPA process in the vicinity of the degeneracy point at 2060 nm. The small signal gain depending on the phase matching angle θ and wavelength λ was calculated for type-I phase matching in 4 mm BBO shown in a) and d), 2 mm BiBO schown in b) and e) and 2.2 mm LNB shown in c) and f). Here, d)-f) show cuts through the gain maps at the marked phase matching angles.

Notably, the amplification bandwidth can be increased by slightly detuning the phase matching angle from the degeneracy point. This situation is illustrated by the red gain curves in the bottom row of Fig. 2.8. Here, the increase of Δk starts limit the amplification gain at the degeneracy point in the center of the gain spectrum. In turn, Δk is decreased to either side of the degeneracy point which results in a larger gain bandwidth. This, however, also leads to an overall reduction of amplification gain.

2.7 Characterization of Ultrashort Pulses

2.7.1 Frequency-Resolved-Optical-Gating

Most experiments involving ultrashort pulses of light require detailed knowledge of the temporal properties of the pulses. These pulses have durations in the range from multiple pico- down to a few attoseconds. A direct measurement of the temporal intensity profile of pulses with such short duration cannot be achieved with electronic devices.

This problem was solved by self-referencing techniques. For a long time, auto-correlation setups where used to characterize ultrashort pulses. However, especially for pulses approaching only a few fs duration or with a complicated temporal structure, auto-correlation devices are not reliable due to the coherent artifact. This issue was overcome with the development of the frequency-resolved optical gating (FROG)-technique [69].

As part of this thesis, a second-harmonic-FROG device was built and used to characterize the pulses generated by the amplifiers. This section will give a brief overview of the operating principle of this type of measurement device. A schematic drawing of a SHG-FROG-device as it was used in this thesis is shown in Fig. 2.9. The pulse under investigation is split into two identical replica by a beamsplitter. The

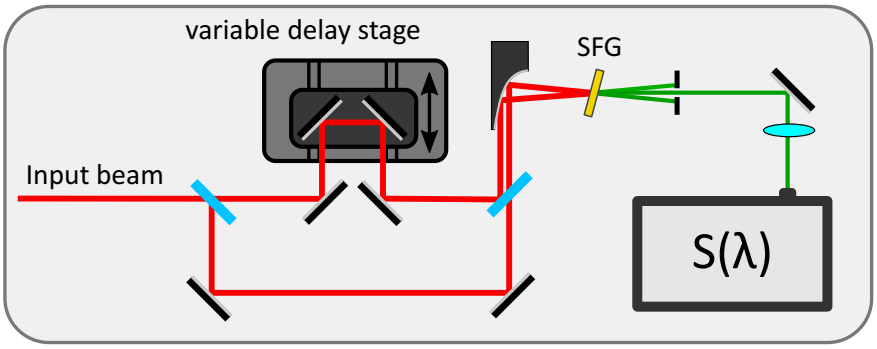

Figure 2.9: Schematic drawing of a SHG-FROG setup. A beamsplitter is used to split the pulse under investigation into two replicas. A motorized delay stage is used to adjust the time delay between the two replicas in one arm of the interferometer. Both replicas are focused into a nonlinear crystal for sum-frequency-generation (SFG). The resulting sum-frequency signal is detected by a spectrometer.

two replica travel through separate arms of an interferometer with a variable delay τ_d. At another beam splitter, the two replica are recombined parallel but noncollinearly. A parabolic mirror is used to focus the parallel beams into a material with a $\chi^{(2)}$-nonlinearity. Due to the parallel displacement of the beams, they are focused into the material under an angle. As described in Sec. 2.5.2, the two beams generate a sum-frequency signal which is detected by a spectrometer. The two beams themselves as well as their second harmonic are blocked at an aperture. Due to the angle between the beams and the law of momentum conservation the beam originating from the sum-frequency process has a different propagation direction. Therefore it is not blocked by the aperture. The sum-frequency spectrum is now recorded as a function of time delay τ_d between the two pulse replicas. The measured delay dependent spectral intensity of the sum-frequency is often referred to as the FROG-spectrogram. The spectral intensity $\mathrm{I}_\mathrm{FROG}(\omega, t)$ of the sum-frequency is given by [69]:

$$\mathrm{I}_{\mathrm{FROG}}(\omega, t) = \left| \int_{-\infty}^{\infty} \mathrm{E}(t)\mathrm{E}(t-\tau_{\mathrm{d}}) \exp(-i\omega t)\mathrm{d}t \right|^2 . \tag{2.69}$$

Calculating the complex electric field from the FROG-spectrogram is equivalent to solving a two-dimensional phase-retrieval problem [70]. Various recursive algorithms exist to retrieve the temporal intensity envelope and the spectral and temporal phases of the involved pulses by solving this phase-retrieval problem [71]. I note here, that in case of an SHG-FROG device, the solution is not explicit. There is a time reversal ambiguity due to the symmetry of the spectrogram around a delay of $\tau_{\mathrm{d}} = 0$. Therefore, it is not possible to identify which part of the retrieved pulse is the trailing and which the leading edge. For the characterization of the pulse duration, this loss of information is not relevant. To allow for a proper reconstruction of the pulse under investigation, all spectral components of the pulse need to be sufficiently phase matched. This can be problematic especially for ultra-broadband pulses. In the devices, used as part of this thesis BBO-crystals with a thickness of 10 μm - 100 μm have been used. The low thickness allows for sufficiently broadband mixing bandwidths to characterize the pulses relevant for this thesis. Generally, uncompensated frequency dependencies of the FROG signal can lead to a wavelength shift in the reconstructed spectrum. These effects can be corrected if the input spectrum of the investigated pulse is known [69].

2.7.2 Carrier-Envelope-Phase Measurements

A reliable detection mechanism for measuring the CEP of a laser pulse train is crucial for stabilizing and monitoring the CEP in experiments requiring stable electric field transients. Therefore, many techniques have been developed to measure the CEP of ultrashort pulses. The gold standard for CEP-measurements techniques are phase meters relying on above-threshold ionization (ATI) [72]. These devices allow for accurate single-shot detection of the absolute CEP-value at repetition rates of up to 100 kHz. However, stereo-ATI-phase meters require relatively high pulse energies > 10 μJ and few-cycle durations [73]. Additionally, the CEP-dependent signal measured by the device relies on electrons recolliding with their parent atom after acceleration by the electric field of the investigated laser pulse. Therefore, the signal is impeded by the characteristic scaling of the recollision probability with λ^{-5} to λ^{-6} at longer wavelengths. Thus, stereo-ATI phase meters are not the optimal choice for the laser setups developed as part of this thesis.

Instead, self-referencing spectral interference techniques have been used to characterize the CEP-stability of the output pulses of the two laser systems developed as part of this thesis. In comparison to sophisticated stereo-ATI-devices, these interferometry methods are easy to set up and operate, do not require large vacuum components and can be used to investigate the CEP of pulses with energies below the nJ level. However, they require a spectrum broad enough to allow for spectral overlap between the two pulses involved and are inherently not able to ascertain the absolute value of the CEP. The most common representation of this technique is the f-2f-interferometer, where the pulse under investigation is referenced against its second harmonic. A schematic drawing of the layout of such a device is shown in Fig. 2.10 a). The fundamental principle behind the retrieval of the relative CEP from the

interference pattern of the two pulses involved is, however, common for all related spectral interference techniques.

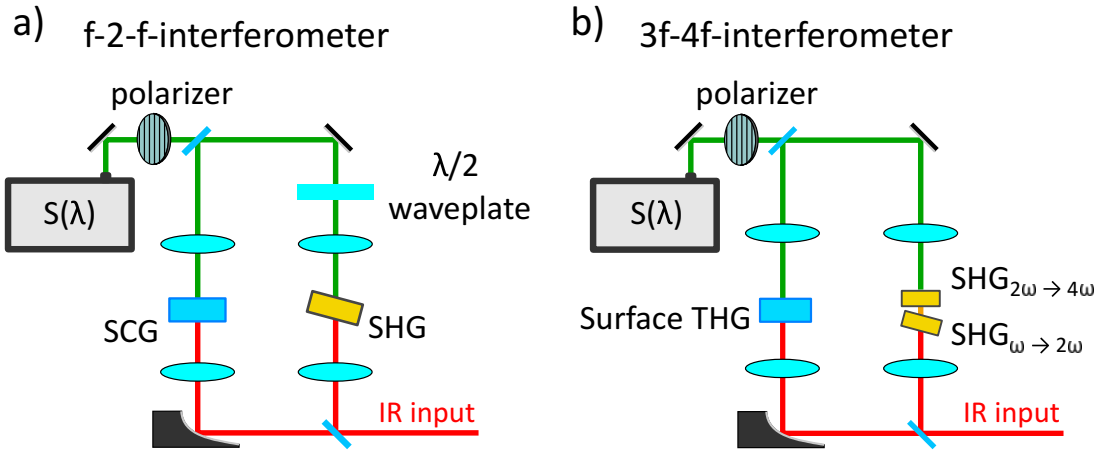

Figure 2.10: a) Layout of a noncollinear f-2f-interferometer. The two arms of the interferometer are used to generate the supercontinuum (SCG) and the second harmonic (SHG) separately. The overlapping spectral components of SC and SHG are then recombined collinearly and the interference pattern is detected with a spectrometer (S(λ)). b) Layout of a noncollinear 3f-4f-interferometer. Here, the interference between the third harmonic (THG) the 4th harmonic of the fundamental light is observed. This device can be used collinearly if the position of the two nonlinear crystals generating the 4th harmonic is adjusted carefully. Then the third harmonic can be generated from the surface of one of the nonlinear crystals.

As part of this thesis, a 3f-4f-interferometer was built for an accurate measurement of the relative CEP of the SWIR-pulses generated in the OPCPA-setup presented in chapter 4. This device does not require a supercontinuum generation and thus avoids the associated intensity-to-phase-noise coupling. Instead, the interference fringes between third harmonic and a fourth harmonic observed. This is only possible because of the high bandwidth of the SWIR pulses. The general layout of this device is displayed in Fig. 2.10 b). In this device, the fourth harmonic is generated in a cascaded SHG-process while the third harmonic is generated from the surface of a crystal. I note here, that the figure shows a noncollinear device. However, careful placement of the two crystals for the fourth harmonic generation allows to generate the third-harmonic from the surface of one of these crystals. Thus, the device displayed in Fig 2.10 allows for collinear operation. The two pulses are overlapped in space with a small time delay τ_d between them. As discussed in the beginning of this chapter (see. Eq. 2.2), the spectral intensity $S(\omega)$ of two interfering waves with intensities $S_1(\omega)$ and $S_2(\omega)$ contains an oscillating part. Assuming a collinear propagation, this oscillating term is given by $2\sqrt{S_1(\omega)S_2(\omega)}\cos\left(\omega\tau_\mathrm{d}+\Delta\phi\right)$ with $\Delta\phi=\phi_1-\phi_2$ being the phase difference between the two pulses. The phases ϕ_1 and ϕ_2 are not identical to the CEP of the pulses but also include other phase contributions such as quadratic phase terms related to GVD. However, in many cases, it is justified to assume that the CEP is the only phase contribution that is changing in time. Under this assumption, the phase of the interference fringes is given by $\Delta\phi(t) = \Delta\phi_\mathrm{static}+\Delta\varphi_\mathrm{ce}(t)$ with the time dependent difference between the CEP of the two interfering pulses $\Delta\varphi_\mathrm{ce}(t) = \varphi_\mathrm{ce}^{(1)}(t)-\varphi_\mathrm{ce}^{(2)}(t)$ and a static phase term $\Delta\phi_\mathrm{static}$ containing all other phase contributions. Thus, an observed change in the phase of the fringe pattern is

directly related to a change in $\Delta\varphi_{\mathrm{ce}}$.

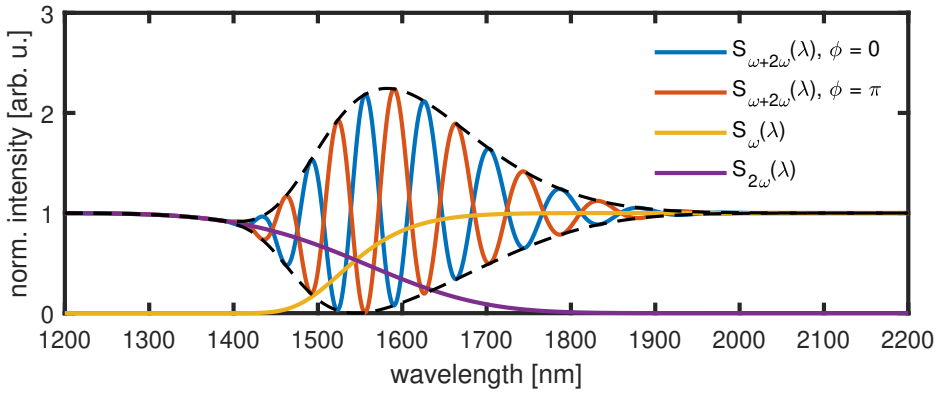

Figure 2.11: Spectral interference between two pulses with spectral intensity $S_{2\omega}$ (purple) and S_{ω} (yellow). Depicted in blue and red are the interference signals calculated for a phase difference of $\Delta\phi = 0$ and $\Delta\phi = \pi$. The dashed lines show the upper (B_1) and lower (B_2) boundary of the spectral fringes when $c_{\mathrm{f}} = 0$.

Fig. 2.11 shows the calculated spectrum created by interference of a pulse with spectral intensity $S_{\omega}(\lambda)$ and its second harmonic with spectral intensity $S_{2\omega}(\lambda)$ assuming a phase difference of $\Delta\phi = 0$ (blue) and $\Delta\phi = \pi$ (red) between the two pulses. In the overlap region of the two spectra, a distinct fringe pattern emerges with $B_1 = S_1^2(\omega) + S_2^2(\omega) + 2\sqrt{S_1(\omega)S_2(\omega)}$ and $B_2 = S_1^2(\omega) + S_2^2(\omega) - 2\sqrt{S_1(\omega)S_2(\omega)}$ as upper and lower boundary of the oscillation, respectively. The oscillation period in the frequency domain is determined by the delay τ_{d} between the two pulses and the position of the fringes is determined by $\Delta\phi$. We can now define a fringe contrast parameter $c_{\mathrm{f}} = A_{\mathrm{f}}(\omega)/(B_1 - B_2)$, where $A_{\mathrm{f}}(\omega)$ is the amplitude of the fringe pattern observed in the spectrum. Using this definition, both interference patterns in Fig. 2.11 have a contrast of $c_{\mathrm{f}} = 1$. This is, however, not generally the case. The spectral intensity $S(\omega)$ is a quantity that is integrated over the whole duration of the pulse. However, interference can only happen between spectral components overlapping in time. Thus, the fringe contrast is reduced depending on the delay τ_{d}. For the same reason, the fringe contrast decreases when chirped pulses are considered. Typically, these effects do not severely limit the performance of the detection device as the delay τ_{d} is chosen to be below the duration of the pulses. The effect of chirp is often negligible due to the narrow bandwidth of the spectral overlap region in realistic applications of the device.

There is, however, another important effect, which can reduce the contrast of an observed interference fringe pattern. Due to the limits in acquisition rate and minimum integration time of the spectrometer used in the device, single shot measurements are often not achievable. Thus, the recorded data is averaged over a number of n_p shots. In the presence of phase fluctuations, the averaging leads to a reduction in fringe contrast. This effect is illustrated by Fig. 2.12 showing fringe patterns created by interference of $S_1(\omega)$ and $S_2(\omega)$ averaged over $n_p = 500$ laser shots. A random phase with a Gaussian probability distribution was added to each of the pulses. Depicted in blue is the result of adding phase noise with a mean value of 0 rad and a standard deviation of $\delta_{\phi} = 1$ rad. The result of the averaging in the presence of phase noise

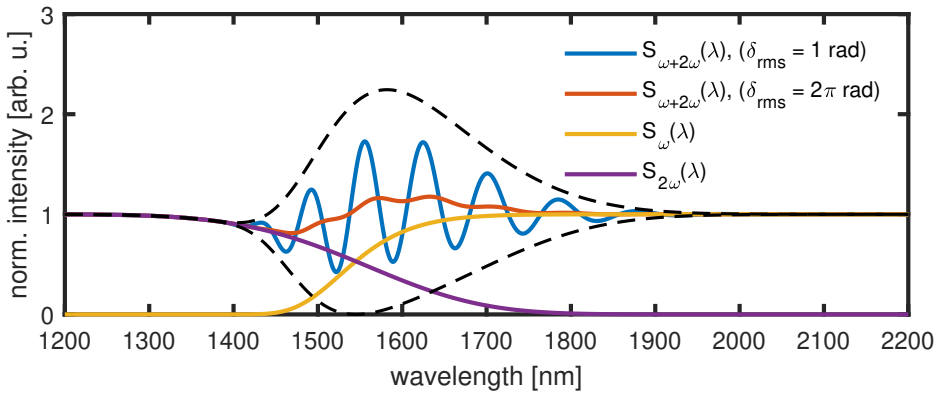

Figure 2.12: Interference of spectra averaged over multiple pulses in the presence of phase noise. The purple and yellow lines show the normalized average spectra of 500 pulses $S_{2\omega}$ and S_{ω} at the frequencies 2ω and ω, respectively. Depicted in blue and red are the calculated interference spectra according to Eq. 2.2. Phase noise with a Gaussian distribution, a mean value of zero and a standard deviation of $\delta_\phi = 1$ rad (blue) and $\delta_\phi = \pi$ was added to the oscillating term of Eq. 2.2. The dashed lines show the upper (B_1) and lower (B_2) boundary of the spectral fringes when $c_\mathrm{f} = 0$.

is again a periodic modulation on the interference spectrum. The amplitude of the modulations is, however, reduced compared to the theoretical maximum given by the dashed lines. A further increase of δ_ϕ results in a decrease of contrast. At a standard deviation of $\delta_\phi = \pi$ rad, the phase of each pulse is essentially random and the fringe contrast almost vanishes. I note here that the sum of cosine functions with random phase will yield again a cosine function according to the harmonic addition theorem [74]. Thus there will be a residual modulation observable when averaging over many pulses with a random CEP. The phase of this modulation, however, is purely random and does no longer carry information on the initial phase of the pulses. I note here, that in an experiment is averaging over a finite amount of pulses, there is however, a finite chance that the oscillation average out to zero. The reduction in fringe contrast depends both on the standard deviation δ_ϕ of the phase noise and on the number of pulses averaged. This is shown by Fig. 2.13, where a) shows the fringe contrast c_f depending on the number n_p of pulses being averaged for two different values of δ_ϕ. It is evident from the graph, that the fringe contrast drops from $c_\mathrm{f} = 1$ in case of a single pulse to a mean value $c_\mathrm{f}^{(\infty)}(\delta_\mathrm{rms})$ depending on the standard deviation of the applied phase noise.

Interestingly, the fringe contrast decreases only for the first 20 - 30 pulses being averaged. After that, the contrast reaches a steady level and a further increase of n_p has no effect on the average fringe contrast. As the reduction of the fringe contrast is a statistical effect, however, the spread around the mean value decreases with a larger number of average pulses. In Fig. 2.13 b) the fringe contrast is displayed depending on the standard deviation of the applied phase noise for three different n_p. The dashed lines show the upper boundary of $c_\mathrm{f} = 1$ observed for a single pulse and the mean value given by Eq. 2.70 for $n_\mathrm{p} \to \infty$

$$c_\mathrm{f}^{(\infty)} = e^{-\delta_\phi^2/2} \,. \tag{2.70}$$

Depicted in blue are the results averaging only two pulses. In this case, c_f is described by Eq. 2.70 only for $\delta_\phi \lesssim 0.1$ rad. At higher values of δ_ϕ, c_f is dominated by the

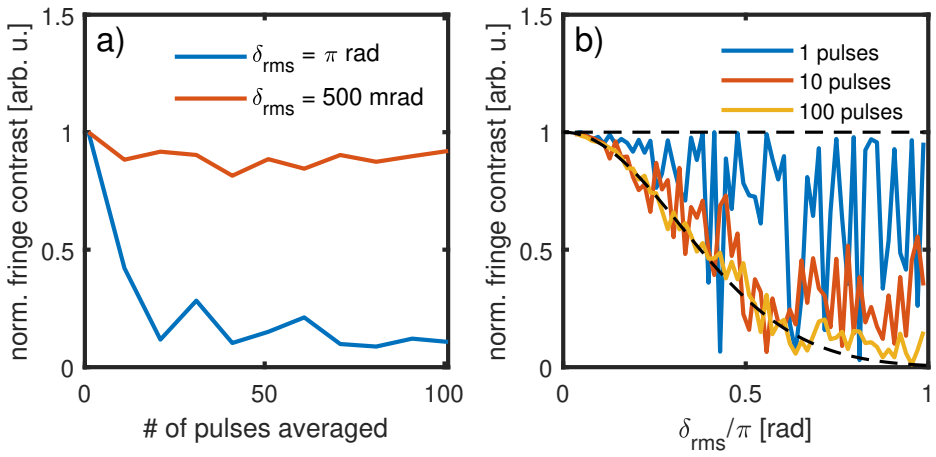

Figure 2.13: a) Calculated average contrast c_f of the spectral interference fringes depending on the number of pulses contributing to spectrum. Depicted in red are the results assuming a random additive phase term with a Gaussian probability distribution with 0 mean and a standard deviation of 500 mrad. Depicted in blue are the results when the standard deviation is increased to a value of π. b) Calculated average contrast c_f depending on the standard deviation of the added phase noise. The results have been calculated for 2 (blue), 10 (red) and 100 (yellow) pulses contributing to the signal. The dashed lines mark the upper limit of $c_f = 1$ achieved for a single pulse and the expected value $c_f^{(\infty)}$ for large numbers of pulses (see. Eq. 2.70).

increasing randomness of $\Delta\phi$. At $\delta_\phi = \pi$ rad, c_f assumes each value between 0 and 1 with the same probability. If the number of averaged pulses is increased the values follow the scaling in Eq. 2.70 more closely, even for higher $\delta\phi$. In fact, the rms deviation from $c_f^{(\infty)}$ scales with $1/\sqrt{n_p} \cdot (1 - \exp(-\delta_\phi^2/2))$.

Chapter 3

A High Power Nonlinear Yb:Yag Regenerative Amplifier

In the wake of efficient nonlinear compression tools for high pulse energy laser systems such as hollow core fibers [75, 76] and gas filled multi-pass cells [77, 78] , Yb:YAG-based laser systems have grown more and more interesting for directly driving ultrafast experiments. The feasibility of generating few-cycle pulses using these techniques combined with the high power capability of Yb:YAG-lasers make them interesting for strong field and attosecond experiments as the necessary pulse energies can be provided at repetition rates far beyond the limits of state-of-the-art Ti:sapphire lasers, accelerating data acquisition considerably. While CPA-based Yb:YAG-amplifiers can be compressed to fs-durations, the narrow bandwidth of the fundamental pulses requires multiple nonlinear compression stages to reduce the pulse duration to the few-cycle regime. Together with the need for large and costly grating-stretcher- and compressor-units, CPA-based few-cycle Yb:YAG-amplifiers can be an expensive investment with a rather large footprint.

An elegant solution to this problem is the direct amplification of femtosecond pulses in a nonlinear regenerative Yb:YAG-thin-disk amplifier [79, 80], overcoming the gain narrowing during amplification by nonlinear broadening in the laser resonator itself, capable of delivering multi-mJ pulses with few hundreds of fs pulse duration. This allows for few-cycle pulse generation in fewer nonlinear broadening stages while also avoiding the need for large stretchers and compressors based on gratings. Regenerative Yb:YAG-thin disk amplifier are especially well suited for generating pulse energies in the multi-mJ level at repetition rates $\geq$ 100 kHz making those types of amplifiers interesting for driving applications requiring high energies such as isolated attosecond pulse generation via HHG. To generate these isolated attosecond pulses, however, the driving IR-laser has not only to provide high energy few-cycle pulses but also has to be CEP-stable, a property that has not yet been demonstrated for Yb:YAG regenerative thin-disk amplifiers. Therefore the development of a CEP stable regenerative Yb:YAG thin-disk amplifier and investigating possible phase distortion mechanisms is highly desirable.

In scope of this project, a nonlinear Yb:YAG regenerative thin-disk amplifier has been built, which delivers pulses compressible to below 200 fs with an average output power of 200 W at a central wavelength of 1030 nm. The general layout of the amplifier is elucidated in section 3.1. The design criteria and achieved output characteristics

in terms of power, pulse duration and beam quality are discussed in section 3.2. In section 3.3 the performance of the amplifier regarding the CEP-stability of the output pulses is investigated. Section 3.4 evaluates the factors ultimately limiting the stability performance of the nonlinear thin-disk amplifier.

3.1 General Layout of the Nonlinear Regenerative Amplifier

The nonlinear regenerative thin disk amplifier built as part of this thesis is based on a development by Moritz Ueffing et al. [81]. A schematic overview of the setup is shown in Fig. 3.1.

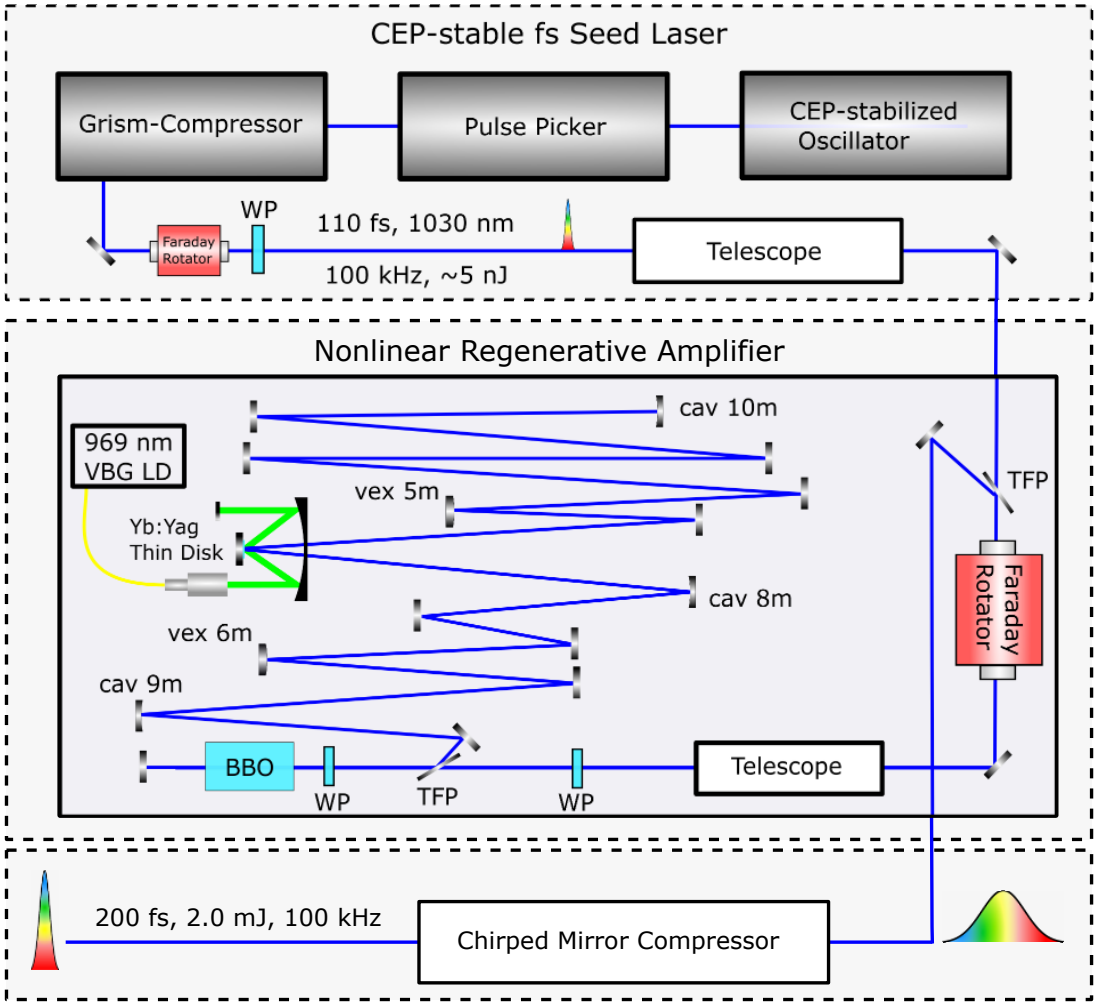

Figure 3.1: Schematic of the nonlinear Yb:YAG-thin-disk regenerative amplifier. VBG LD: volume Bragg-grating stabilized laser diode, TFP: thin film polarizer, WP: wave plate.

In contrast to CPA-systems this laser relies on direct amplification of femtosecond pulses generated in a CEP-stabilized oscillator (Menlo Systems GmbH ULN-FC1500). The oscillator operates at 100 MHz repetition rate and is stabilized to a carrier-envelope-offset frequency of 25 MHz, resulting in a pulse train with a CEP-shift of $\frac{\pi}{2}$

between successive pulses. Thus, every 4th pulse has the same CEP value. A commercial Pockels-cell pulse picker (Bergmann Messgeräte Entwicklung KG) including a 4 mm x 4 mm X-Cut rubidium titanyl phosphate (RTP) crystal is used to rotate the polarization of every thousandth pulse by 90°. The pulses with rotated polarization pass the thin-film-polarizer (TFP) after the pulse picker, while the other pulses are reflected into a beam trap. The pulse train passing the TFP has a repetition rate of 100 kHz and since the repetition rate is picked at a multiple of 4 pulses of the original rate, all the pulses have the same CEP. It is important to note here that the process of pulse picking can have a detrimental effect on the CEP of the pulses which is described in section 3.3. The pulses are compressed to a duration of 107 fs in a grism-compressor. To protect the seed laser from light propagating back from the main amplifier, an optical isolator was implemented in the beam path. To facilitate adjustment and optimization of the size and divergence of the seed beam, a beam expander (EKSMA Optics) is used, which increases the $1/e^2$ beam diameter to ≥ 1 cm and enables matching the incoming seed mode to the mode of the resonator in an easy-to-use fashion. The seed-beam is transmitted through a second optical isolator formed by a TFP and a Faraday rotator, which is used to separate the incoming seed from the amplified output beam. As this Faraday rotator is subject to the full output power of the amplifier, it is prone to laser induced damage. Therefore, it requires a large clear aperture to accommodate beam sizes as large as possible in order to avoid damage or nonlinear effects detrimental to the output beam quality. A mirror telescope between the Faraday rotator and the laser resonator is used to reduce the beam size to the ≈ 5 mm diameter required by the laser cavity. A $\frac{\lambda}{2}$-waveplate rotates the polarization of the incoming seed beam, allowing it to be coupled into the Cavity by passing through a TFP.

The amplifier resonator of this laser source is set up in a linear geometry, thus the beam is bouncing back and forth between two end mirrors. A $\frac{\lambda}{8}$-waveplate and a high voltage Pockels cell between the in-and out-coupling TFP act as an optical switch to trap the beam in the resonator by rotating its polarization. In the Pockels cell, a BBO crystal with a surface area of 12 mm x 12 mm and a length of 20 mm along the laser propagation axis is used. The high voltage for operating the Pockels cell is provided by a commercial Pockels cell driver (Bergmann Messgeräte Entwicklung KG) capable of supplying up to 14.5 kV and allowing for fast switching with a 15 ns rise time. When the beam first enters the cavity, the voltage on the Pockels cell induces a birefringence in the BBO-crystal effectively inducing another $\frac{\lambda}{8}$-shift. Both the waveplate and the Pockels cell are passed twice while the pulse travels from the TFP to the first end-Mirror and back. Thus, the phase shifts of the two elements adds up to a $\frac{\lambda}{2}$-shift, inducing a 90° rotation of the polarization. During the first round trip of the pulse in the cavity, the high voltage applied to the Pockels cell crystal is reversed and the Pockels cell is now effectively compensating the $\frac{\lambda}{8}$-waveplate. Therefore the polarization of the pulses is unimpeded while traveling through the setup. The pulses are trapped in the cavity until the high voltage at the Pockels-cell is reversed again resulting in a rotation of polarization and allowing them to leave the cavity.

While kept inside the laser cavity, the pulses pass the active medium of the Yb:YAG-thin disk twice per round trip. The Yb:YAG-disk itself has a diameter < 10 mm-diameter and a thickness ¡200 μm. It is bonded to a diamond substrate which is efficiently cooled by a stream water on its backside. The pump light pro-

vided by a volume-Bragg-grating stabilized 969 nm diode laser from (DILAS Diodenlaser GmbH) with $\geq$ 1000 W of output power capability. A pump light cavity (TRUMPF Laser GmbH) folds the pump light 18 times onto the same spot on the disk, which ensures efficient pump light absorption and good population inversion in the active medium within the pump spot.

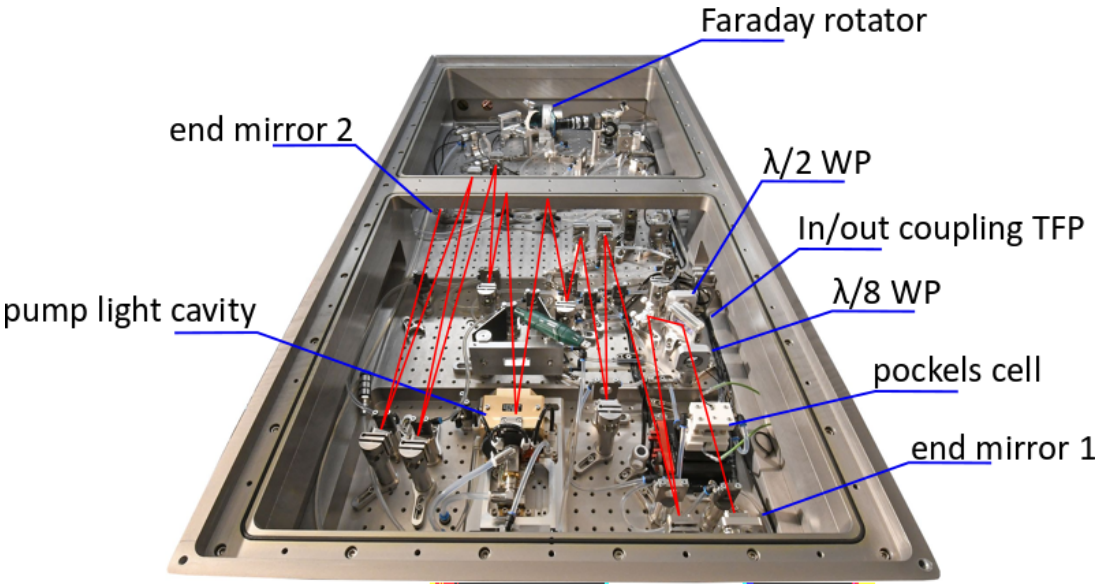

Figure 3.2: The nonlinear regenerative Yb:YAG-thin-disk amplifier.

Fig. 3.2 shows an image of the nonlinear regenerative amplifier, highlighting the most important components. The approximate beam path insight the laser resonator is highlighted in red.

3.2 Nonlinear Amplification

The concept of the nonlinear regenerative amplifier built as part of this thesis was developed by Moritz Ueffing and is described in detail in [79]. This section gives a quick overview of the unique features of the nonlinear regenerative amplifier as a concept and the laser system described above specifically. In particular, the design criteria and crucial parameters for its functionality are illustrated. The purpose of this project was the direct amplification of CEP-stable femtosecond pulses to multi-mJ energies, thus avoiding a CPA-based approach. This, however, puts a severe limitation on the number of possible laser concepts. The amplifier involved has to be capable of withstanding high energy pulses with durations on the scale of picoseconds rather than ns typical for CPA-based laser systems. Therefore, using a concept based on fibers or slabs which require the pulses to have a long propagation distance inside the active medium is challenging due to the prevalence of nonlinear effects such as self-focusing. While direct nonlinear high power amplifiers based on fiber concepts exist, they typically operate at MHz repetition rate and cannot provide the multi-mJ output energies necessary for driving HHG setups.

Using an active medium in form of a thin disk, however, is less prone to catastrophic self-focusing as the active medium has only a thickness of $\sim\ 100 - 500\mu$m.

Thus the damage threshold of the laser system as a whole is mostly governed by the optical switch which is typically a Pockels cell including a BBO-crystal, which allows much larger beam diameters than the active medium of a fiber- or Innoslab-amplifier. As the laser is meant to deliver multi-mJ pulse energies at a repetition rate of 100 kHz, the active medium is also subject to high power radiation from the pump laser as well as the amplified pulses. Fortunately, thin-disk active media offer effective heat removal by water cooling the backside of the substrate due to the low thickness and therefore beneficial surface to volume ratio of the material. However, as the active medium is thin, amplifiers relying on thin disks have limited single pass gain and therefore require many passes over the disk to amplify nJ pulses to the multi-mJ range. This can be done in a multi-pass configuration for booster amplifiers typically having a low gain factor of 10 to 100. Thin-disk amplifiers which increased the pulse energy of an incoming seed pulse by 6 or more orders of magnitude, however, have to rely on the regenerative amplifier concept. Therefore, a regenerative Yb:YAG-thin-disk amplifier is the best choice for direct amplification of nJ, femtosecond pulses from a CEP-stable oscillator to multi-mJ energies at ≥ 100 kHz repetition rates.

However, building a laser allowing for high power, high pulse energy and short duration of the amplified pulses still is challenging.

Due to the high power and peak intensity of the pulses propagating in the resonator thermal and nonlinear lenses emerge. These lenses alter the propagation conditions for the pulse and change significantly with the applied pump power. Due to the increasing pulse energy, the propagation conditions are also different for earlier or later round trips during the amplification cycle. The nonlinear regenerative amplifier presented here was carefully designed to allow for stable operation over the full pulse energy range from 2 nJ to 2 mJ. Following the guidelines provided in [79], this is achieved by a resonator design which exhibits minimal change in the beam size on the thin-disk active medium when subject to an additional nonlinear lens at position of the Pockels cell. Fig. 3.3 a) displays the diameter of the beam while propagating through the cavity for the low energy limit and at 2 mJ of pulse energy. The calculated diameter shows only a small change in beam size on the disk when the nonlinear lens introduced by the 2 mJ energy pulses is taken into account. The calculation was done using a cavity calculation software written by Moritz Ueffing [79] relying on the ray transfer matrix formalism described in Sec. 2.2. However, as can be seen in Fig. 3.3, the nonlinear lens induced in the Pockels cell crystal results in a decrease of the beam diameter on the back end-mirror which is ultimately limiting the pulse energy achievable from the laser due to the damage threshold of the dielectric mirrors. Additionally, if the peak power of the pulse exceeds the critical self-focusing power of the BBO, the pulses will even collapse as the focusing due to the nonlinear lens exceeds the natural divergence of the beam eventually leading to the creation of a filament or damage to the medium.

In contrast to CPA based setups, the nonlinear regenerative Yb:YAG-thin-disk amplifier is directly seeded with ~ 100 fs pulses from a fiber oscillator. Due to gain narrowing and dispersion, the pulse duration increases to multiple picoseconds during the amplification process, which is still considerably shorter than the ns pulse durations typically used in CPA-based setups. Therefore, the peak intensity of the pulses inside the cavity is much larger. This circumstance enables the intra-cavity broadening allowing to generate pulses with a bandwidth beyond the width of the

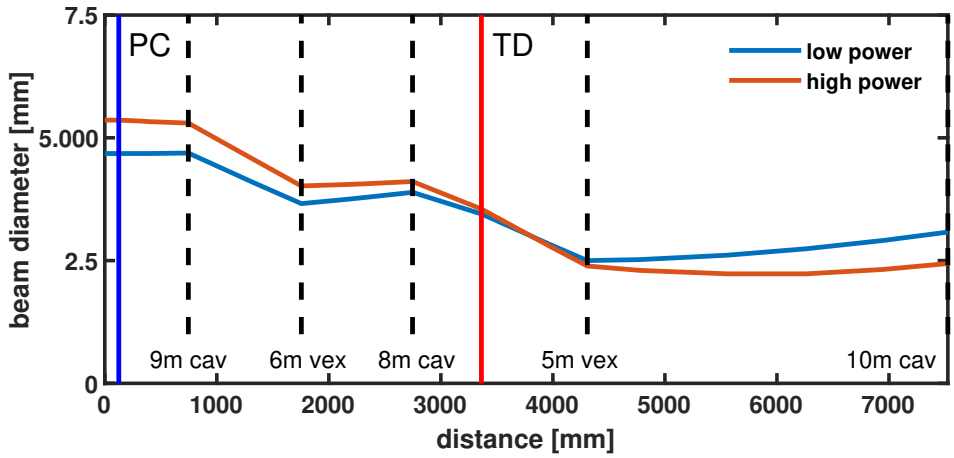

Figure 3.3: Calculated resonator mode of the nonlinear regenerative amplifier. The high power data includes a refractive element at the position of the Pockels cell corresponding to the nonlinear lens induced in the 20 mm BBO of the Pockels cell by pulses with an energy of 2 mJ. The resonator design was optimized to keep the beam diameter at the thin disk stable for pulse energies ranging from the few nJ input energy to 2 mJ to avoid mode instabilities and loss of amplification efficiency.

gain spectrum of the active medium. However, it also sets a limit for the highest achievable power at a given repetition rate due to catastrophic damage to the cavity optics as soon as the peak intensity exceeds the damage threshold. Typically the optics most susceptible to damage are the Pockels cell BBO-crystal and the 5 m convex mirror placed at the position of minimum beam diameter inside the cavity (see Fig. 3.3). In the case of the laser system demonstrated here, the maximum output power that allowed stable long-term operation was 210 W. Fig. 3.4 shows a measurement of the amplifiers output power for a time span of > 120 min, demonstrating excellent power stability with only 0.3 % rms average power fluctuations. The pulse-to-pulse stability was measured to be < 1 % using a fast silicium (SI) photo diode with a 120 ps rise time and an oscilloscope, however, this value can only be regarded as an upper limit as the measurement was already limited by the 10 $\frac{\mathrm{GS}}{\mathrm{s}}$ sampling rate of the oscilloscope.

Scaling the achievable pulse energy of such a nonlinear amplifier to even higher levels is limited by the dimensions of the available BBO-crystals used as an electro-optic switch. As the amplifier is utilizing the fact that the spectrum of the pulses is broadened by SPM inside the cavity, the output spectrum of the amplified pulses depends on the energy, spatial profile of the pulses and the number of round trips inside the cavity. Thus, the nonlinear propagation conditions inside the cavity need to be tailored to the desired output power to ensure sufficient spectral broadening. Here, the cavity is designed to achieve optimal broadening conditions at an output pulse energy of 2 mJ after 129 round trips when the cavity is purged with dry air. The usage of dry air inside the cavity is beneficial since the refractive index and effective nonlinearity of air depend on its humidity. Thus, using ambient air conditions results in unwanted performance changes of the laser due to weather-related changes in air humidity.

The output spectrum achieved at an output power of 200 W is displayed in Fig. 3.5 (blue curve). Additionally, the figure shows the output spectrum at low ener-

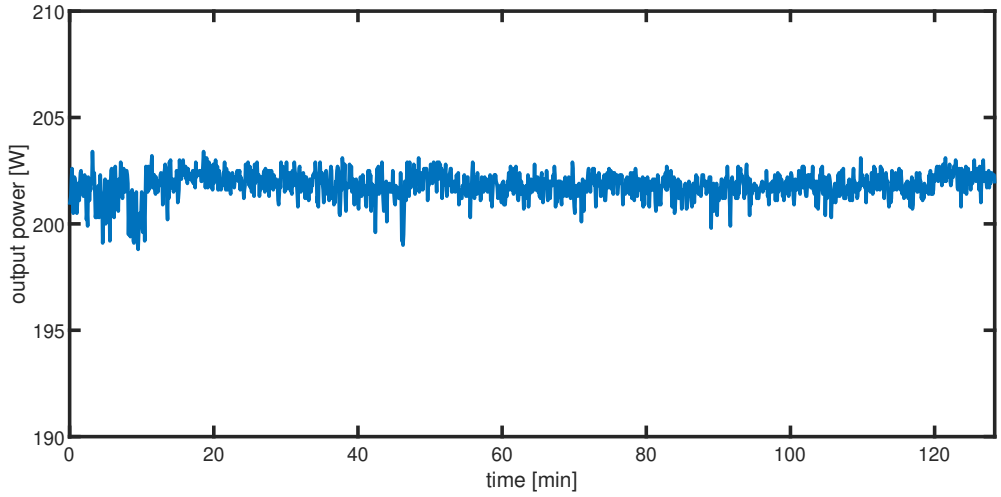

Figure 3.4: Measurement of the output power of the nonlinear regenerative amplifier for multiple hours of operation after the laser reached a thermal equilibrium. The average output power is 202 W with rms fluctuations of 0.3 %.

gies before the onset of nonlinear broadening. The spectrum at 2 mJ ranges from 1020 nm to 1037 nm exceeding the $\sim$ 4 nm amplification bandwidth of the Yb:YAG amplifier without intra-cavity nonlinear broadening. The spectrum has the modulated shape typical for pulses broadened by SPM. The peak in the spectrum at the original wavelength of the Yb:YAG amplifier of 1030 nm is enveloped by two side peaks generated by the nonlinear propagation inside the cavity. Theoretically, higher bandwidths could be achieved at higher pulse energies or a larger amount of round trips. In reality, however, the achievable spectrum is limited by the damage threshold of the Pockels-cell and the large dispersion in the setup leading to pulse breaking.

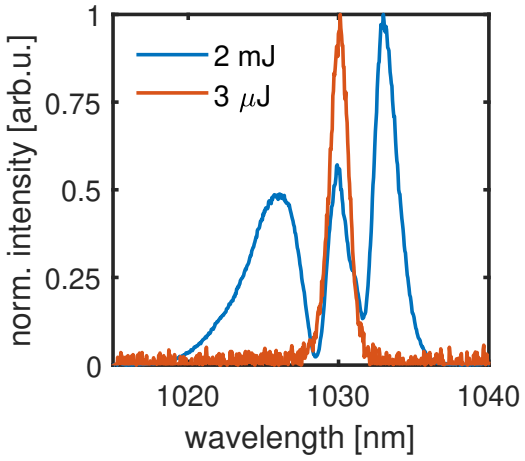

Figure 3.5: Output spectrum of the nonlinear regenerative amplifier at 2mJ pulse energy (blue) and at powers below the onset of nonlinear broadening (red).

However, the fact that the broadband spectrum originates from the nonlinear

propagation of the pulses in the resonator is also limiting the flexibility of the laser system as a broadband spectrum can only be achieved if the output pulse energies and number of round trips are close to the design values of 2 mJ and 129 round trips.

Following amplification to multi-mJ energies, the pulses were compressed using a chirped mirror compressor with 30 bounces on highly dispersive mirrors, allowing for a stable, low-loss compression. The temporal structure of the pulses after compression was characterized using a home built SHG-FROG setup as described in Sec. 2.7.1. Fig. 3.6 displays the results of a FROG measurement of the compressed 2 mJ pulses. The good agreement between the measured and reconstructed FROG-traces in Fig. 3.6 a) and b) and the reconstructed and measured spectrum in Fig. 3.6 c) are an indication for the reliability of the measurement. The temporal reconstruction displayed in Fig. 3.6 d) shows 191 fs near-Gaussian temporal profile of the compressed multi-mJ pulses. While there are small post- and pre-pulses surrounding main pulse, which are typical for spectra broadened by SPM, the main pulse still contains 80% of the total pulse energy.

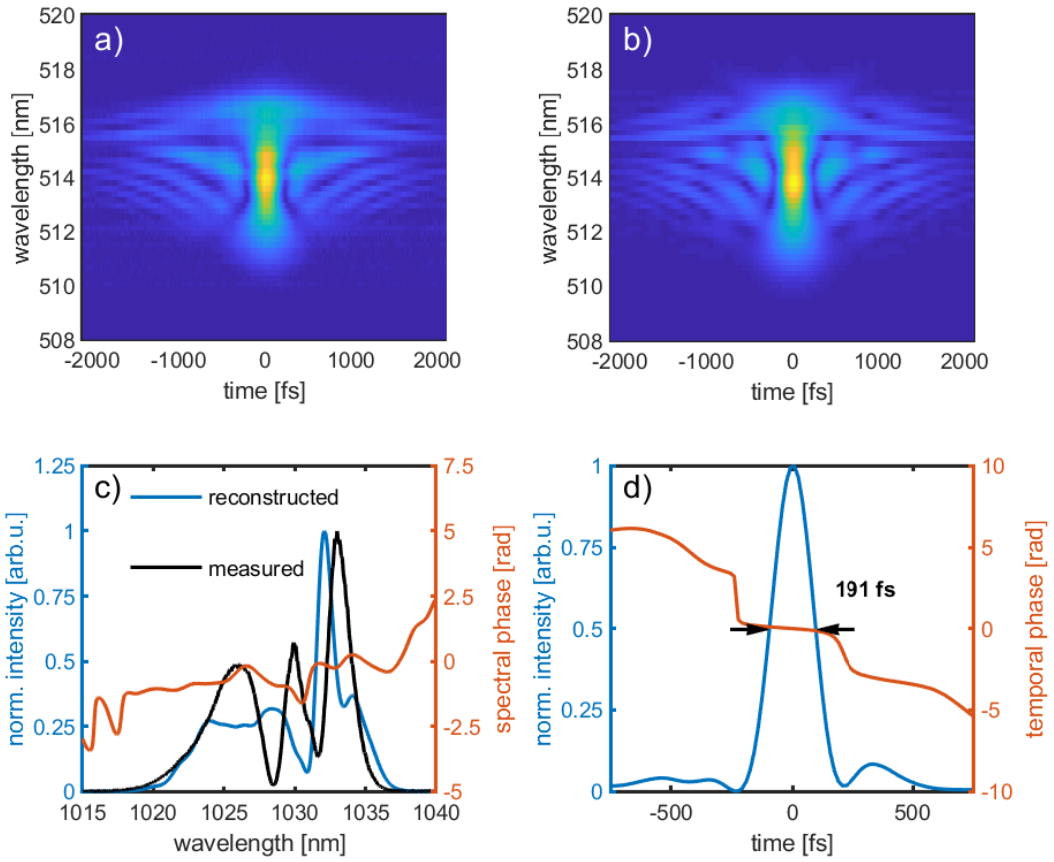

Figure 3.6: SHG-FROG measurement of the 200 W output from the nonlinear regenerative amplifier after compression in a chirped mirror compressor. a) Measured (black) and reconstructed spectrum (blue) and spectral phase (red) of the 2 mJ output pulses. b) Reconstructed temporal profile (blue) and temporal phase (red).

The high beam quality, sub-200 fs duration and > 2 mJ energy of the pulses from the nonlinear regenerative amplifier are excellent preconditions for further nonlinear compression to few-cycle pulse durations in multi-pass cells [77] and (stretched-)hollow-core fibers (HCF) [75]. These broadening techniques as well as many experiments rely on a good spatial beam profile and focusability of the involved laser beams. The parameter typically used to characterize this property is the M^2-beam quality parameter described in section 2.2. Fig. 3.7 displays the result of an M^2-measurement of the 2 mJ output beam of the amplifier after compression in the chirped mirror compressor using a commercial M^2-measurement device (Ophir Spiricon, BSQ-SP920). The measurement resulted M^2 values of $M_X^2 = 1.08$ and $M_Y^2 = 1.07$ in x- and y-direction, respectively. Additionally, it is evident from the measurement data that the pulses from the nonlinear regenerative amplifier only have minor spatial distortions in terms of astigmatism and ellipticity of the spatial intensity distribution. The beam profile, displayed in the inset of Fig. 3.7 shows the near-Gaussian spatial intensity distribution of the output after the chirped-mirror (CM)-compressor.

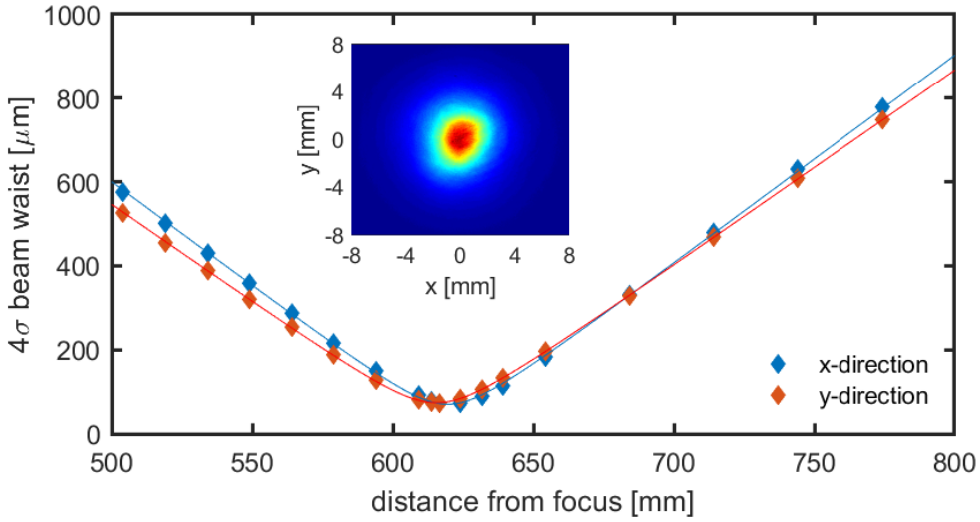

Figure 3.7: M^2 measurement of the compressed output beam. The inset shows the beam profile of the 2 mJ pulses after compression in the CM-compressor.

The nonlinear regenerative amplifier combines high pulse energy, high repetition rate and high beam quality with low average power noise and short pulse duration directly from the amplifier. Its unique performance makes this laser system interesting for experiments in strong field physics, attosecond spectroscopy and transient molecular fingerprinting. However, many experiments rely on utilizing or probing effects sensitive to the electric field of the involved laser pulses. Therefore, a stable phase relation between the envelope and the carrier wave for all pulses in the laser pulse train is required in addition to the stable amplitude of the envelope. Therefore, one purpose of this project was to explore the feasibility of the amplification of CEP-stable pulses in the nonlinear regenerative amplifier, which will be investigated in the following sections.

3.3 Carrier-Envelope-Phase Measurements

A stable CEP is a key requirement for many state-of-the-art applications in ultrafast laser science. Yet, CEP stable high power Yb:YAG regenerative thin disk amplifiers have not been demonstrated so far. While CEP-stabilized high power Yb:YAG thin-disk oscillators [82] and fiber lasers [83] exist, those setups are limited in pulse energy or rely on coherent combination of multiple sources, severely increasing the complexity, size and cost of such systems. Thus CEP-stable lasers based on Yb:YAG are generally quite rare. One reason for the general lack of CEP-stable Yb:YAG sources is the low amplification bandwidth of the gain material, preventing direct amplification of ultrashort pulses in CPA-based systems. However, many CEP-dependent effects observed in experiments become relevant only for short pulses in the few-cycle regime, where a strong effective field strength asymmetry between pulses with a CEP of $\varphi_{\mathrm{ce}} = 0$ and $\varphi_{\mathrm{ce}} = \pi$ can be observed (see Sec. 2.3.2). Thus, CEP-stability was not a primary design criterion for Yb:YAG-based laser systems with pulse durations typically ranging from hundreds of femtoseconds to picoseconds. However, recent developments in nonlinear broadening techniques for high power laser systems make a few-cycle compression of multi-mJ pulses from Yb:YAG amplifiers feasible [77, 84, 75, 76].

To explore the feasibility of direct amplification of CEP-stable pulses, the nonlinear regenerative Yb:YAG thin-disk amplifier developed as part of this thesis was seeded by a CEP-stabilized oscillator with a built-in phase control device allowing for the implementation of a fast feedback loop to stabilize phase noise introduced by the amplifier or applying phase modulations for CEP-dependant experiments. The relative carrier envelope phase of the pulses from the oscillator was measured before and after amplification by using spectral interference technique described in Sec. 2.7.2 with noncollinear f-2f-interferometers. Neither the seed nor the output of the amplifier, however, doesn't have an octave spanning spectral bandwidth. Therefore, the f-2f-interferometer needs to include a nonlinear broadening stage to allow for spectral overlap between the fundamental and second harmonic spectrum. For the short, low energy pulses from the oscillator a HNF provided by (Menlo Systems GmbH) was used to generate a supercontinuum in one arm of the interferometer while the second harmonic is generated from a 1 mm thick BBO-crystal in the second arm of the interferometer. This device will be referred to as the low-energy f-2f-interferometer.

As described in Sec. 2.7.2, the relative CEP of the input pulses is directly translated to the position of the spectral fringes emerging when the pulses from the SHG- and supercontinuum-arm of the interferometer overlap in time, space and spectrum. The interfering spectra from the two arms are recorded using a fast spectrometer (Avantes AvaSpec-ULS2048CL-EVO) capable of measuring up to $\sim$ 2640 spectra per second. To characterize the stability performance of the seed laser, the relative CEP of the pulses was recorded prior to amplification in the nonlinear regenerative amplifier. The results are displayed in Fig. 3.8 a)-c). The measurement was done with 5 ms integration time, recording 187 spectra/s during a 54 s measurement time, thus each spectrum in the fringe-trace is an average of 500 laser shots. The evolution of the spectral fringe pattern in time, referred to as the fringe-trace is displayed in Fig. 3.8 a). For each time step, the relative CEP between the fundamental- and SHG-arm of the f-2f-interferometer is calculated from the spectral position of the interference

fringes. The retrieved relative CEP is shown in Fig. 3.8 b) demonstrating the good CEP-stability of the oscillator with only 112 mrad rms CEP noise in the detection bandwidth from 0.02 Hz to the Nyquist-frequency of 93 Hz. It has to be noted here that the CEP-stability directly from the oscillator is even better with about 60 mrad rms noise, however, there is already a considerable intensity- and pointing-noise-to-phase coupling in the supercontinuum generation of the f-2f-interferometer due to the approximately 1.5 m of free space propagation from the output of the oscillator, through the grism-compressor to the measurement device. Therefore, the rms noise measured in front of the amplifier is already slightly increased. Fig. 3.8 c) shows a histogram of the retrieved values for the relative CEP.

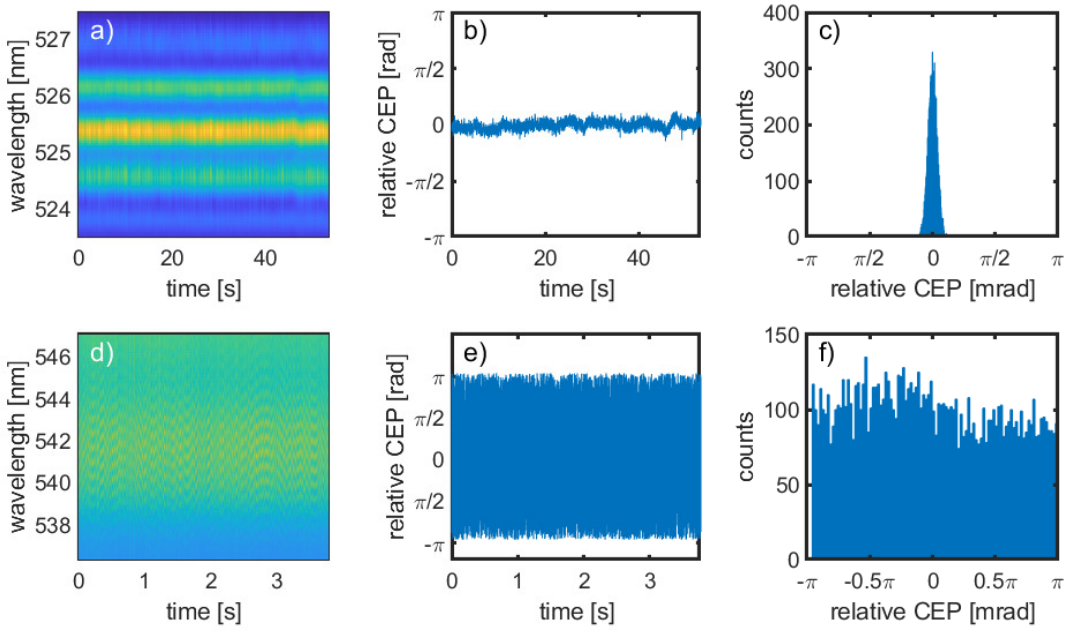

Figure 3.8: Results of the relative CEP measurements of the seed pulses before injection to the nonlinear regenerative amplifier and after amplification to 2 mJ pulse energies. a) and d) show the respective spectral fringe-trace, b) and e) the retrieved relative CEP and c) and f) the histogram of the retrieved CEP values. The data for the seed pulses was recorded using the low-energy f-2f-interferometer with 5 ms integration time and 187 spectra/s. The data for the amplified pulses was recorded using the high-energy f-2f-interferometer with 0.3 ms integration time and 2640 spectra/s.

The CEP-stable pulses from the oscillator are injected into the amplifier cavity. During the 5.36 μs amplification window corresponding to 129 round trips in the amplifiers resonator, the pulses are amplified to 2 mJ energy. The supercontinuum generation in the HNF of the f-2f-interferometer used for recording the relative CEP of the seed pulses is not suitable for high energy pulses with durations of $\gtrsim$ 200 fs. Therefore, a second device relying on bulk filamentation, was built to characterize the output pulses of the nonlinear amplifier after compression. This device is referred to as the high-energy f-2f-interferometer.

A trace of the spectral fringe pattern recorded for the amplified 2 mJ pulses with this second device is displayed in Fig. 3.8 d). With about 2640 spectra/s and 3.8 s measurement time, the recorded data can resolve phase fluctuations in the range from

0.26 Hz to 1320 Hz. It is evident that the amplified pulses do not have a stable CEP, despite the high phase stability of the seed pulses from the oscillator and that the fluctuations are too fast for the detection setup to resolve. The strong phase noise on the amplified pulses becomes even more apparent when directly comparing the relative CEP curves of the seed pulses and the amplified pulses in Fig. 3.8 b) and e), respectively. In fact, the relative CEP of the amplified pulses seems to be completely random which is emphasised by the histogram displayed in Fig. 3.8 d). While the relative CEP of the seed pulses in 3.8 c) shows a high probability to be close to 0, all values in the interval from -π to π seem equally likely for the amplified pulses. Furthermore, the phase difference between two consecutive measurement points is likewise evenly distributed over the full $-\pi$ to π interval, indicating, that whatever mechanism is introducing the additional phase noise happens on time scales below the temporal resolution of the measurement device of the order of ≈ 1 ms.

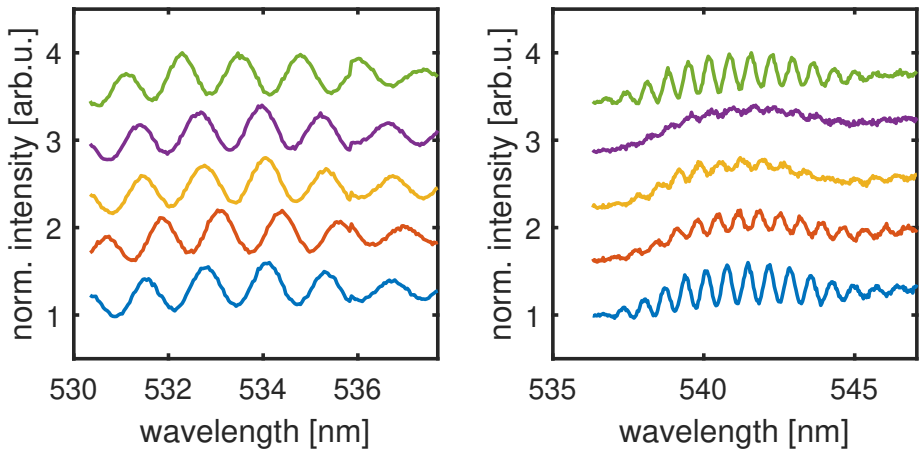

Figure 3.9: a) Five spectra of the interference region of the f-2f-interferometer recorded in consecutive time steps of the fringe-trace shown in Fig. 3.13. For this measurement, the repetition rate of the laser was reduced to 1 kHz allowing for single shot measurements using 1 ms integration time. c) Five spectra of the interference region of the f-2f-interferometer recorded in consecutive time steps of the fringe-trace shown in Fig. 3.8 b). With 0.3 ms integration time, each spectrum is an average of 30 shots.

Due to the speed of the spectrometer, the sampling rate is limited to 2.6 kHz which doesn't allow for shot-to-shot measurements. However, the spectrometer allows for integration times of only 300 μs and thus the measurement of spectra representing the sum of 30 consecutive pulses on average. Comparing spectra recorded at such low integration times reveals strong fluctuations in the contrast of the recorded fringe patterns from one time frame to another indicating that the phase relation between the three pulses forming the spectrum is different for each collected spectrum. This effect becomes apparent when comparing the data displayed in Fig. 3.9 a) and b), showing five fringe-traces recorded consecutively in a single-shot measurement at a reduced amplifier repetition rate of 1 kHz and averaged over 30 shots at 100 kHz repetition rate, respectively. While both measurements show distinct CEP-fringes with random phase jumps from one time step to the next, the overall fringe contrast in the single shot measurement is stable over time. In the measurement averaging over 30 shots, however, the fringe contrast changes from one time step to the next, due to a change in the relative phases of the pulses contributing to the average spectrum.

According to Sec. 2.7.2, this circumstance suggests that the CEP of the amplified pulses is subject to high frequency noise way above the highest resolvable frequency of the f-2f-interferometer and might even by distorted on a shot-to-shot basis. The underlying mechanisms for the phase noise introduced by the nonlinear regenerative amplifier are investigated and evaluated in the following sections of this chapter.

3.4 CEP Distortion Mechanisms in Nonlinear Thin-Disk Amplifiers

The measurements of the CEP in section 3.3 clearly show that the phase of the input pulses gets distorted by the nonlinear regenerative amplifier resulting in a completely random phase after amplification. This indicates, that the nonlinear regenerative amplifier induces a random phase shift $\geq \pm\pi$ on timescales below the resolution of the detection method with its $\sim$ 1000 Hz detection limit. In this section, several possible reasons for these phase distortion are investigated and evaluated to identify the underlying mechanisms and reveal approaches to circumvent the associated phase distortions.

3.4.1 Electro-Optic Phase Distortions

The most obvious possible mechanism to introduce fast CEP fluctuations to the laser beam is the Pockels cell used as optical switch to open and close the resonator of the nonlinear regenerative amplifier. As described in section 3.1, the Pockels cell acts as a variable waveplate, rotating the polarization of a transmitted laser beam by introducing a phase shift between its ordinary and extraordinary polarization components when a high voltage is applied. This effect, however, also leads to a shift of the CEP of the transmitted beam depending on the voltage applied to the Pockels cell. Thus, a large phase noise could be introduced from pulse to pulse if the applied voltage is different for consecutive pulses.

This effect has been observed for the oscillator output when the employed pulse picker was operated in a dual switching mode defined by alternating the induced polarization shift from $+\pi$ to $-\pi$ for consecutive pulses, resulting in a CEP-noise at half the repetition rate. The Pockels cell in the nonlinear regenerative amplifier, however, applies the same voltages for every pulse, resulting in a shift of $-\frac{\lambda}{8}$ when the resonator is open and $\frac{\lambda}{8}$ when it is closed. The CEP of the pulses propagating in the resonator can, however, still suffer from voltage ripple noise caused by the Pockels cell power supply as well as piezoelectric ringing[85]. The effect the switching of the Pockels cell has on the phase can be further investigated by observation of the CEP-fringe-traces of the seed pulses after propagation in the resonator for a small number of round trips. Fig. 3.10 shows the measured fringe-trace (a) and retrieved relative CEP (b) of the seed laser after 3 resonator round trips with no pump light applied. It is evident from the data that the CEP-stability of the seed pulses is not heavily disturbed. While the rms CEP noise increased to 348 mrad, there is no indication that the switching process of the Pockels cell is responsible. In fact, the decrease in phase stability is to be expected considering the loss of pulse energy from accumulated cavity losses as well as the increase in pointing instability and pulsed duration associated

with the additional path length of ≥ 48 m between the source of the laser pulses and the detection setup. As described in section 3.1, the Pockels cell voltage switches only twice during the amplification cycle, once directly after the pulse enters the cavity and once when it is to be released. Therefore, it is not expected that the phase noise introduced by the switching process itself increases accumulative with the amount of round trips. Therefore, it is evident from the results in Fig. 3.10, that the switching process of the Pockels cell is not introducing phase noise of the magnitude observed in the measurements of the amplified pulses.

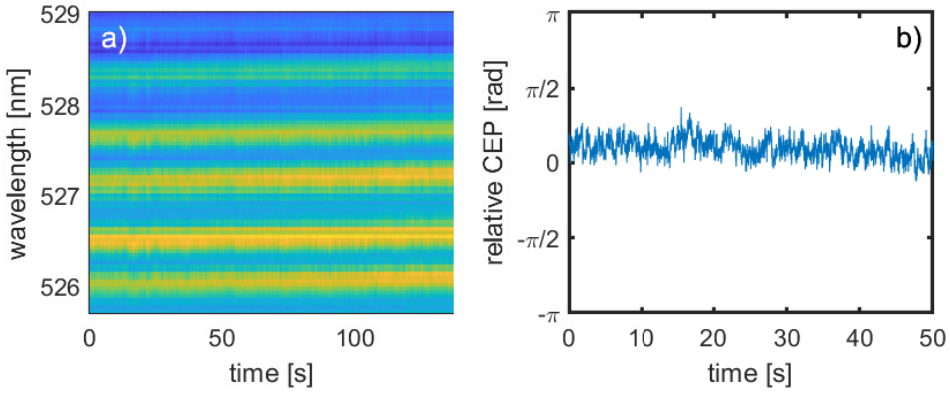

Figure 3.10: CEP measurement of the oscillator pulses after three round trips in the resonator of the nonlinear regenerative amplifier while no pump light was applied. a) shows the recorded fringe-trace and b) shows the retrieved relative CEP for each step in the 137 s measurement time with an rms relative CEP noise of 348 mrad. The integration time on the spectrometer was 5 ms, corresponding to an average of 500 laser shots contributing to each measured spectrum.

Voltage ripple noise on the Pockels cell high voltage driver and piezoelectric ringing could lead to a phase noise which is accumulative with the number of round trips but it is unlikely that these effects contribute significantly to the phase noise as they would also lead to large intensity fluctuations which are not observed in the output pulses of the amplifier with below 1 % pulse-to-pulse energy fluctuations. Additionally, a further increase of the number of round trips of the seed pulses discussed below (Fig. 3.12) shows no indication that the presence of voltage ripples on the Pockels cell voltage supply is responsible for large phase distortions.

3.4.2 Mechanical Vibrations and Path Length Fluctuations

Other mechanisms for introducing additional phase noise are mechanical vibrations and path length fluctuations inside the resonator. As a consequence of the difference between the group- and phase-velocity a CEP-stable train of laser pulses traveling through any kind of dispersive material is subject to a shift of its carrier-envelope phase. Typically, this effect leads to a static shift of the CEP as the main contribution is from propagation in transparent solids of constant thickness. The long propagation distance in the resonator of the nonlinear regenerative amplifier makes the CEP-shift introduced by propagation in air non-negligible. Fluctuations in effective path length inside the resonator can arise from pointing instabilities, thermal drifts and vibrations of the reflective elements in the resonator. However, to have significant

impact on the CEP-noise of the pulse-train, the path length in the medium has to change dramatically. Fig. 3.11 displays the induced shift to the CEP of a short pulse with a center wavelength of 1030 nm over the propagation distance in air, calculated using nonlinear propagation software (Lightwave Explorer) [86].

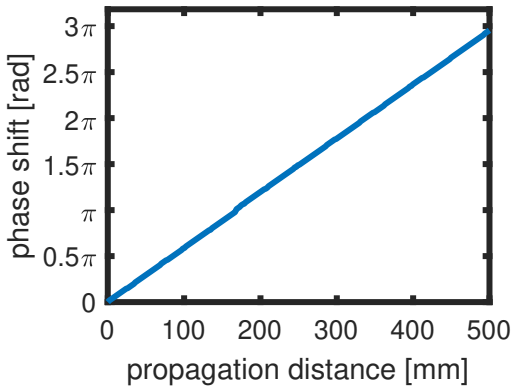

Figure 3.11: Calculated shift in the carrier envelope phase of a laser pulse centered at 1030 nm depending on the propagation distance in air.

Notably, a full 2π-phase shift is induced after 337 mm of propagation in air. To add additional phase noise on the order of $\delta\varphi_{\mathrm{ce}} \approx 100$ mrad, path length fluctuations of $\sim$ 5 mm would be necessary, which is far beyond what a pulse train with moderate pointing stability would experience on propagation distances of a few meters typical to multi-pass amplifiers or beam guiding to experiments. Therefore, this effect is typically negligible. For a regenerative thin-disk amplifier, however, this might not be true. The resonator cavity displayed in 3.3 has a round trip length of $\sim$ 15 m which amounts to a total propagation distance of $>$ 1.9 km over the 129 round trips the pulses take in the cavity. Possible sources for path length fluctuations inside the resonator such as mechanical vibrations or thermal drifts might happen on time scales from hours to few tens of microseconds. Therefore, the phase noise contribution of these effects could be fast enough to exceed the resolution of the f-2f-interferometer for CEP-measurements. However, they are certainly slow enough to be regarded as quasi static during the amplification time window of 5.36 μs for each pulse in the cavity. Thus, the difference in the length of the resonator experienced by subsequent pulses accumulates over the full number of round trips. Therefore, path length fluctuations of only $\sim$ 40 μm per round trip would be sufficient to induce an additional 100 mrad phase noise contribution. This result is already closer to realistic values for length changes due to thermalization processes. However, it is still unlikely that the resonator length fluctuates by $\pm$ 40 μm on time scales below the temporal resolution of the CEP-measurements, let alone between a few shots of the 100 kHz laser system. Additionally, the CEP-stability of the seed-pulses was measured after the pulses where kept inside the resonator for various amounts of round trips. It is evident from the results displayed in Fig. 3.12 a) that the CEP-stability exhibits only a weak dependence on the number of cavity round trips. The observed decrease in CEP-stability is mainly caused by the increasing pulse duration and decreasing pulse energy rather than actual CEP-noise. This leads to more and more unfavorable conditions for the

supercontinuum generation in the measurement device. Thus the observed noise increase is caused by an enhancement of the detection noise.

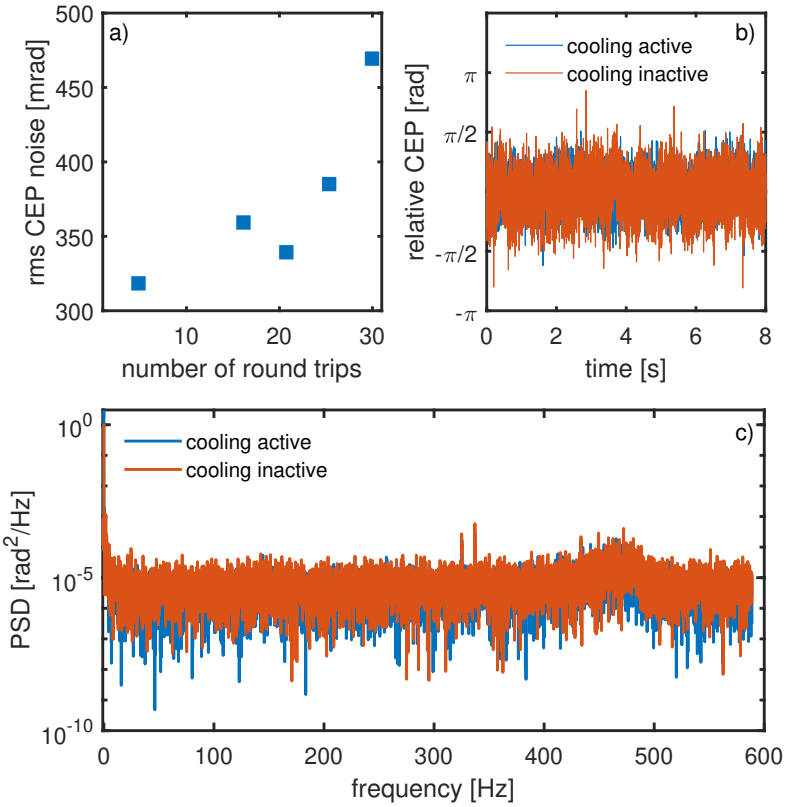

Figure 3.12: a) Observed rms CEP-noise of the seed pulses depending on the number round trips the pulses were kept in the resonator of the nonlinear regenerative amplifier before the measurement. Each data point is derived from a 13.4 s long CEP-measurement recording 741 spectra/s at an integration time of 1 ms. b) Relative carrier-envelope-phase observed for the seed pulses after 3 resonator round trips with active and inactive water cooling of the thin disk, respectively. During an 8 s time interval, 1180 spectra/s were recorded with an integration time of 0.5 ms. c) Power spectral density of the CEP noise calculated from the measurements displayed in b).

To further investigate the effect of mechanical vibrations, the relative CEP of the seed laser was measured after 3 round trips in the cavity both with and without water cooling of the thin-disk and resonator chamber active. For each of these measurements, 10000 spectra were recorded at an integration time of 0.5 ms. If mechanical vibrations have a major contribution to the phase distortion, deactivating the water cooling as the main source of vibrations in the setup should have a notable effect on the observed CEP-stability. Fig. 3.12 b) shows the retrieved relative CEP for the two measurements showing equivalent amounts of CEP fluctuations for both measurements. In fact, the rms CEP noise with the water cooling activated amounting to 420 mrad is slightly below the 513 mrad phase noise observed for the reference measurement with the water cooling deactivated. Fig. 3.12 c) shows the power spectral densities calculated from the CEP measurements for both cases allowing for a frequency resolved analysis of the CEP noise. However, there doesn't seem to be a noise contribution at a specific

frequency in the 0.1-590 Hz detection range of the measurement which is exclusive to the measurement with activated water cooling and thus could be attributed to the induced mechanical vibrations.

To achieve a better understanding of how and when the CEP-phase stability is lost during the amplification process, it would be desirable to observe the CEP-stability for each number of round trips and various amplification levels from the unpumped seed laser to the full 2 mJ output beam. However, this is not possible due to the limitations of the used f-2f-interferometers which requires a stable supercontinuum generation. Additional insight into the matter can be achieved by investigating the results from measurements of the seed and amplified pulses at the detection limits of the low-energy and high energy f-2f-interferometer, respectively. These limits are determined by the pulse conditions required to allow stable supercontinuum generation in the respective device.

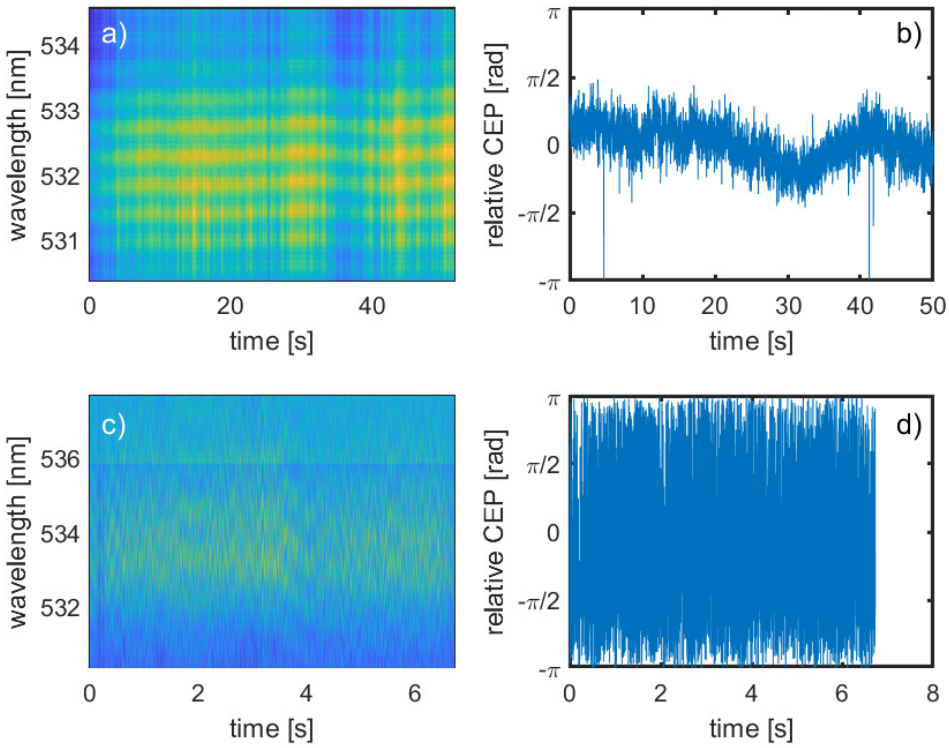

Figure 3.13: a) and b) show the measured CEP-fringe-trace and the retrieved relative CEP of the seed pulses after 30 resonator round trips. 78 W of pump light were applied to the disk. The spectral fringes were recorded for 137 s using the low-energy f-2f-interferometer. The integration time was set to 10 ms. The rms CEP noise of the measurement amounts to 488 mrad. c) and d) show the CEP-fringe-trace and the retrieved relative CEP of the amplified pulses after 33 resonator round trips with $\sim$ 400 W of pump power applied to the disk recorded for 13.5 s using the high-energy f-2f-interferometer. The integration time was set to 1 ms. For this measurement, the repetition rate of the amplifier was reduced to 1 kHz, the data therefore represents a single-shot measurement. The recorded data has a random CEP for each recorded pulse.

Fig. 3.13 a) and b) show the fringe-trace and relative CEP of the seed pulses under conditions as close as possible to the regular operation conditions of the amplifier.

Using the low energy f-2f-interferometer, a stable CEP fringe-trace can be observed after 30 round trips while 78 W of 969 nm pump light is applied to the thin-disk. The rms CEP noise of the measurement amounts to 488 mrad. Beyond 30 round trips, the increase in pulse duration and the decrease in pulse energy prevent the generation of a stable supercontinuum and thus the observation of the spectral fringes which encode the information on the relative CEP. At pump powers exceeding 78 W the amplification and associated gain narrowing increased and likewise made the generation of a stable supercontinuum impossible. However, while the rms noise increases from 112 mrad at the oscillator output (see fig 3.8a)-c)) to 469 mrad after 30 round trips in the resonator, the data displayed in Fig. 3.13 a) and b) shows that the CEP-stability of the seed pulses is preserved for many round trips. Even at the edge of the detection capabilities of the measurement device, where instabilities in the supercontinuum generation impose additional noise to the measurements, a stable relative CEP of the pulses can be observed.

The high energy f-2f-interferometer is capable of generating a stable supercontinuum even for pulses with picosecond durations, but needs sufficient pulse energy to enable filamentation in the YAG crystal. Amplification to energies which enable operation of the high energy f-2f-interferometer was possible for a minimum of 33 round trips at a pump power of $P_{pump} \approx 400$ W. The recorded spectral fringe-trace and retrieved relative CEP are shown in Fig. 3.13 e) and f), respectively. Despite the low number of round trips, a stable CEP cannot be observed. It has to be noted here, that the repetition rate of the amplifier was decreased to 1 kHz for the measurement displayed here to allow for single-shot measurements using an integration time of 1 ms at the spectrometer.

Despite the similar amount of round trips in the measurements shown in Fig. 3.13 c)-d) and e)-f), the CEP-behaviour observable for the seed and amplified pulses is vastly different which suggests that the main contribution of the observed phase distortion is introduced during the amplification process, caused either by nonlinear or thermal effects rather than vibrations or path length fluctuations. By investigating the CEP-behaviour of the seed and amplified pulses under different conditions, mechanical vibrations, path length fluctuations, the switching process of the Pockels-cell and piezo-electric ringing could be excluded as main contributions to the observed phase distortions. However, the limitations of the f-2f-interferometers for CEP-measurements prevent a systematic analysis of the noise contributions of these effects during the amplification process. Therefore, other tools must be used to investigate the process underlying the observed phase noise.

3.4.3 Intra-Cavity Air Turbulences

The nonlinear regenerative amplifier is built inside a vacuum chamber to prevent a disturbance of the stable laser operation by turbulent air currents generated by the inevitable air flow present in the laboratory. However, the chamber is not evacuated since a low air pressure would lead to a significant reduction in nonlinear broadening and a drastically increased probability of voltage flashovers at the employed Pockels cell switch which would eventually render the cell unserviceable [79]. As described in section 3.3, the chamber is instead filled with dry air to reduce the influence of the inevitable changes of the environmental air humidity on the laser performance

as far as possible. Operating the amplifier now induces heat sources to the confined environment of the resonator chamber leading to an increased air temperature and the emergence of convectional air flows. Especially in the space between the Yb:YAG-disk and the pump light optics a turbulent air current can emerge due to the high thermal load on the disk. Those air currents result in a refractive index profile experienced by the pulses during amplification which is varying in time and space. The disturbance of the homogeneity in the refractive index of the gas leads to a partial diffraction of the pulses which can be utilized in techniques like Schlieren imaging which is described below. Additionally, a non static refractive index results in an effective change of the path length experienced by pulses propagating through the medium leading to a time dependant phase shift. Even a small change in phase at some point in the beam path would have a noticeable effect on the CEP of the output pulses as the total phase shift is accumulated over the $\sim$ 260 passes through the turbulent air space during the resonators amplification time window.

To investigate the strength and frequency of the phase noise induced by turbulent air currents in front of the thin disk of a high power regenerative amplifier a simple interferometer was implemented into the cavity as shown in Fig. 3.14. Building the interferometer directly into an operational amplifier is necessary as it is crucial to conduct the measurements of the phase fluctuations induced by turbulent air currents in front of a strongly pumped and therefore hot Yb:YAG-disk. Applying a strong pump beam to the disk without a laser beam extracting the energy stored in the active medium, however, would lead to damages to the disk, the pump optics or even the pump diodes themselves. Due to spatial constraints, the measurements in this section were not performed in the resonator of the nonlinear regenerative amplifier but in the resonator of another high power thin-disk amplifier. The effect of air turbulences in front of a strongly pumped disk should, however, be universal to the thin disk concept.

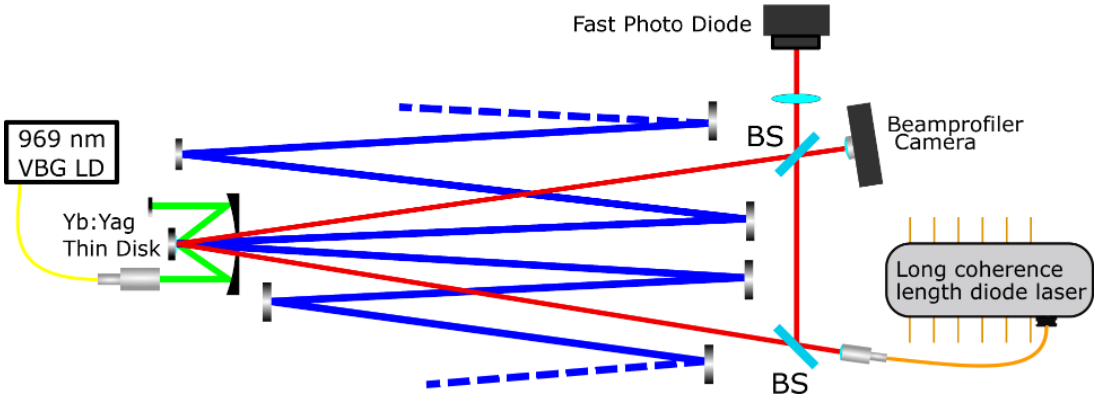

Figure 3.14: Schematic drawing of the interferometer setup used for recording phase fluctuations induced by thermally induced air turbulences in front of the disk. BS refers to a 50/50-beamsplitter for the 1064 nm output of the long coherence length photo diode, splitting and recombining the two arms of the interferometer, respectively. Depicted in red is the 1064 nm beam probing the phase fluctuations. Depicted in blue is a part of the beam path of the 1030 nm pulses which are amplified in the resonator.

The interferometer consists of a continuous wave laser diode with a coherence length of > 1 km and a wavelength of 1064 nm. Since the amplification bandwidth of the Yb:YAG is only ~ 9 nm, the 1064 nm beam from the laser diode can pass over

the disk without experiencing significant amplification while still being close enough in wavelength to experience similar refraction in the gas. The laser beam is divided into two arms by a 50/50-beamsplitter. One arm is guided over the thin disk and subsequently recombined with the second arm of the interferometer by another 50/50-beamsplitter. A beam profiler camera in one output channel of the recombination beamsplitter is used to observe the resulting interference and ensure proper beam alignment. The beams in the second output channel of the beamsplitter are focused onto a fast photo diode with a rise time of ~ 120 ps, which is protected from stray light of the amplifier by a 1064 nm bandpass filter. The signal detected on this photo diode is directly proportional to the phase difference between the two arms of the interferometer. Assuming a 50/50 splitting ratio, the intensity in the corresponding output channel of the beamsplitter, is given by

$$I_{out} = \frac{I_1 + I_2}{2} + \frac{\sqrt{I_1^2 + I_2^2}}{2} \cdot \cos(\Delta\phi) \tag{3.1}$$

where I_1 and I_2 are the respective intensities of the interfering input beams and $\Delta\phi = \phi_1 - \phi_2$ is their difference in phase. If there is a strong, time dependent phase distortion due to turbulent air currents in front of the disk, the photo diode will observe intensity fluctuations according to equation 3.1 as the phase of only one of the input laser beams is modulated by the distortion. Thus the phase noise introduced by the turbulent air currents is transferred to an intensity noise signal which is recorded using a fast USB oscilloscope (Pico Technology Ltd PicoScope). To characterize different contributions to the phase noise, the intensity fluctuations on the photo diode were measured in different configurations summarized in table 3.1.

Configuration	water cooling	P_{out} [W]	t_{obs} [s]	n	rms noise [mrad]
I	active	758	30	5e6	213
II	active	0	30	5e6	167
III	inactive	0	30	5e6	87

Table 3.1: Overview of the different operation states of the amplifier during the phase noise measurement using the interferometer setup shown in Fig. 3.14. The table also displays the total rms phase noise observed in the respective operation state in a time resolved measurement using an oscilloscope.

To compare the phase noise between the two arms of the interferometer, the power spectral density (PSD) of the intensity noise was calculated from the recorded time domain data for the configurations in table 3.1 and is displayed in Fig. 3.15.

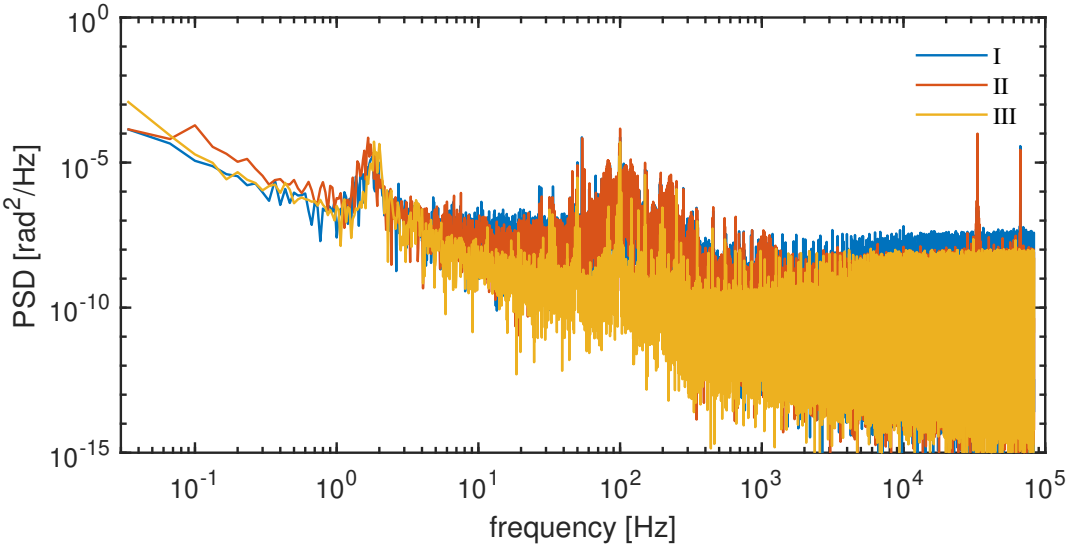

Figure 3.15: Recorded direct cw-laser phase measurements using the interferometer setup shown in Fig. 3.14 in a time resolved measurement using a USB oscilloscope (Pico Technology Ltd PicoScope) for inactive, and active water cooling of the thin disk as well as during amplifier operation with 758 W of pump power applied to the disk.

Several features can be identified in the power spectral density of these phase measurements. The most prominent is the pronounced increase in noise at frequencies between 50 Hz and 120 Hz which emerges when the water cooling for the disk is activated. In the reference measurement (III) without active water cooling, this noise feature is absent. Likewise, there are two peaks in the power spectral density a 33 kHz and 67 kHz which are exclusive to the two measurements with the disk cooling active. However, the vibrations caused by the water cooling of the disk and the chiller have already been excluded as main contribution to the phase distortions in section 3.4 and there are no prominent features showing up only in the measurements in configuration (I) where the disk is illuminated by 758 W of pump light. Fig. 3.15 in fact reveals that the main difference to the unpumped measurement (II) is a slight increase of the white noise between 10 kHz and 100 kHz. Interestingly, the noise feature at 50 Hz-120 Hz visible in configuration I and II does not show up in the CEP-measurements of the seed laser in Fig. 3.12 c) despite being within the detection bandwidth of the CEP measurement. This might be due to the larger dimensions of the disk implemented into the resonator used for the interferometric phase measurements with the cw-diode laser leading to lower resonance frequencies. Thus, the noise features observed in the CEP-measurements with the smaller disk size would show up at higher frequencies. The total amount of phase fluctuations over the full observable frequency range was calculated by integrating the PSD and amounts to 213 mrad, 167 mrad and 87 mrad for the measurement configurations I, II and III, respectively. To evaluate the background noise of the measurement, two additional measurements of the intensity noise on the disk were taken with the disk arm and reference arm of the interferometer blocked, respectively. From these measurements the background detection noise due to pointing and intensity fluctuations of the diode laser can be calculated to be $\lesssim 50$ mrad. The increase in phase noise observed when a strong pump beam is applied could indicate that air turbulences contribute to

the phase distortions observed in the CEP of the amplified pulses. However, the data displayed in Fig. 3.15 suggests that the noise introduced by thermally induced distortions of the air in front of the disk is smaller than the contribution of mechanical vibrations of the disk which have already been excluded as main contribution to the phase distortion in the previous section.

Another way to observe the effect of air turbulences in front of the disk is to directly visualize them using Schlieren photography.

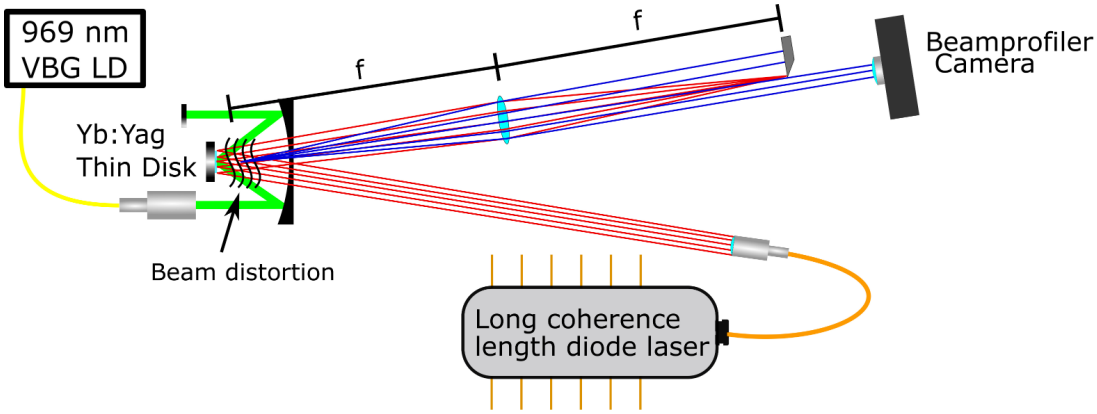

Figure 3.16: Setup used for recording Schlieren images of the air currents in front of the disk.

The Schlieren imaging setup shown in Fig. 3.16 is based on the same long coherence length 1064 nm cw-diode laser used for the interferometric phase measurements. In this case, however, the beam is not split into the arms of an interferometer but directly guided over the disk. A 200 mm lens is used to focus the beam after reflection on the disk. The distance between the lens and the disk is chosen to be slightly larger than the focal distance to allow imaging of the plane directly in front of the disk to the beam profiler camera. In the focus of the beam, a knife edge is inserted, blocking a large portion of the undisturbed beam. If the 1064 nm beam is diffracted by air turbulences in front of the disk the different propagation of the diffracted beam afterwards leads to an increased intensity transmitted past the knife edge. Thus the camera is observing an image of the refractive index profile responsible for the diffraction of the beam. The functionality of the setup was verified by imaging the gas jet from a $\sim$ 1 mm diameter nozzle attached to a spray can used for cleaning optics. The resulting image is shown in Fig. 3.17 a). The image is slightly blurry due to the fact that the nozzle cannot be inserted into the imaging plane in front of the disk. Still the jet exiting the nozzle is clearly visible in the image.

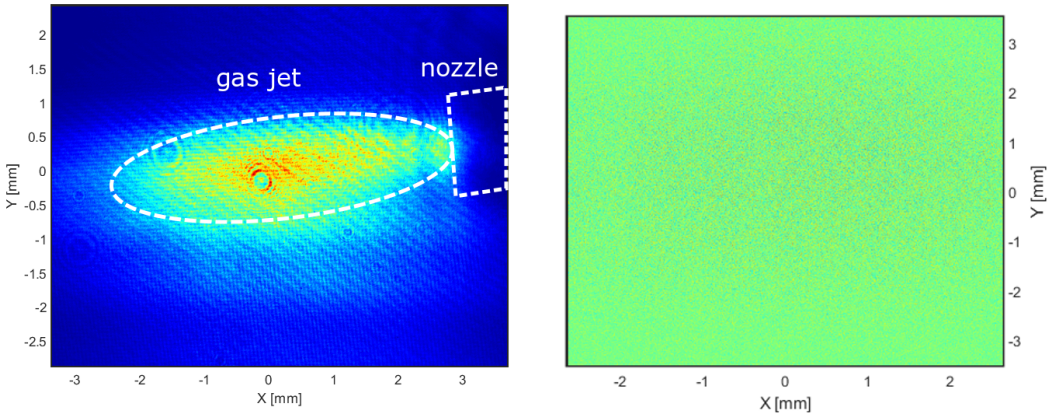

Figure 3.17: a) Schlieren image of the gas jet emitted from a $\sim$ 1 mm nozzle. b) Schlieren-image of the air turbulences in front of the Yb:YAG-thin-disk. The image shows one of the 53 images taken with the first image subtracted to eliminate static background. Only electronic noise and residual background is visible in the image and no air turbulences can be resolved in the Schlieren-image.

To characterize the air turbulences induced by the thermal load on the disk during the amplification process, a series of 53 images was taken within about 30 s. The resonator was operated with 758 W of pump light illuminating the disk during this measurement. This allows for an observation of time varying, temperature induced refractive index changes in front of the disk. However, the recorded Schlieren images do not show any signal evolving in time beyond the electronic noise of the camera. This suggests that the air turbulences in front of the disk are not disruptive enough to be observed using the Schlieren photography.

3.4.4 Nonlinear Phase Noise

The last possible source of additional phase noise investigated in this work is the nonlinear nature of the amplifier itself. As the light pulses get amplified and the pulse energy inside the cavity rises, the pulses start inducing a nonlinear response in the 20 mm BBO of the Pockels cell and the air inside the resonator. The result is an augmentation of the refractive index $n = n_0 + n_2$ as described in section 2.5.1. This nonlinear response is a crucial part of the nonlinear regenerative amplifier concept. It allows for a reduction of the compressed duration of the amplified pulses by spectral broadening due to intra-cavity SPM. However, since the nonlinear response manifest itself in an intensity dependent refractive index of the medium, there is also an intensity dependent phase shift associated to it. If the seed pulse energy, single pass gain and cavity losses were to be identical for every pulse within the laser pulse train, this phase shift would not lead to an increased CEP-noise as all pulses would experience the same phase shift. However, a real laser system is always subject to fluctuations leading to slightly different conditions from pulse to pulse, and thus to a different amplification behaviour. This different behaviour can be expressed by the B-integral the pulses accumulate during the amplification process. Especially when the amplifier is operated in a saturated regime, where changes in the seed energy or the number of round trips have little effect on the final energy of the amplified pulses, consecutive pulses might accumulate vastly different B-integrals without showing obvious devia-

tions in pulse energy. I note here, that the major contribution to the B-integral of the pulses is from the last couple of round trips where the pulse energy is already high enough to induce a significant nonlinear response of the media inside the cavity. Therefore, reaching the 2 mJ pulse energy on an earlier or later round trip immediately leads to a large change in the total B-integral. This could easily be caused by a change in cavity losses, single pass gain or seed pulse energy. The CEP-noise induced by this effect, however, cannot be investigated experimentally since there is no way to reliably measure the CEP during the built up in the cavity or the total B-integral of the output pulses. Thus, the effect is investigated theoretically by simulating the propagation of the pulses using the Lightwave Explorer nonlinear propagation software developed by Nicholas Karpowicz [86]. The change in the nonlinear phase Φ_{NL} the pulses accumulate during the amplification process and the output pulse energy were extracted from the results. While this nonlinear phase is not equivalent to the CEP of the pulses, a change in the nonlinear phase accumulated during amplification is directly related to a proportional shift in the carrier-envelope-phase. To make the simulations less expensive, the medium inside the resonator is treated as vacuum and the nonlinearity is confined to the BBO of the Pockels cell. The beam size and the length of the Pockels cell have been adjusted for the simulations to reproduce the output spectrum shown in Fig. 3.5 for the cavity layout illustrated in Fig. 3.3. The saturation of the amplifier is represented in the simulations by a finite energy stored in the thin disk augmenting the single-pass gain upon depletion.

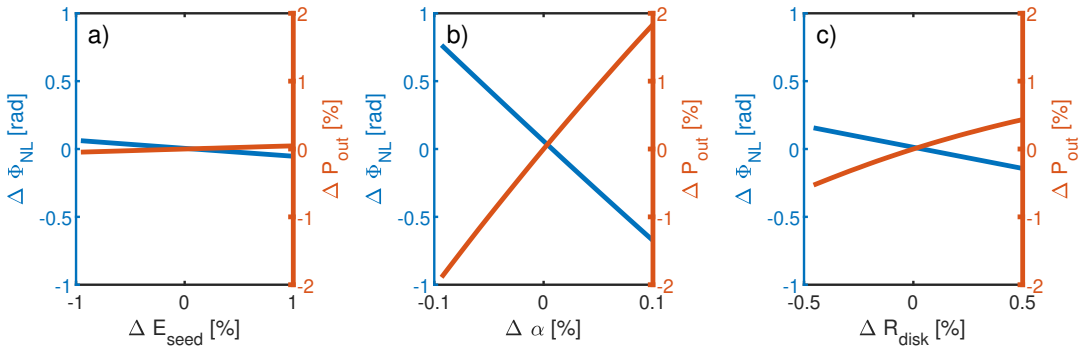

Figure 3.18: Simulated change in the nonlinear phase $\Delta\Phi_{NL}$ the pulses accumulate during amplification to 2 mJ pulse energy in the nonlinear regenerative amplifier (blue) and percental change in output power (red) depending on a change in seed pulse energy (ΔE_{seed}) a), cavity losses ($\Delta\alpha$) b) and radius of curvature of the thin disk (ΔR_{disk}) c).

Fig. 3.18 shows the results of simulations of the pulse propagation inside the cavity depending on the seed energy (a), the amount of cavity losses (b) and the curvature of the disk (c). The relative change in nonlinear phase $\Delta\Phi$ is depicted in red while the relative percental change in output power P_{out} is depicted in blue. To allow for an easier comparison, all graphs use equal y-axis-scales. It is evident from the results, that the impact on the nonlinear phase and output power depends heavily on the parameter which is varied. As expected, changing the seed power in a $\pm$ 1%-interval only leads to a small change output power due to the saturated nature of the amplifier. Interestingly, the change in nonlinear phase amounts to only approx. 260 mrad in the

investigated seed pulse energy interval. Since the pulse-to-pulse energy fluctuations of the seed laser have been measured to be $\leq 1\%$ it is unlikely that seed fluctuations cause major nonlinear distortions to the CEP, however, Fig. 3.18 shows that other parameters have a much larger influence on the accumulated nonlinear phase of the amplified pulses. Especially the magnitude of the intra cavity losses (Fig. 3.18 b)) have a large impact on the nonlinear phase. A small change of the loss per round trip of only 0.1 % results in a change in nonlinear phase of $\Delta\Phi = 765$mrad. Due to the saturation of the amplifier, however, a change in the cavity losses per round trip doesn't result in large changes in the achievable output power. A scan of single round trip gain leads to equivalent results.

The nonlinear phase noise also offers an additional avenue for mechanical vibrations and thermal air turbulences to couple to the phase noise, as they are the main source for pointing and thus changes of the intra cavity losses. Vibrations of the disk due to the backside water cooling might also lead to small fluctuations of the curvature of the disk and therefore of the beam diameter in the cavity. The beam size fluctuation could couple to the CEP-noise of the amplified pulses while leaving the low-energy seed pulses undisturbed due to nonlinear propagation effects. This effect is investigated by simulating the amplification of the pulses in the cavity for different radii of curvature for the disk. The results shown in Fig. 3.18 c) suggest that while this effect leads to a change in nonlinear phase, the impact on the output power is much higher, making it unlikely that this effect has a major contribution to the phase distortions as the pulse-to-pulse energy noise of the output pulses was measured to be approximately 1 %.

3.5 Summary and Conclusion

The purpose of this laser development project was to explore the feasibility to generate a high power CEP-stable pump beam by direct amplification of CEP-stable seed pulses in a nonlinear regenerative Yb:YAG-thin-disk amplifier. With an achievable pulse duration < 200 fs and multi-mJ pulse energies directly from the amplifier, such laser systems provide excellent preconditions for further nonlinear compression to the few-cycle regime while avoiding the need for large and costly grating based stretchers and compressors, which introduce losses and provide an additional source of CEP-noise. Thus, a nonlinear regenerative amplifier delivering CEP-stable multi-mJ pulses would be highly interesting for driving various experiments in attosecond spectroscopy and strong field physics.

In the scope of this thesis, a nonlinear regenerative amplifier was built, based on the work of Moritz Ueffing [79, 81]. Seeded by a CEP-stable fiber oscillator, this amplifier achieved an output power of up to 210 W at 100 kHz repetition rate and compressed pulse durations of $\tau \approx 190$ fs. The CEP-stability of the amplified pulses was characterized using an f-2f-interferometer including a YAG-crystal for supercontinuum generation. This is necessary to achieve spectral overlap between the fundamental and second harmonic components of the beam. A thorough investigation revealed, that the CEP of the amplified pulses is subject to strong distortions during the amplification process resulting in a completely random phase relation between the carrier and the envelope post amplification. Several possible explanations for the strong distortions to the CEP have been investigated experimentally and the-

oretically, evaluating the contribution of the respective distortion mechanisms to the overall phase noise observed in the experiment.

The conclusion drawn from this investigation is that the main contribution is likely to be the nonlinear phase noise investigated in section 3.4.4. This phase noise results from a slightly different pulse built-up behaviour in the cavity due to fluctuations in the seed energy, cavity losses or gain which leads to different total amounts of nonlinear phase accumulated during amplification. A real laser system will always be subject to these fluctuations to some extent. This suggests that CEP-stability cannot be easily achieved using an amplifier design relying on intra-cavity nonlinear broadening. Therefore, realizing a CEP-stable regenerative thin-disk amplifier might only be possible using a CPA-based approach at cost of giving up the more compact and cost efficient design and more straightforward compression of the nonlinear approach. However, the CEP-stability would still suffer from the $\sim$ 1 km propagation distance and the turbulent air currents inside the cavity of the resonator. Thus, other means of generating high power multi-mJ, CEP-stable pulses could be preferable. Considering near infrared (NIR)-sources, a similar performance compared to a CPA-based Yb:YAG-thin-disk regenerative amplifier in terms of pulse energy, repetition rate and pulse duration can be achieved using an Innoslab amplifier. Seeded by CEP-stable pulses, the multi-pass amplification in an Innoslab amplifier could avoid the additional phase noise introduced by km-scale propagation distances and accumulative phase noise from air turbulences. This could allow for a better stability performance of the amplified pulses.

Chapter 4

A High Power CEP-stable SWIR OPCPA Setup

The content of this chapter has partially been published in [87].

While direct amplification of CEP-stable pulses in a regenerative thin-disk amplifier is desirable due to the high pulse energies and average powers achievable, it suffers from the phase distortion effects discussed in the previous chapter. However, high power Yb:YAG-thin-disk amplifiers make outstanding pump sources for OPCPA-setups. Therefore, these laser systems can still be useful for generating CEP-stable, few-cycle, high-energy pulses at high repetition rates. As pump-to-signal conversion efficiency in broadband SWIR OPAs typically is limited to $< 20\,\%$, this approach results in lower achievable average powers and pulse energies compared to the direct output of an Yb:YAG-amplifier [88]. However, OPCPA setups also have a number of distinct advantages over the direct use of the Yb:YAG output pulses especially for the use in attosecond experiments, which make up for the reduced average power. OPCPA setups driven by the 1030 nm pump light from an Yb:YAG-amplifier can achieve high amplification bandwidths allowing for few-cycle pulses especially at the degeneracy point where the amplified signal is centered at twice the pump wavelength [66]. Therefore, OPCPA setups can avoid the necessity for nonlinear post-compression for many applications. Furthermore, the longer wavelength of the OPCPA output helps to push the HHG-photon energies further into the SXR-regime due to the λ^2-scaling of the HHG-cutoff energies and enable efficient photon generation in the water window [89]. Finally, passively CEP-stable SWIR-seed pulses can be generated directly from the pump light by nonlinear frequency conversion involving a DFG process [41, p.106].

In this chapter a high pulse energy, 10 kHz repetition rate SWIR-OPCPA-source, based on a kW-class Yb:YAG pump laser driving a passively CEP stable SWIR seed generation and the subsequent amplification in three broadband degenerate OPA stages is demonstrated. Reaching up to 51 W of average power, this laser system is to the best of the author's knowledge, the highest average power SWIR-OPCPA source which delivers CEP-stable few-cycle pulses. Furthermore, it delivers the highest SWIR pulse energies available at repetition rates above 1 kHz. The resulting high energy pulses with a center wavelength of 2.1 μm are compressible to below 20 fs. Due to the passively CEP-stable seed pulse generation and an active slow-loop CEP control, the CEP of the pulses can be stabilized with a precision of < 100 mrad. Together with the excellent power stability resulting in only 0.8 % rms average power fluctua-

tions, this laser system constitutes a new back-bone of ultrafast science. To classify the performance of the OPCPA setup, Fig. 4.1 shows the achievable peak power depending on the repetition rate of current state-of-the-art SWIR-OPCPA sources.

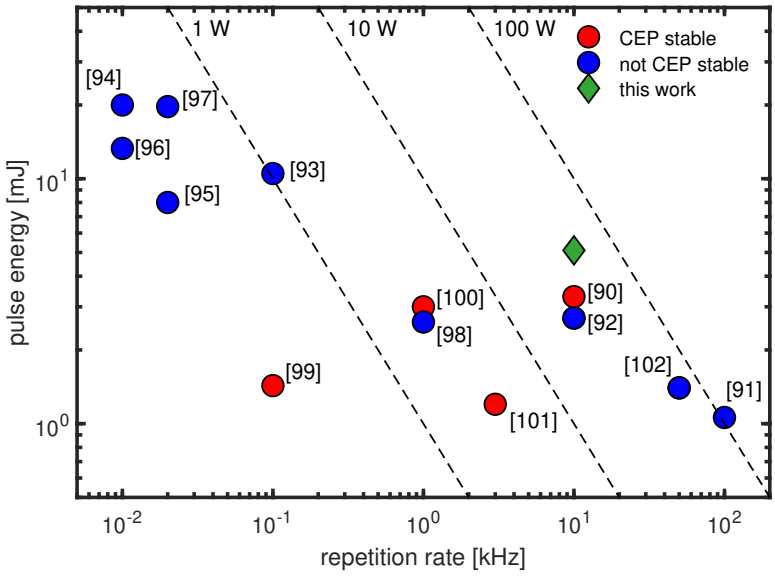

Figure 4.1: Overview of high pulse energy SWIR and mid infrared (MIR) OPCPA setups. CEP stable systems are displayed in red. Sources without CEP stability are shown in blue. The dashed lines mark lines of constant average power.

This chapter describes the general layout and output performance of the pump light source in Sec. 4.1 before describing the general layout of the OPCPA-setup in Sec. 4.2. The output performance, design criteria, and challenges for the CEP-stable seed generation (Sec. 4.3), broadband amplification (Sec. 4.4), few-cycle pulse compression (Sec. 4.5) and CEP-stabilization (Sec. 4.6) are discussed. The results are summarized and evaluated in Sec. 4.7.

4.1 The Pump Source

For driving the high energy OPCPA-setup a high-power light source is required which delivers pulses with tens to hundreds of mJ energy at repetition rates exceeding the kHz-level. This makes CPA-based high power Yb:YAG thin-disk regenerative amplifiers an optimal choice. The laser built as a pump source for the OPCPA-setup discussed in this chapter is very similar to the laser system demonstrated by T.Nubbemeyer et al. [103], which is thoroughly described in [104]. Therefore, this section only gives a brief overview of the setup and the relevant output parameters of the pump light source used to drive the OPCPA-setup. A schematic drawing of the pump laser setup is shown in Fig. 4.2.

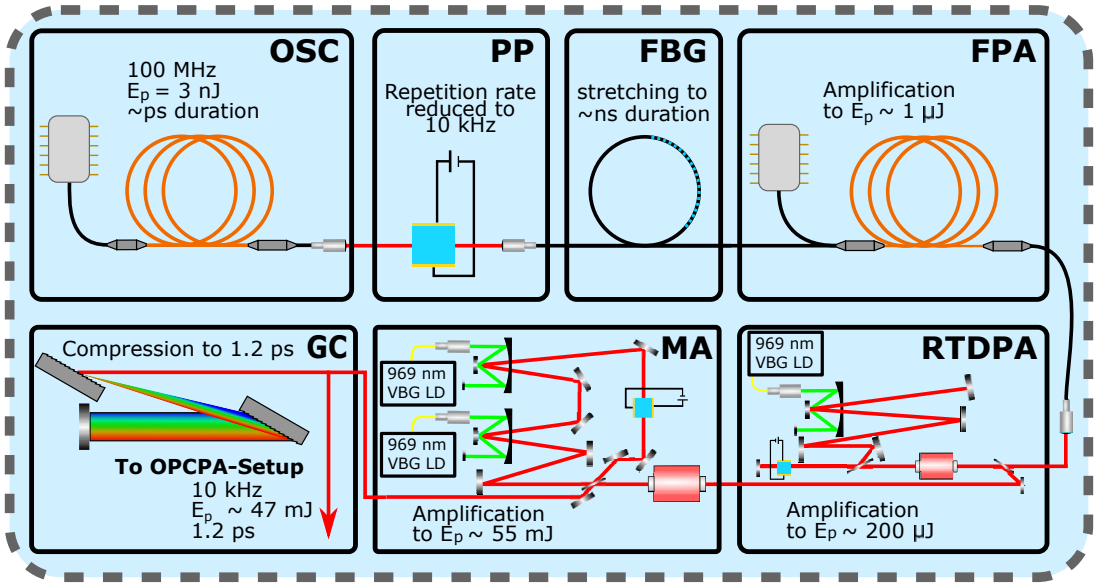

Figure 4.2: Overview of the high power Yb:YAG-amplifier chain used as a pump laser for the OPCPA setup. The individual segments displayed here do not show the actual setup of the respective parts of the laser but only a general representation of the respective unit. OSC: oscillator, PP: pulse picker, FBG: fiber-Bragg-grating, FPA: fiber pre-amplifier, RTDPA: regenerative thin-disk pre-amplifier, MA: main power-amplifier, GC: grating compressor. Beams traveling in free-space are displayed in red, fiber components are displayed in black (plain waveguide) or orange (laser active fibers).

The pump laser chain is based on an Yb:YAG-fiber oscillator (EKSPLA LightWire FFS) operating at 50 MHz repetition rate. A commercial Pockels-cell pulse picker (Bergmann Messgeräte Entwicklung KG) including a 4 mm x 4 mm X-Cut RTP crystal is used to reduce the repetition rate to 10 kHz. The pulses are then stretched to ns pulse durations in a fiber-Bragg-grating (FBG) (Teraxion). The low efficiency of the FBG necessitates the implementation of a Yb:YAG-fiber pre-amplifier provided by (Thorlabs Inc.) to boost the pulse energy between the FBG and the two Yb:YAG thin-disk amplifiers. The thin-disk pre-amplifier is a home-built linear, single thin-disk regenerative amplifier which amplifies the pulse energy of the seed pulses to ~ 2 mJ. While only a 200 μJ fraction of the pulse energy is used to seed the main power amplifier, it is necessary to operate the pre-amplifier at a higher power level to to guarantee stable output conditions. The pulses split from the pre-amplifier output are then directly seeded into the circular resonator of the home-built double-Yb:YAG-thin-disk main power amplifier.

The main power-amplifier is capable of delivering more than 550 W of average power at 10 kHz repetition rate. The 1030 nm wavelength pulses from this pump source are compressed to 1.2 ps duration in a grating compressor with 85 % throughput efficiency, providing up to 470 W of power in the compressed beam. While being a high power laser source, the Yb:YAG thin-disk amplifier still exhibits an excellent power stability and beam quality with only 0.3 % rms average power fluctuations over multiple hours of operation and an M^2 of 1.1 in both Y- and X-direction.

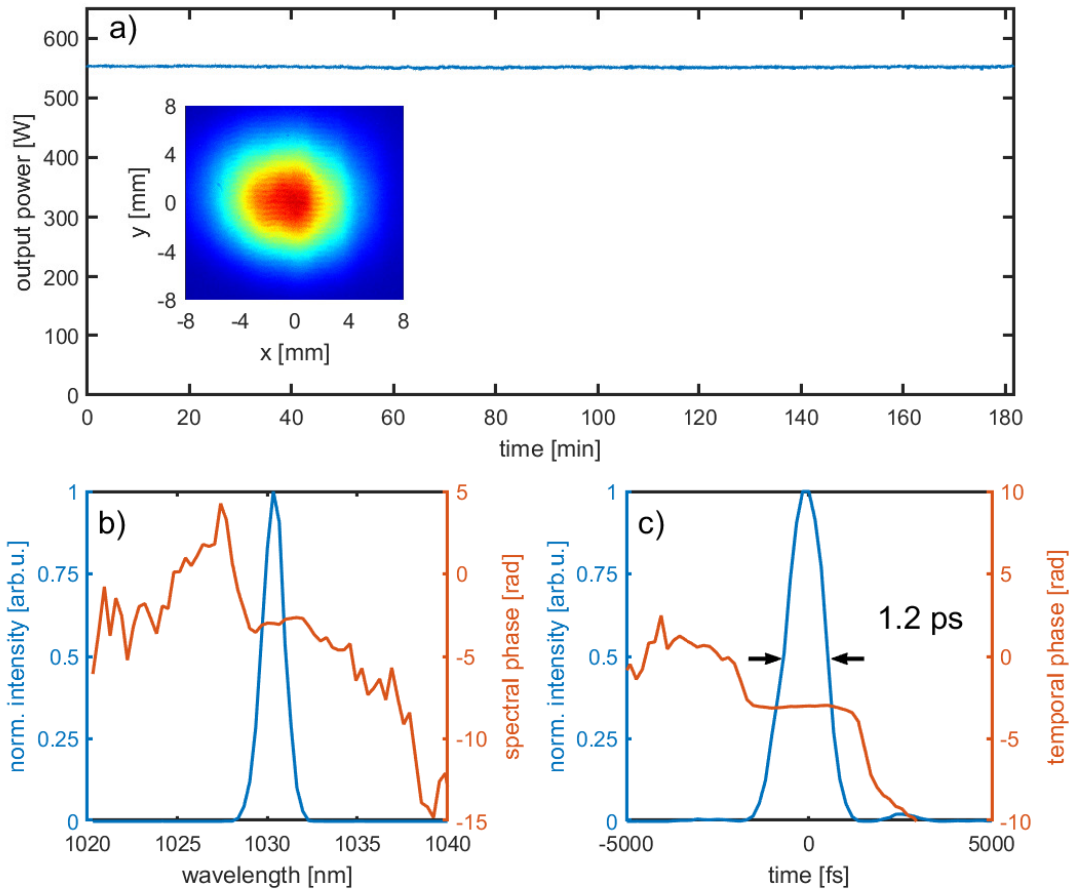

Figure 4.3: a) Output power of the regenerative thin-disk power amplifier measured over more than 140 min showing rms average power fluctuations below 0.3 %. The inset shows the beam profile of the high power pump pulses directly at the output of the power amplifier. b) Retrieved spectral intensity and c) Temporal profile of the high-energy 1030 nm pump pulses measured using a home-built SHG-FROG device after the grating compressor. The spectral and temporal phase are displayed in red. The retrieved pulse duration is 1.2 ps.

4.2 Layout of OPCPA Setup

The 470 W average compressor output power in the 1030 nm beam is used drive the self-seeded, high pulse energy, high repetition rate SWIR OPCPA setup. To keep pointing and pulse duration instabilities in the output of the main Yb:YAG thin-disk amplifier to a minimum, two active beam pointing stabilization systems are used in front of the grating compressor and the OPA setup, respectively. The OPCPA setup itself can be divided into three sections, the seed generation, the dispersion control and the power amplification section. This chapter gives a brief overview of the layout and purpose of the OPCPA-setups. A more detailed description of the design criteria, involved processes and output parameters for the seed-generation, dispersion control and power amplification setups is presented in the following sections.

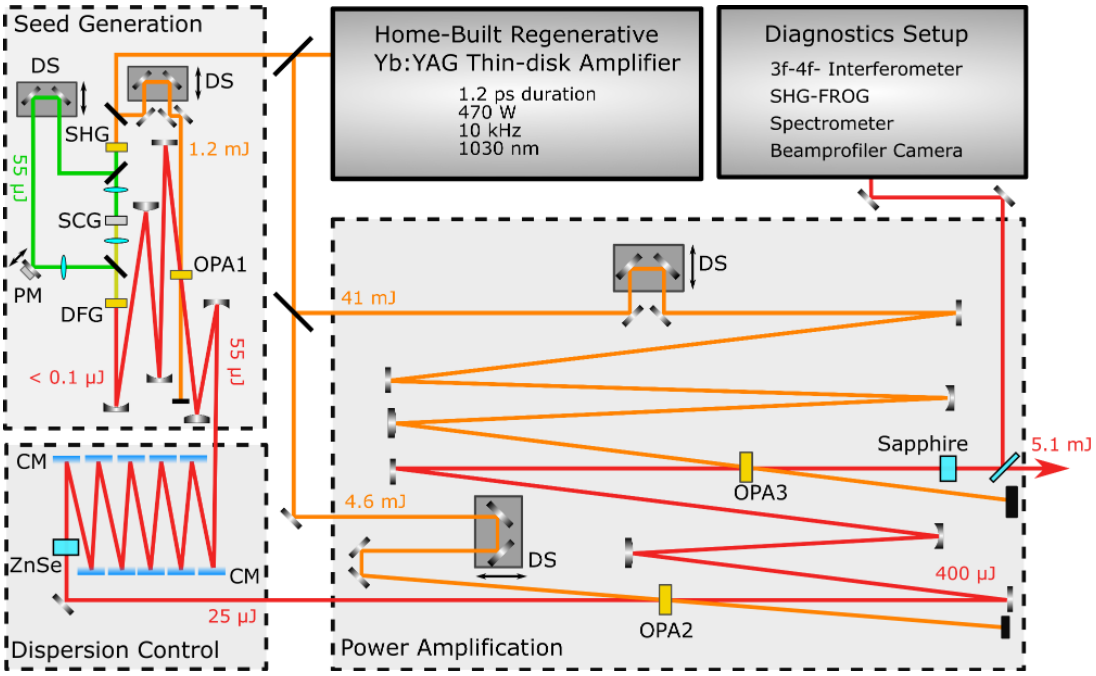

Figure 4.4: Schematic drawing of the high power SWIR OPCPA setup. CM: chirped mirrors, DFG: difference frequency generation, DS: delay stage, OPA: optical parametric amplification, PM: piezo mirror, SCG: supercontinuum generation, SHG: second harmonic generation.

The seed generation setup requires only a small fraction of the available pump power to generate the phase-stable 1.7 μm to 2.5 μm pulses. Approximately 1 W of the pump light is frequency doubled to 515 nm in an SHG stage which is divided into two channels. In the first channel, a supercontinuum (SC) is generated by bulk filamentation (SCG in Fig. 4.4). This SC was mixed with the remainder of the SHG to generate the CEP-stable SWIR pulses via a DFG process as described in Sec. 2.6. This approach for generating a CEP-stable SWIR seed for the OPA setup allows for a very compact footprint by avoiding the necessity to amplify the desired part of the SC prior to the DFG.

The sub-mW SWIR pulses from the DFG are then amplified in a first OPA stage pumped by approx. 11 W of the fundamental beam to measurable power levels in a first noncollinear OPA stage with an external noncollinearity angle of 1.5°. To ensure optimum amplification efficiency and compressibility, the amplified pulses from OPA stage 1 are sent into a dispersion control setup consisting of a combination of dispersive material and chirped mirrors. This setup compensates for the third order dispersion accumulated by the SWIR-pulses throughout the amplification stages. Additionally, it introduces enough positive dispersion to reverse the sign of the dispersion on the pulses. Thereby, it ensures high amplification efficiency while allowing post-amplification compression by dispersion in sapphire or other negative dispersion materials suitable for transmission of ultrashort multi-mJ pulses. Following the dispersion optimization, the SWIR pulses are subsequently amplified to multi-mJ energies in two additional noncollinear OPA stages using BiBO (OPAstage 2) and LNB (OPA stage 3) crystals. The external noncollinearity angles for OPA stage 2 and 3 are 2° and 1.9°, respectively.

4.3 CEP-stable Seed Generation

Generating broadband, CEP stable seed pulses is the most crucial part of the OPCPA setup since the bandwidth and noise properties achieved here will limit the performance of the whole laser setup. Thus, a robust and compact design is important to reduce pointing and phase instabilities in the DFG process. In this section, the layout and performance of the setup for generating phase- and energy-stable SWIR-seed pulses is described in more detail.

A thin film polarizer is used to split off 13 W of average power from the pump beam for the seed generation setup. This 13 W beam is then divided into two beams with 1 W and 12 W of power, respectively. The 1 W beam is frequency doubled in a 4 mm BBO crystal, generating 550 mW light at a wavelength of 515 nm (SHG). To generate a signal beam for the DFG process, 15 mW of this SHG are split off by a beam splitter and used to generate a SC by bulk filamentation (SCG in Fig. 4.4). Both YAG and sapphire are possible crystal choices for bulk filamentation using 515 nm picosecond pulses. While sapphire resulted in a larger spectral bandwidth, the SC generated in YAG had favorable stability regarding pulse energy and spectral shape. Sapphire crystals also require more pulse energy to generate a filament and suffered laser induced damage more frequently. Therefore, a 6 mm thick YAG crystal was used to generate the SC. The spectral components in the range between 650 nm and 750 nm (see Fig. 4.5 a)) are then spatially and temporally overlapped with the remaining 530 mW of the SHG.

Both beams are focused into a 3 mm lithium triborate (LBO) crystal to generate SWIR idler pulses covering the spectral range from 1.7 μm to 2.5 μm (See Fig. 4.5 b)) via a DFG process. While BBO has a higher nonlinear coefficient [105], its narrow acceptance bandwidth for the DFG process mixing 515 nm with a 650 nm-750 nm SC, limited the crystal thickness. To generate SWIR-pulses with a spectral coverage from 1700 nm– 2500 nm BBO crystals with a thickness below 1 mm were required. Therefore, LBO, allowing for a larger crystal thickness due to its wider phase matching bandwidth, resulted in an overall stronger broadband SWIR emission.

To avoid spatial chirp in the resulting idler pulses, the SC and SHG beams are recombined collinearly using a dichroic mirror in front of the DFG crystal. This approach, allows for small arm length of the interferometer formed by the SC and SHG pump light beam paths. In turn, a compact interferometer results in reduced pointing and path length fluctuations for the involved signal (SC) and pump (SHG) beams. This helps to reduce instabilities of the generated SWIR light in terms of power as well as CEP. The SWIR pulses centered at 2.1 μm wavelength generated in this DFG process are passively CEP stable due to the fact that the SHG- and SC-beams have identical phase noise which then cancels out during the DFG process (see Sec. 2.6). In contrast to intrapulse-DFG processes, however, the phase of the generated pulses is not exactly zero at creation but has a finite but static phase determined by the path length difference of this interferometer. This leads to slow CEP drifts due to path length changes caused by pointing or thermal drifts which are typically occurring on time scales of hours to seconds. These drifts need to be compensated to achieve long-term CEP stability and also present a simple way for active control of the relative CEP value (see sec. 4.6).

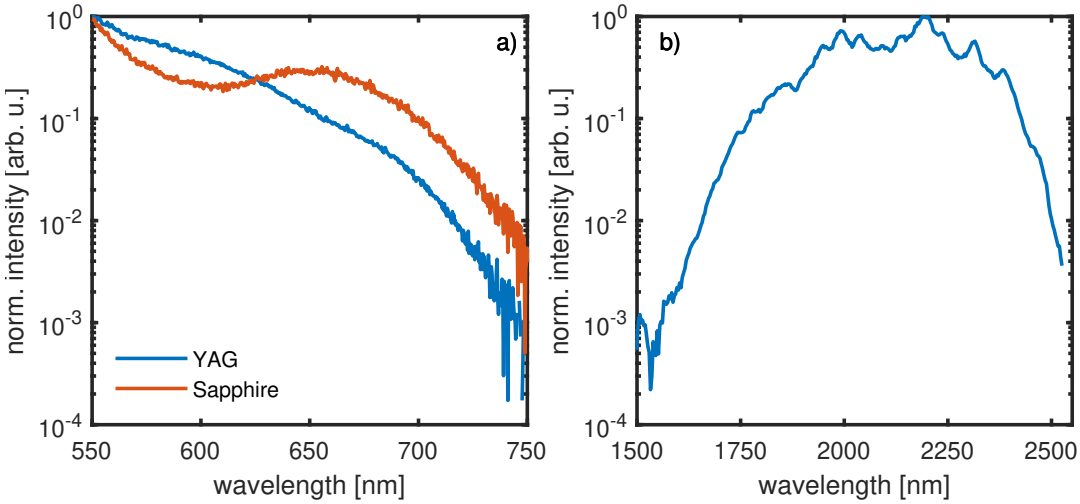

Figure 4.5: a) Supercontinuum spectrum generated from the 515 nm SHG in 8 mm Sapphire (red) and 6 mm YAG (blue). b) DFG Spectrum generated by difference frequency mixing the SC from a 6 mm YAG crystal with 530 mW of the SHG in a 3 mm LBO crystal.

In total, an average power of up to 3 mW of the broadband SWIR seed beam was generated by difference frequency mixing in a 3 mm thick LBO crystal, cut in XY-plane for type 1 phase matching with $\theta = 90°$, Φ =10.6°. Optimizing the conditions for stability and bandwidth, however, typically limits the DFG output to just below 1 mW. This power was insufficient for the characterization and optimization of dispersion, beam profile and output power of the pulses. Therefore, the SWIR idler was amplified in a first OPA stage pumped by the remaining 12 W of the 1030 nm fundamental beam that was split off for the seed generation setup. Both, SWIR-seed and fundamental pump beam, are focused into the first OPA crystal to a $1/e^2$-beam diameter of 1.5 mm under a noncollinearity angle of 1.5°.

The right choice of crystal is a crucial part for broadband seed-generation and high power parametric amplification. Multiple types of amplification crystals for 1030-nm-driven 2.1 μm OPAs can be used such as BBO, BiBO, LNB, LBO , potassium titanyle arsenate (KTA) and yttrium calcium oxyborate (YCOB). They all come with different strengths and limitations. Tab. 4.1 gives an overview of the optical properties of nonlinear crystals typically used in high-power OPCPA-setups. It also provides the information required to understand why a specific crystal was chosen for each of the nonlinear stages of the OPCPA-setup.

As BBO is less costly than BiBO, has a much higher damage threshold than LNB and a larger amplification bandwidth than YCOB or KTA, it is the most suitable crystal for the first OPA stage. With a pump peak intensity of $\sim$ 100 $\frac{\mathrm{GW}^2}{\mathrm{cm}^2}$, the achievable bandwidth optimized output power from the used 4 mm BBO crystal with a cutting-angle of $\theta = 21.4°$ amounts to 550 mW. However, after passing through the dispersion control setup, described in more detail below, only 250 mW are left to seed the power-amplification stages. At output powers beyond the few-W regime, OPA stages based on BBO suffer from the residual absorption of spectral components above 2300 nm, resulting in a drastic temperature increase and eventual thermally induced damage [106]. This effect prevents the usage of BBO in the power amplification stages.

Crystal	Interaction type	λ_p [nm]	λ_s (λ_i) [nm]	d_{eff} [$\frac{pm}{V}$]	$\delta\nu$ [cm^{-1}]
BBO [107]	type-1 OPA	(e) 1030	(o) 2060 (o) (2060)	1.85	43.3
BiBO [108]	type-1 OPA	(e) 1030	(o) 2060 (o) (2060)	2.6	63.0
LNB [109]	type-1 OPA	(e) 1030	(o) 2060 (o) (2060)	-4.025	72.0
YCOB [110]	type-1 OPA	(e) 1030	(o) 2060 (o) (2060)	-0.98	34.1
LiIO3 [111]	type-1 OPA	(e) 1030	(o) 2060 (o) (2060)	1.49	124.1
KTA [112]	type-2 OPA	(o) 1030	(o) 2060 (e) (2060)	-2.28	5.9

Table 4.1: Optical properties of nonlinear crystals relevant for SWIR-OPCPA setups. The amplification bandwidths have been calculated according to Eq. 2.68 for type-I phase matching and according to Eq. 2.67 for type-II phase matching. The effective nonlinear coefficient was calculated using the SNLO software by Arlee V. Smith [113]. For a better comparability, the values were calculated for a 1mm crystal with a pump intensity of 100 GW/cm². The sources for the Sellmeier-Coefficients used in the calculation are cited next to the crystal names.

4.4 Broadband Amplification to multi-mJ Energy

As the pulses from the seed generation setup do not have sufficient pulse energy for high-cutoff HHG, broadband amplification of the SWIR pulses is necessary. This section discusses the design, performance and the challenges for the broadband amplification in the presented OPCPA-setup. The amplification process has to preserve the spectral bandwidth, CEP stability and pulse energy stability of the seed pulses and must not introduce distortions in the spatio-temporal profile of the SWIR-beam. Achieving this requires the right choice of amplification crystals, and a careful management of thermal loads and beam sizes throughout the setup to avoid thermal and nonlinear lenses.

A nonlinear lens forming in air is observable due to the high peak power of the 1.2 ps 470 W compressed pump beam which can cause damages to mirrors, crystals or even water-cooled beam dumps. Fully avoiding this nonlinear lens caused by propagation through several meters of air would only be possible by operating the laser setup in a vacuum. However, the effect can be mitigated by increasing the beam diameter of the pump light, effectively shifting the focal spot of the nonlinear lens far beyond the actual length of the setup. Therefore, the pump beam from the Yb:YAG thin-disk power-amplifier was expanded to a diameter of 15 mm prior to compression in the grating compressor. The nonlinear lens, however, becomes a critical aspect for a further increase of pump pulse energy or average power to make full use of the kW potential of the main power amplifier. Higher pulse energies will require even larger beam diameters to avoid self-focusing issues which makes the beam more prone to instabilities due to air turbulences. Increasing the average power while keeping the

energy constant, e.g. by increasing the repetition rate of the laser system, will result in a significant increase of thermal load. Therefore, increasingly strong air turbulences and thermal lensing which will in turn promote the issue of self-focusing are to be expected.

After splitting off the portion used for the seed generation, the remaining $\sim$ 456 W of pump light is divided into a 46 W channel for OPA stage 2 and a $\sim$ 410 W channel for OPA stage 3. Only after dividing the power between the channels, the beam diameters are reduced from 15 mm to 3 mm in OPA 2 and 12 mm in OPA 3, resulting in peak pump intensities of $\sim$ 125 $\frac{\mathrm{GW}}{\mathrm{cm}^2}$ and $\sim$ 50 $\frac{\mathrm{GW}}{\mathrm{cm}^2}$ on the respective crystals. An overview of the crystals used in the nonlinear stages of the setup is given in Tab. 4.2.

Crystal	Stage	d [mm]	θ	Φ	I_{peak} [GW/cm^2]	CA ø [mm]
LBO	DFG	3	90°	10.6°	110	8
BBO	OPA 1	4	21.3°	-	105	8
BiBO	OPA 2	2	7.8°	0°	102	12
LNB	OPA 3	2.2	42.9°	-	50	25

Table 4.2: Overview of the crystals used in the DFG- and the three OPA stages of the SWIR-OPCPA setup. CA denotes the clear-aperture diameter of the crystals and d denotes the crystal thickness. Θ and Φ denote the angles between the pump beam and the respective crystal axis as described in Sec. 2.6.2 .

In the second OPA stage a 2 mm thick BiBO crystal is used, as BiBO has a higher effective nonlinear coefficient, larger acceptance bandwidth and more favorable absorption properties than BBO and thus suffers less from an increasing temperature due to absorption above 2300 nm [114, 115]. However, BiBO crystals in the required size are also significantly more expensive. The crystal is cut in the XZ-plane with a cutting-angle of θ= 7.8°.

The measured and simulated output spectra of all nonlinear stages for generating and amplifying the SWIR-beam in the OPCPA-setup are depicted in Fig. 4.6 in blue and red, respectively. The simulations are full 3D-simulations done with the Lightwave Explorer software [86] and take into account the noncollinearity angles and second and third order dispersion of the beams. However, the simulation is based on Gaussian seed and pump spectra for each stage and assumes an absence of material absorption. Despite these limitations, the measured and simulated spectra are in good agreement and share many characteristic features. A comparison of the input seed spectrum (OPA1) and the output spectrum (OPA2) in Fig. 4.6 b) and c), respectively, shows that the second OPA stage is slightly less broadband and the wavelengths above 2450 nm are not amplified efficiently. This reduction in bandwidth is likely caused by the rather big external noncollinearity angle >2° between the seed and the pump beam, which is necessary to safely split the SWIR beam from the pump beam after amplification, slightly reducing the bandwidth of the amplification process. The output spectra of the first and second OPA stage both exhibit a distinct spectral shape with peaks in the spectral intensity to both sides of the spectrum and less spectral intensity in the center. This shape is a characteristic feature of the phase matching behavior in degenerate OPA stages when the phase matching angle is slightly detuned from phase matching the degeneracy frequency (see Fig. 2.8 in Sec. 2.6). This detuning is introduced to increase the amplification bandwidth of the

first two OPA stages at the cost of a slightly reduced amplification gain. Even higher amplification bandwidth could be achieved by further detuning the phase matching angle of the crystal. However, this causes a significant reduction in amplification gain.

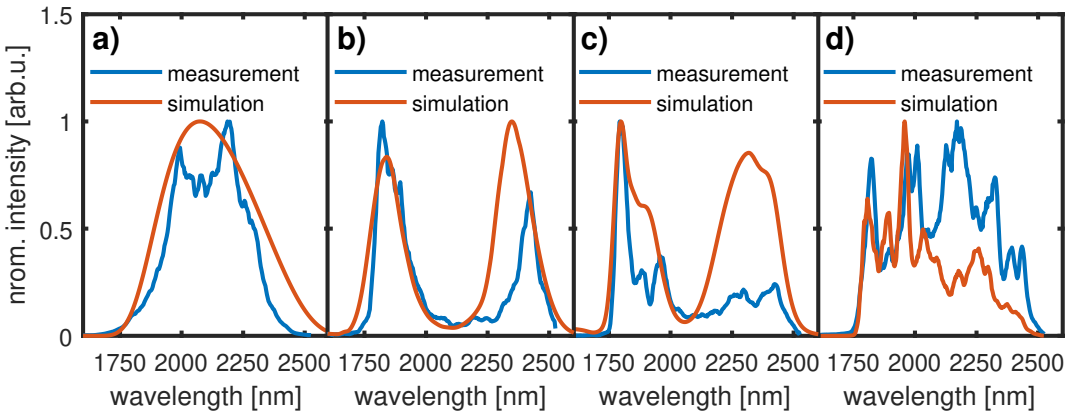

Figure 4.6: Output spectra of the DFG-stage (a) and of the first (b), second (c) and third (d) OPA stage. Measured spectra are depicted in blue, the spectra depicted in red are the results from simulations using the Lightwave Explorer software [86]. The simulations are full 3D-simulation for Gaussian-input spectra taking into account second and third order dispersion as well as the noncollinearity angles of the stages.

In the final OPA stage (OPA 3) the up to 410 W of pump power used for amplification impose even more challenging requirements to the nonlinear crystal. The high energy of the pump pulses makes it necessary to significantly increase the beam size in order to avoid peak intensities above the damage threshold of the crystal. Therefore, BiBO can no longer be used at such high powers as BiBO crystals with clear apertures > 15 mm are not readily available. KTA and YCOB crystals are available in large sizes and have damage thresholds superior to BBO or BiBO but result in a limited bandwidth of the SWIR output pulses since KTA does not support broadband phase matching in this spectral region and the low nonlinear coefficient of YCOB demands for thicker crystals (see Tab. 4.1). LNB has a low damage threshold compared to BBO and BiBO and photorefractive effects can lead to a catastrophic runaway focus process resulting in crystal damage at peak intensities of the pump light exceeding $50\ \frac{\mathrm{GW}}{\mathrm{cm}^2}$ [106, 116]. Even at a pump power of 410 W, however, large aperture diameter LNB crystals easily allow the beam sizes necessary to keep the peak intensity below the damage threshold. The broadband phase matching conditions and a strong nonlinearity with a nonlinear coefficient of $|d_{\mathrm{eff}}| > 4\ \frac{\mathrm{pV}}{\mathrm{m}}$ [105] enable broadband and efficient amplification even at lower pump peak intensities. Additionally, LNB has a low absorption coefficient over the full spectral range of the SWIR pulses [117], resulting in a reduced thermal load as compared to BBO or BiBO crystals. Despite the low absorption coefficient, the crystal temperature rises reaching a steady equilibrium temperature of 45 ± 2 °C when the stage is operated at approximately 400 W of pump power. The LNB crystals used here are cut at a phase matching angle of $\theta = 42.9°$ and are mounted into motorized mirror mounts providing an easy way to compensate the temperature induced shift in optimum phase matching angle by tilting the crystal.

Comparing the spectrum of the SWIR pulses after amplification in a 2.2 mm LNB to 51 W of average power in Fig. 4.6 d) with the spectra recorded for the previous

amplification stages shows no further decrease in spectral bandwidth. Compared to other high-power OPCPA-systems relying on power amplification in KTA or YCOB, the usage of LNB allows for a considerably higher amplification bandwidth and thus shorter compressed pulse duration after the OPA. I note here, that initially two 1.2 mm LNB crystals were inserted in the overlap region of the third OPA stage in order to achieve a larger interaction length avoiding a reduction in bandwidth by phase matching different spectral regions in the separate crystals. This configuration is referred to as the double crystal approach below and its advantages and challenges are discussed in Sec. 4.5. Using a singular 2.2 mm LNB crystal ultimately proved to achieve better results compared to the double crystal approach.

In contrast to the first and second OPA stage, the output spectrum of OPA stage 3 shows a higher spectral intensity in the center of the spectrum. This reflects the more Gaussian gain profile as detuning the phase matching angle was not necessary due to the large acceptance bandwidth of the LNB crystal. The spectrum of the amplified pulses supports a Fourier-transform-limited duration of 17 fs. Benefiting from the compact setup, excellent stability with below 0.8 % rms average power fluctuations for approximately one hour of operation can be achieved even at output powers beyond 45 W (Fig. 4.7).

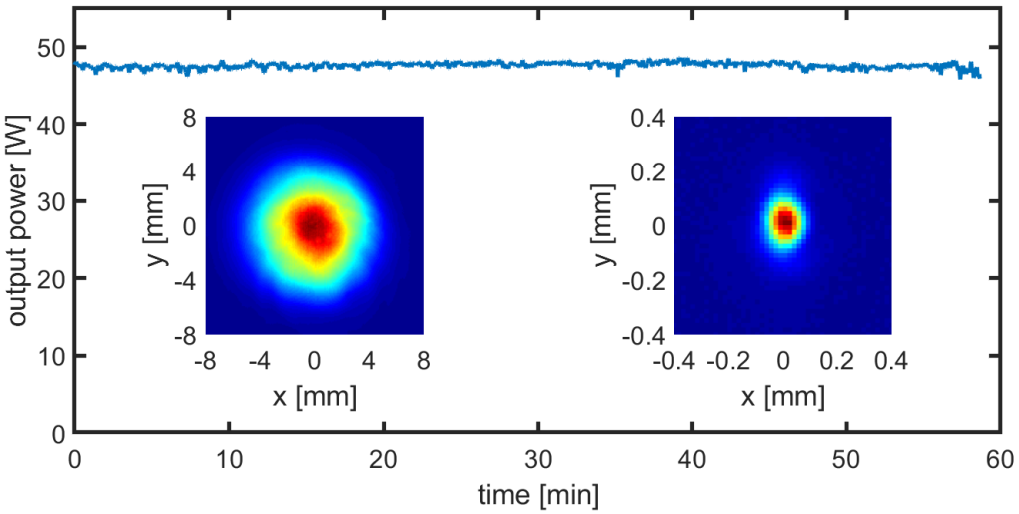

Figure 4.7: Average output power of the three stage high power SWIR-OPCPA setup, recorded with a water-cooled thermopile power sensor for $\sim$ 1 hour. The average power amounts to 47.6 W with a standard deviation of 0.8 %. The insets show the beam profile of the SWIR-pulses directly after the third OPA stage with 395 W of pump light applied (left) and in the focus of a 500 mm focus distance curved mirror (right).

The beam profiles shown as insets to Fig. 4.7 have been recorded on the wedge-reflection of the output beam at 395 W of pump power. The inset to the left shows the output beam profile from the third OPA stage after approximately 1 m of propagation, recorded with a (Spiricon Pyrocam IV) beam profiler camera. The beam has a $1/e^2$-diameter of approximately 12 mm and a near Gaussian profile. The inset on the right of Fig. 4.7 shows an image of the beam in the focus of a 500 mm focal length spherical mirror and was measured with a microbolometer camera (Swiss Terrahertz Rigi M2).

This image reveals an overall good focusability with a near Gaussian shape preserved also in the focus of the beam. The general beam quality of the SWIR output pulses is investigated further below in Fig 4.11. I note here, that all OPA stages are operated in a regime where the output power still depends linearly on the applied pump power. This avoids the back-conversion regime and the associated distortions of the spatio-temporal profile of the SWIR-pulses which result in significant reduction of HHG efficiency [118, 119]. Fig. 4.8 a) and c) illustrate the linear dependence of output power on the applied pump power in the chosen operating regime for the second and third OPA stage, respectively. Additionally, the output power as a function of the input seed power is displayed for the second (b) and third (d) OPA stage. Additionally to the measured values, the output power of the OPA has been simulated in 2D using the Sisyfos nonlinear propagation library [120, 121, 122].

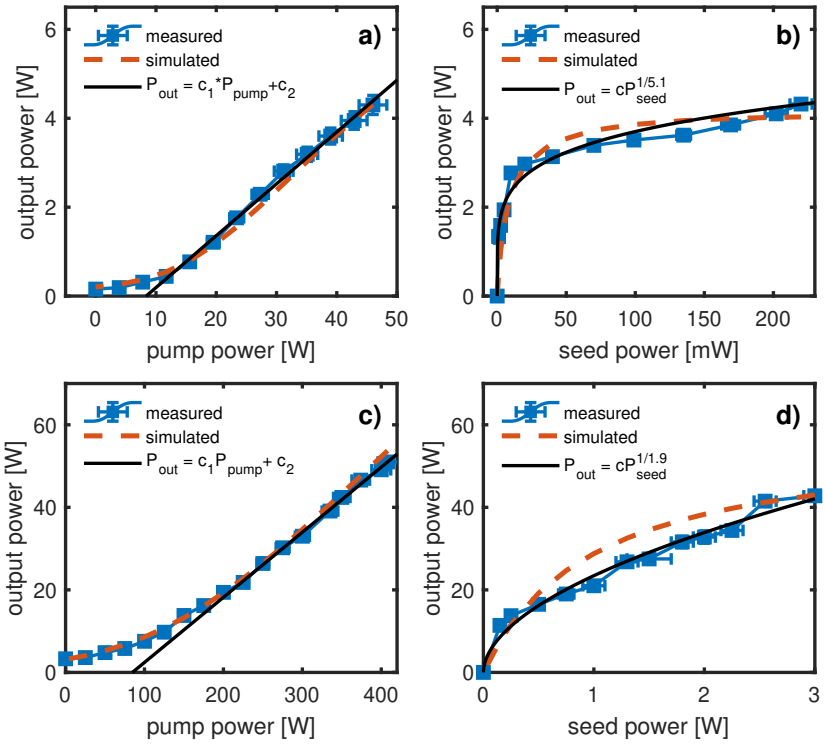

Figure 4.8: a) Measured (blue solid) and simulated (dashed red line) average SWIR-output power of OPA stage 2 as a function of pump power. The solid black line is a linear fit to highlight the linear increase of output power with applied pump power. b) Measured (blue solid) and simulated (dashed red line) average SWIR-output power of OPA stage 2 as a function of seed power. c) Measured (blue solid) and simulated (dashed red line) average SWIR-output power of OPA stage 3 as a function of seed power. The solid black line is a linear fit to highlight the linear increase of output power with applied pump power. d) Measured (blue solid) and simulated (dashed red line) average SWIR-output power of OPA stage 3 as a function of pump power. The error bars displayed in the graph represent the rms noise of the respective power measurement in a $\sim$ 30 s observation time. However, the necessity for frequent realignment and adjustments of the phase matching angle might have caused a larger measurement error.

The results of the simulations in Fig. 4.8 are depicted in red. The simulations for the pump and seed power scan experiments for the respective OPA stage share the same input parameters with exception of the scanned parameters. The parameters of

the simulation are kept as close to the real conditions as possible. The simulations, however, only account for Gaussian input spectra with second order dispersion. Good agreement between the experimental data and simulations can be achieved within the limits of the simulation if pulse durations of $\sim$ 0.8 ps and $\sim$ 1 ps are assumed for the SWIR-seed-pulses in OPA stage 2 and 3, respectively. While those values are realistic, simulations with other pulse durations (not shown in the figure) suggest, that slightly longer pulse durations could result in an overall better amplification efficiency, perhaps allowing for an increase of output power to up to 60 W from OPA stage 3. This could be achieved by implementing a pair of zinc selenide (ZnSe)-wedges into the dispersion control setup between OPA 1 and OPA 2 which would allow for a variable fine-tuning of the dispersion. In the current setup, however, the dispersion control with chirped mirrors and ZnSe-windows with a thickness of ≥ 3 mm lacks the flexibility to further optimize the efficiency of the OPA process.

While the output power scales linearly with the pump power for both the second and the third OPA stage, the dependence of the output power on the seed power shows a different behaviour, implying that the two stages differ in the degree of saturation. For the third OPA stage, a square-root like behaviour can be observed, suggesting that the stage reaches a weak saturation state indicated by the small deviation from the linear scaling in a small signal limit. The second OPA stage is driven considerably further into saturation with an output power scaling proportional to $\sim P_{seed}^{1/5}$. However, it is evident from the linear scaling with pump power and the conversion efficiency of 9.3 % that the second OPA stage is still in an intermediate saturation regime which should be unproblematic in regard to back-conversion induced phase distortions which could limit HHG efficiency [118].

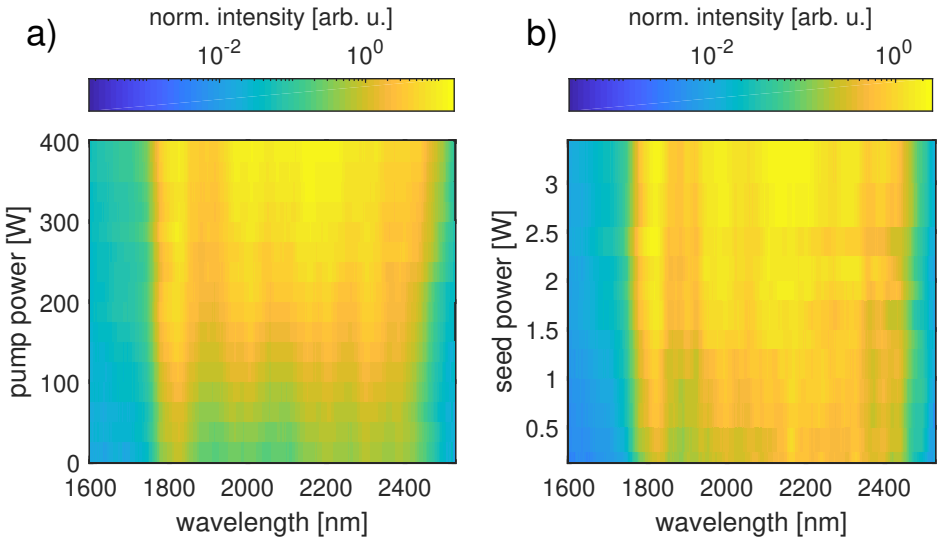

Figure 4.9: Evolution of the output spectrum of the third OPA stage with increasing pump (a) and seed power (b). The color coded spectral intensity is normalized to the maximum value of the spectral intensity at the lowest pump power, and lowest seed power, respectively and displayed on a logarithmic scale.

While the general output power of the power amplification stages does not show critical saturation levels, observing the average power alone does not give the full pic-

ture. It might happen that certain spectral or spatial regions are driven much further into saturation then others. The reason for this is the inhomogeneous spatial, spectral and temporal intensity distribution of the involved chirped pulses which result in local variances of the achieved gain. Thus, spectral components which have better temporal and spatial overlap with the high intensity regions of the pump pulses might exhibit stronger saturation effects than others. It is evident from the Gaussian beam profile of the SWIR-pulses after amplification that strong spatial differences in saturation levels do not occur, as this would lead to a more flat top or even donut like shape of the beam profile.

To investigate this effect in the spectral domain, the spectrum of the pulses after amplification was measured for each data point shown in Fig. 4.8. The recorded spectra for the pump and seed power scan are displayed in Fig. 4.9 a) and b), respectively. The seed power during the pump power scan was kept constant at 340 mW and during the seed power scan a constant pump power of 400 W was applied. The color coded spectral intensities are normalized to the maximum of the spectral intensity at the lowest pump and seed power, respectively. While the spectrum is certain to change during amplification due to the inherent gain spectrum of the amplification stage, the intensity recorded for each wavelength should grow monotonically and follow a similar behaviour as the overall average power displayed in Fig. 4.8. It is evident from Fig. 4.9 that the spectral shape does not change drastically during amplification and most dips and peaks in the spectrum are already present at low pump and seed powers and just get more pronounced at higher power levels. The stronger amplification in the center of the spectrum, discussed for the output of the third OPA stage before, is the most noticeable change in spectral shape and results in a shift of the maximum spectral intensity towards the center of the spectrum at pump powers beyond 250 W in Fig. 4.9 a). The spectral intensity also does seem to grow monotonically with pump power and seed power in a) and b), respectively, at all wavelengths within the limits of the experimental error. However, a closer inspection for the spectral regions with the highest power is expedient. Thus, the evolution of the spectral intensity with applied pump and seed power at certain wavelengths is displayed in Fig. 4.10 a) and b), respectively. The choice of wavelengths was made specifically to catch the spectral regions most likely to exhibit stronger saturation, which is the wavelength with the highest spectral intensity in the seed beam at 1822 nm and the wavelength of the highest spectral intensity when the full pump and seed power is applied at 2158 nm.

Fig. 4.10 a) shows a behaviour of the spectral intensity at the selected wavelengths very similar to the overall power scaling shown in Fig. 4.8 c) with a super linear increase at low pump powers and a linear increase at higher powers. However, at 2158 nm, a noticeable deviation from the linear behaviour emerges and the curve flattens at powers beyond 375 W. This suggests that energy conversion from the pump pulse into this specific spectral region of the signal pulses is already approaching saturation while other spectral regions are not. This might be due to spatio-temporal walk-off effects or the general spatio-temporal structure of the signal pulses [123]. However, the level of saturation reached should not yet be detrimental to the spatio-temporal structure of the pulses. As none of the spectral components of the SWIR-signal pulses actually reaches the back-conversion regime, no strong distortions in the spatio-temporal structure [118] and therefore, no loss of HHG efficiency [119] are expected. Additionally, the output power scaling for the seed power scan shown in

Fig. 4.10 b) at the same wavelengths does not show a similar saturation behaviour neither at 1822 nm nor at 2158 nm. This also indicates that a full saturation or even back-conversion of energy from the signal to the pump pulses does not occur. Thus, the spatio-temporal structure should yet be undisturbed by the amplification process.

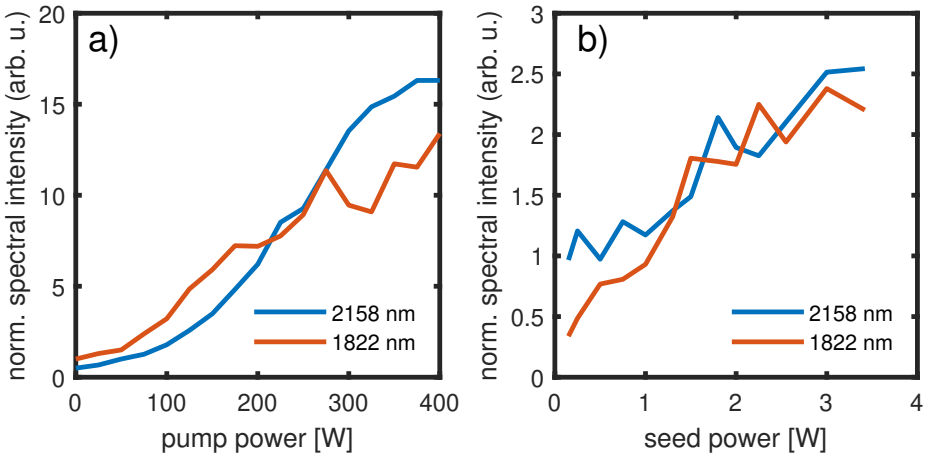

Figure 4.10: Intensity scaling of the SWIR-pulses with pump power (a) and seed power (b). The curves in a) and b) represent vertical cuts at 1822 nm (the wavelength of the maximum intensity of the input seed spectrum) and 2158 nm through the intensity map shown in Fig 4.9 a) and b), respectively.

As for many experiments, efficient HHG requires not only high pulse energies and a clean spatio-temporal profile, but also a good focusability and overall spatial beam quality. The spatial properties can be characterized by the M^2 beam quality parameter introduced in Sec. 2.2.1. To ensure a good beam quality, the M^2 parameter was investigated at various pump powers for the third OPA stage in the double LNB crystal configuration. As the observed beam doesn't have a perfect Gaussian profile in space, it is of great importance to the measurement to use the D4-σ-beam diameters defined in Sec. 2.2.1 when calculating the M^2-values. Additionally, the camera used to measure the beam profile needs a large enough sensor to accommodate for the beam size far from the focus. Furthermore, a high enough spatial resolution to resolve the beam in the focus is required. While it is possible to measure a beam profile using two-photon absorption on a silicon detector, this approach will likely distort the results due to the quadratic scaling of the signal with intensity and the dependence of the signal on the temporal length of the pulses. Therefore, the D4σ beam diameter was determined from images taken with a 17 μm pixel pitch microbolometer camera (Swiss Terrahertz RIGI- M2), offering a good enough spatial resolution for the 180 μm beam radius in the focus at a detector size of $>$ 10 mm x 8 mm. The M^2 was measured only in the double crystal configuration. However, the results should be equivalent for the singular 2.2 mm LNB crystal at the same applied pump powers. Due to the walk-off and phase differences in the two separate crystals, it is even expected that the double crystal approach results in additional distortions and has an overall detrimental effect on the beam quality.

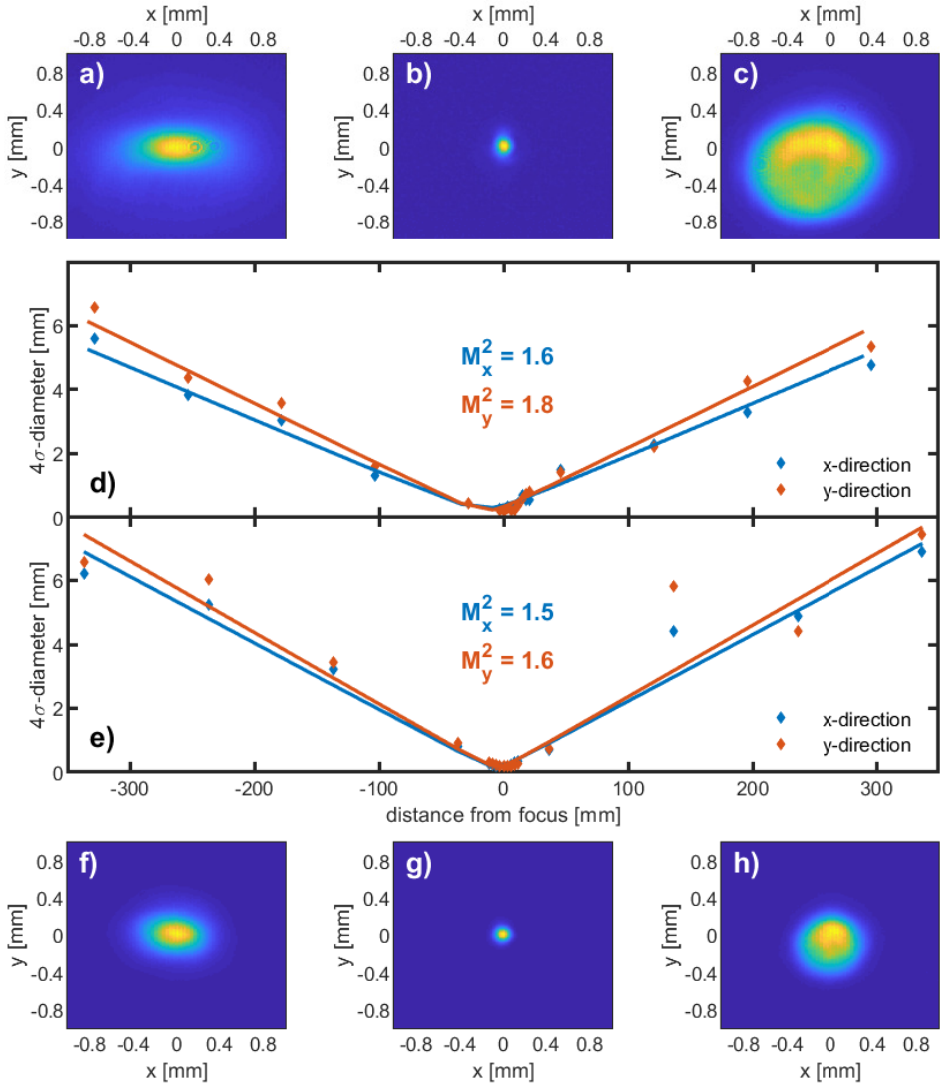

Figure 4.11: Results of the beam quality measurement for the OPCPA output after OPA stage 3. The beam profile was measured using a microbolometer camera with 17 μm pixel pitch. a)-c) show the beam profile measured with 390 W of pump power applied to the LNB crystals at a distance of $\sim$ -10 mm (front) 0 mm and $\sim$ 10 mm (back) from the focus, respectively. After the focus, a donut-like shape emerges as can be seen in c) which is responsible for the increased M^2 values as compared to the low-power case. d) and e) show the D4σ-beam diameters (see Sec 2.2.1) retrieved from the measurements at 395 W and 280 W, respectively. The values for the X-direction are displayed in blue while the values for the Y-direction are displayed in red. The data has been fitted according to equation 2.21 to retrieve the respective M^2 values of $M^2_X = 1.6$ and $M^2_Y = 1.8$ for the high power and $M^2_X = 1.5$ and $M^2_Y = 1.6$. for low power measurement. In both cases, the measurement of OPCPA output beam caustic shows low astigmatism and ellipticity and a generally good focusability with a near Gaussian profile in the focus. f)-h) show the beam profiles measured for the low power beam at distances from the focus equivalent to those displayed in a)-c). The data shows that the donut-like shape is much less pronounced in the low power measurement.

The measured 4σ-beam diameters in X- and Y-direction and the fit according to Eq. 2.21 used to retrieve the M^2 values are displayed in Fig. 4.11 d) and e) for the beams pumped at 390 W and 280 W, respectively. At pump powers $<$ 280 W, the M^2 value was measured to be $\sim$ 1.5 in X- and $\sim$ 1.6 in Y-direction. When the pump

power was increased beyond this threshold, the beam quality gradually decreased. This resulted in e.g. an M^2 value of $\sim$ 1.6 in X- and $\sim$ 1.8 in Y-direction at a pump power of 390 W. The reason for the decrease in beam quality (increase in M^2 value) is the emergence of a non-Gaussian beam profile after the focus, which is displayed in Fig. 4.11 c). A comparison with the profile of the 280 W pumped beam at an equivalent distance after the focus in Fig. 4.11 h) shows that the beam distortion is much less pronounced if the pump power of the OPA stage is reduced. Despite this distortion, the SWIR beam in case of high pump power is still focusable with a nearly Gaussian shape in the focus as can be seen in Fig. 4.11 b). In front of the focus, the beam distortion is not observed in both cases as can be seen from Fig. 4.11 a) and f).

The decrease in beam quality is likely to be caused by a thermal lensing effect in the LNB crystals of the third OPA stage which results in the development of the non-Gaussian beam profile after the focus. To further investigate the thermal conditions during operation of the OPCPA, the temperature of the OPA crystals was measured for various applied pump powers. While the temperature in the first OPA crystal rises only by 2±1 °C above room temperature even when the full 10 W of pump light is applied, the significantly larger amounts of pump power used in the second and third OPA stage lead to higher temperatures. The measurements for the second and third stage are shown in Fig. 4.12. The temperature of the crystals was measured during laser operation using a (Testo 882) thermal imaging camera. The error values assigned to the temperature here refer to the limited read out precision of the camera. The absolute temperature precision of the camera is specified to be ± 2 °C, but is less relevant for judging temperate differences. Fig. 4.12 a) shows a thermal image of the BiBO-crystal in OPA stage 2. The position of the pump-signal-overlap region is clearly visible from the higher temperature at the bottom left of the crystal. 4.12 b) shows that the temperature measured in the overlap region increases from the ambient air temperature of 23±0.5 °C if no pump light is applied to 28± 0.5 °C when pumped by 46 W of 1030 nm light. While potentially inducing a weak thermal lens, this overall moderate increase in temperature is not expected to lead to severe beam distortions. In OPA stage 3, however, the applied pump power is significantly higher with up to 410 W applied to the crystal. Even at the low absorption of LNB, this amount of average power leads to a considerable temperature increase. The thermal image displayed in Fig. 4.12 c) of the LNB-crystal pumped with 395 W of average power demonstrates the larger beam diameters leading to an increased temperature profile covering nearly the full 25 mm clear aperture of the crystals. However, the aluminum mount of the crystal remains comparatively cool revealing a low amount of stray pump light exposure outside the clear aperture of the crystal. The temperature of the crystal was again measured in the center of the overlap region of the pump and signal beam for different average pump powers applied.

Fig. 4.12 d) shows the linear increase of the temperature from 25± 0.5 °C with no pump light applied to a temperature of 45.3± 0.5 °C at 395 W. This temperature increase is strong enough to lead to a significant change in refractive index and phase matching conditions of the crystal, resulting in the necessity to readjust the crystals phase matching angle during the warm-up-phase of the setup and leading to a thermal lensing causing the reduction in beam quality observed in Fig. 4.11 c). Additionally, the temperature of the crystal in OPA stage 3 was measured depending output power while the full 400 W of pump power were applied to the crystal. In this case, the

output power was adjusted by detuning the phase matching angle of the crystal. The results of this measurement are shown in Fig. 4.12 d), depicted in red. The overall weak dependence of the crystal temperature on the output power at full pump power shows the low linear absorption of the crystal at the signal and idler wavelengths.

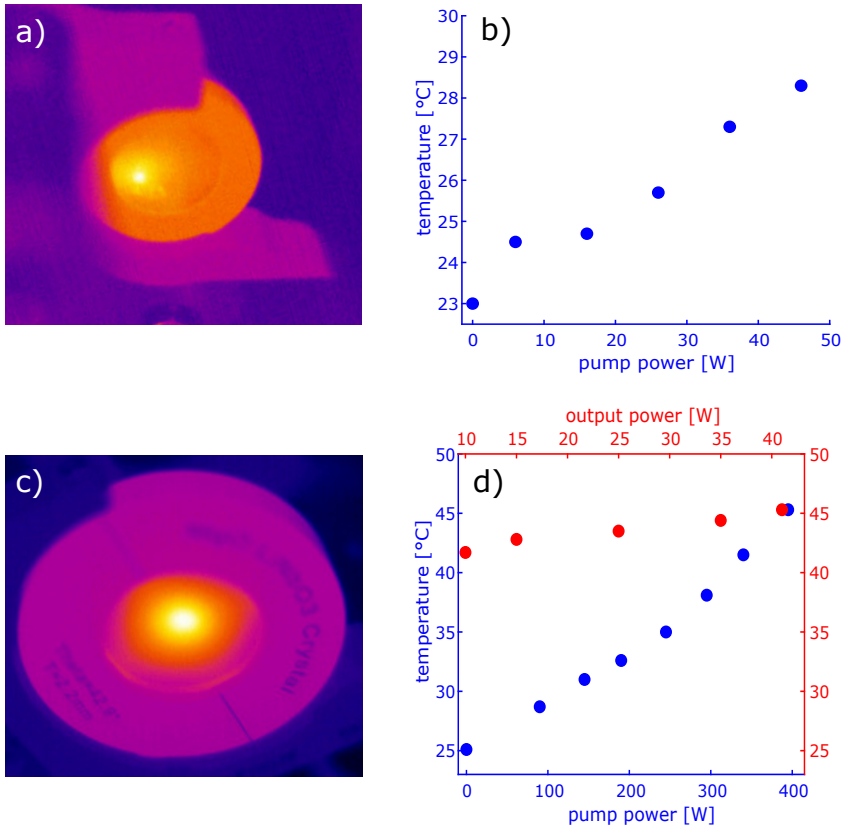

Figure 4.12: a) Image of the second OPA crystal recorded with a thermal imaging camera. b) Temperature of the BiBO-crystal used in OPA stage 2 at the overlap position of pump and seed beam. c) Image of the LNB-crystal in the third OPA stage recorded with a thermal imaging camera. d) Double-x-axis plot of the temperature of the LNB-crystal in OPA stage 3. The temperature depending on the applied pump power is displayed in blue (bottom x-axis), showing a linear increase of temperature up to $\sim$ 45$\pm$ 0.5 °C at 400 W of pump power. With the full 400 W of pump power applied to the crystal, the phase matching angle was detuned and the crystal temperature was measured depending on the SWIR output power after OPA stage 3. The results from this measurement are shown in red (top x-axis).

4.5 Dispersion Control and Compression

Since this laser system is meant to drive HHG with cutoff energies well into the water window, it is essential to generate few-cycle pulses, as it increases the available peak intensities and enables the utilization of amplitude gating for isolated attosecond pulse generation. This chapter describes the measures taken to allow for few-cycle pulse compression and the results of pulse duration measurements with an SHG-FROG-device (see Sec. 2.7.1). The generated SWIR spectrum after amplification in the third OPA stage shown in Fig. 4.6 d) supports a Fourier-limited pulse duration as short as 17 fs, corresponding to 2.4 optical cycles at a center wavelength of 2.1 μm. A combination of Sapphire, ZnSe and custom chirped mirrors is used to control the dispersion of the SWIR pulses to maximize the amplification efficiency as well as to compress the output pulses of the third OPA stage.

The supercontinuum used as a signal during the DFG process generating the CEP-stable seed pulses is chirped due to positive dispersion in the YAG crystal used to generate the SC light. Due to the mixing process in the LBO crystal generating the difference frequency of the overlapping SHG and SC fields, the chirp is reversed for the generated idler. Hence, the resulting SWIR-seed pulses have negative chirp. Most transparent materials, however, including the amplification crystals used in OPA stage 2 and 3 and the sapphire material meant to compress the pulses later on, introduce negative GVD. While materials like ZnSe or multilayer chirped mirrors can be used to induce positive second order dispersion, both of these options are not suitable for compressing high energy, few-cycle pulses due to damage thresholds, thermally induced dispersion shifts and random quasi phase matching [124, 125, 126].

Therefore, to ensure good temporal profile matching between the SWIR signal and 1030 nm pump pulses, a dispersion control setup was implemented inbetween the first and second OPA stage consisting of 10 mm ZnSe and two types of custom chirped mirrors with eight and two bounces, respectively. Due to the large amount of dispersive material in the setup, the TOD cannot be neglected when trying to compress the pulses close to their bandwidth-limited duration.

This issue, however, is addressed by the chirped mirrors in the dispersion control setup. The first set of chirped mirrors was reported in [106] and accumulates negative TOD and positive GDD compensating 40 mm of sapphire during the eight bounces on the mirrors. Together with the positive dispersion of the 10 mm ZnSe enough GDD is introduced to first compensate for the native negative second order dispersion of the SWIR pulses and then stretch the pulses to a duration allowing for high efficiency in the subsequent OPA stages. The remaining TOD of the output pulses is (pre-)compensated by two passes on the second type of chirped mirrors, which introduce negative TOD while having little effect on the second order dispersion of the pulses. Pre-compensating the TOD allows for pulse compression after the power amplification to the multi-mJ range, solely by introducing 18 mm sapphire, including entrance windows to the vacuum beamline and pick-off windows for diagnostics later on. The fine tuning of the duration of the amplified pulses is done using a pair of fused silica wedges. At a $1/e^2$ beam diameter of 14 mm the estimated B-integral in the compression material according to Eq. 2.44 amounts to 0.37 rad, which is small enough to not expect a degradation of the beam quality due to nonlinear effects in the solid-state compression unit. Additionally, a change in spectrum or beam profile

of the output pulses was not observed when the compression material was inserted, even at a reduced beam diameter of 10 mm.

At OPA 3 an output power of up to 51 W was achieved from a single 2.2 mm thick LNB crystal. The generated SWIR pulses were characterized using a SHG-FROG measurement, yielding a 20.4 fs pulse with 89 % of the intensity confined in the main pulse (Fig. 4.13 b)).

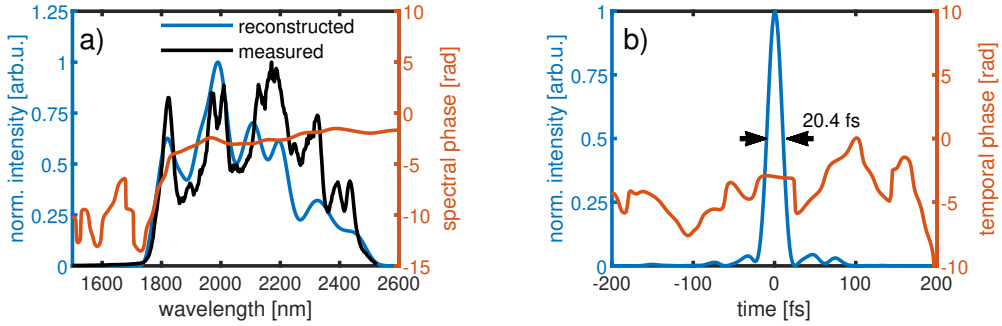

Figure 4.13: Results of the SHG-FROG measurements on the SWIR-output after amplification in the 2.2 mm LNB-crystal to 5 mJ. A small portion of the output pulses was compressed by propagating thru 18 mm of sapphire. The fine adjustment of the dispersion for optimal compression was done using a pair of fused silica wedges. a) Shows the measured (black) and retrieved spectrum (blue) along with the retrieved spectral phase (red) in. b) Shows the reconstructed temporal profile of the compressed pulses (blue) and the retrieved temporal phase (red).

Shorter pulses with 18.5 fs duration were achievable with a double crystal approach using two 1.2 mm LNB crystals phase matching different parts of the input spectrum. This technique is widely used to achieve a higher amplification bandwidth while still having the benefits of a thick crystal [127]. However, the shorter pulse duration was achieved at the cost of an average output power reduction to 40 W due to the walk-off inbetween the crystals. Additionally, the use of two crystals in a noncollinear geometry led to the development of modulations in the output spectrum which result in either formation of multiple pulses or an energy transfer from the main pulse to a pedestal with a duration of several hundred of fs.

To counter this effect, the two 1.2 mm thick LNB crystals into the same mount to keep the distance between the crystals with $\sim$ 1 mm as small as possible. This approach achieved the best results despite the fact that the phase matching angle of the two crystals cannot be adjusted independently. Additionally, careful alignment of the input beams, a small noncollinearity angle and operating the crystals in a walk-off-compensating scheme [128, 129], helped to mitigate those effects, resulting in a decently compressible pulse. Fig. 4.14 shows the SHG-FROG reconstruction of the spectrum (a) and temporal profile (b) of the output pulses from the third OPA stage in case of optimal alignment (blue) and for a pulse typically achievable in day-to-day operation without taking special optimization of the OPA 3 alignment (red).

Compressed pulse durations as short as 18.5 fs could be achieved with $\sim$ 50 % of the total pulse energy contained in the main pulse for optimal alignment. This suggests that using a single crystal is preferable when aiming for the highest peak powers, whereas experiments relying on the shortest possible pulses for nonlinear processes such as amplitude gating in HHG could benefit from the double crystal

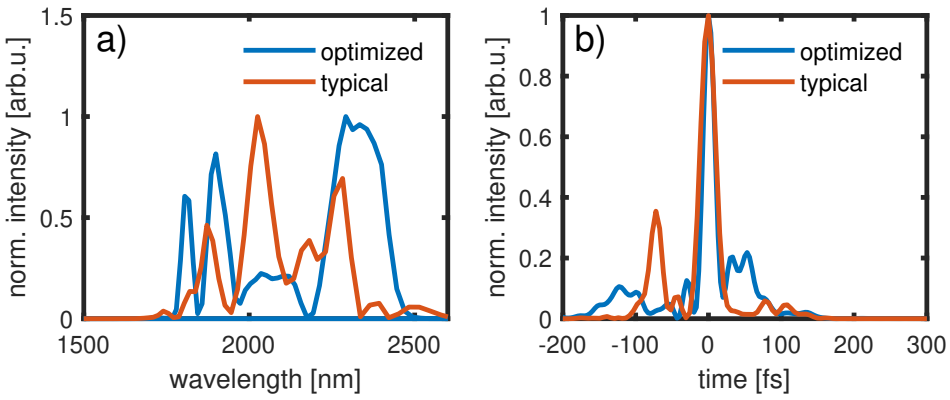

Figure 4.14: Results of the SHG-FROG measurements on the compressed SWIR-output after amplification to 4 mJ in two 1.2 mm LNB-crystal placed close together. The results for the best compression achieved after careful alignment are depicted in blue. An example for the results typically achievable on a day to day basis is depicted in red. a) Shows the retrieved spectra. b) Shows the reconstructed temporal profile of the compressed pulses.

approach. However, without taking special care when aligning the third OPA stage, the pulse duration of the main pulse increases to $\sim$ 24 fs and a large satellite pulse with 35 % of the intensity of the main pulse emerges as can be seen from the red curve in 4.14 b). The compressibility of the pulses in this approach is very sensitive to the noncollinearity angle between the pump and seed pulse and the individual phase matching conditions in the two crystals. These two parameters however, are subject to drifts on longer time scales. The spectra, however, are strongly modulated and the achievable output powers are equivalent for both pulses displayed in Fig. 4.14. Thus, the alignment of the OPA stage has to be optimized with regard to FROG measurements which makes the process time consuming and thus unsuitable for a long-term-stable operation. To solve this issue, it would be necessary to implement a beam pointing stabilization for both the signal and the pump beam. Additionally, a crystal mount would be required which allows for close proximity between the crystals while also facilitating individual adjustment of their phase matching angles. I note here, that the 2.6-2.8-cycle duration achieved directly from the OPA output using the double and single crystal approach, respectively, is not short enough to allow for amplitude gating. Therefore, the demonstrated SWIR-source will be extended by an additional nonlinear compression stage based on a hollow-core fiber in the future to enable the generation of sub 1.5 cycle pulses. Therefore, the cleaner temporal profile and higher pulse energy achievable using the single crystal approach is preferable.

4.6 Carrier-Envelope Phase Stability

A stable carrier-envelope phase is one of the key features of the laser system described in this chapter, as it is necessary for isolated attosecond pulse generation via amplitude- or polarization-gating [130, p. 47 ff] and allows for the study of field-sensitive effects in SXR-pump-probe spectroscopy experiments. This chapter describes active CEP-stabilization mechanisms and the measurement devices used in the demonstrated OPCPA-source before discussing the results achieved after amplification of the SWIR-pulses to multi-mJ energies.

The concept for achieving a highly stable CEP of the output pulses used in this setup, relies on the passively CEP stable seed generation, a CEP preserving amplification and an active slow-loop CEP control. This active component requires a device to measure the relative CEP and to generate a feedback signal for the piezo mirror (PM in Fig. 4.4) in the seed generation setup.

Typically, f-2f-interferometers are used to measure the relative CEP fluctuations by recording the spectral interference fringes that form when a pulse is spatio-temporally overlapped with its second harmonic (see Sec. 2.7.2). However, since the bandwidth of the SWIR pulses is not octave spanning such a device would require additional nonlinear spectral broadening associated with intensity-to-phase-noise coupling and pointing-to-phase-noise coupling. While not octave spanning, the large spectral bandwidth of this OPCPA-setup provides a promising alternative as it allows for spectral overlap between the third and fourth harmonic of the SWIR-pulses. Thus, a collinear 3f-4f-interferometer can be used to observe the spectral fringes emerging from interference between a surface third harmonic (THG). The 4th harmonic is generated from by a cascaded SHG process in two subsequent BBO crystals. This approach avoids the additional phase noise introduced by a bulk filamentation nonlinear broadening stage, which is known for its strong intensity-to-phase-noise and pointing-to-phase-noise coupling [131, 132].

To investigate the differences between the different types of measurement devices, two collinear 3f-4f-interferometers and one noncollinear f-2f-interferometer were built. In order to evaluate the performance of the collinear 3f-4f-interferometer in comparison to the noncollinear f-2f-interferometer the output of the second OPA stage was actively stabilized using one of the collinear 3f-4f-interferometers while the remaining 3f-4f-interferometer and the f-2f-interferometer were used for out-of-loop measurements. The superior performance of the collinear interferometer geometry in general is evident from Fig. 4.15. The graph shows the time-evolution of the relative CEP of the output pulses from OPA stage 2 which was retrieved from simultaneous measurements using the three separate detection devices. The relative CEP was recorded for 105 min at an acquisition rate of 4.75 Hz and an integration time of 30 ms. The data depicted in blue was measured in-loop by the collinear 3f-4f-interferometer which generates the error signal for the piezo-driven CEP-control. The data depicted in red and yellow show the results of out-of-loop measurements with the second collinear 3f-4f-interferometer and the noncollinear f-2f-interferometer, respectively. It is apparent from Fig. 4.15, that the two out-of-loop interferometers perform differently. The measurement using the collinear 3f-4f-interferometer at an rms CEP-noise of 101 mrad exhibits approximately the same noise behaviour observed for the in-loop measurement (100 mrad). The data, however, that was recorded from the noncollinear f-2f-interferometer shows very

distinct deviations.

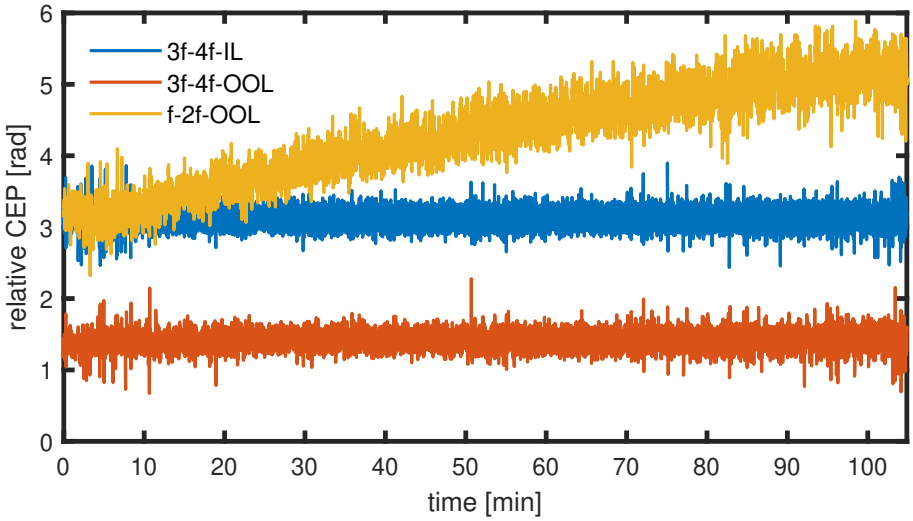

Figure 4.15: Relative CEP simultaneously measured with a collinear 3f-4f-interferometer which is used for active stabilization (in-loop), a collinear 3f-4f interferometer (out-of-loop) and a noncollinear f-2f-interferometer (out-of-loop). The rms fluctuations of the relative CEP during the 105 min measurement times amount to 100 mrad for the in-loop-measurement, 101 mrad for the out-of-loop measurement using the collinear 3f-4f-interferometer and 665 mrad for the out-of-loop measurement using the noncollinear f-2f-interferometer.

The slow drift visible in the relative CEP measured by the f-2f device can be attributed to the noncollinear nature of the interferometer which leads to a slow phase shift inbetween the two arms of the interferometer due to the slow drift of the input beam position. However, the f-2f-interferometer also exhibits larger noise on short time scales, which manifests itself in the larger width of the data curve for the f-2f-interferometer. To examine this effect in more detail, Fig. 4.16 a) shows the first 6 min of the retrieved relative CEP curve displayed in Fig. 4.15. It is apparent from the CEP-curves, that the slow CEP-drift observed for the data recorded with the noncollinear f-2f-interferometer over the full 105 min is negligible in the 6 min time interval. However, faster fluctuations in the retrieved CEP values can be observed.

The probability distribution for the phase values in the 6 min time interval is displayed in Fig. 4.16 b). For the sake of clarity, the mean value of the histograms has been shifted to 0 for the in-loop-measurement, 1 for the out-of-loop-measurement using the collinear 3f-4f-device and 2 for the out-of-loop-measurement using the noncollinear f-2f-device. As the measurements in principle cannot acquire absolute phase values, the position on the phase axis is anyways inherently arbitrary. The data from the measurement using the f-2f-device obviously has a larger probability spread for its phase values and thus shows larger rms fluctuations. The relative CEP measured with the two 3f-4f-interferometers, however, show good stability performance with 91 mrad and 94 mrad rms CEP-noise during the 6 min time interval for the in-loop and out-of-loop measurement, respectively. Notably, the data from the 3f-4f-devices exhibit hardly any deviation between the in- and out-of-loop measurements. This is not true for the data set acquired by the f-2f-device. Here, the rms CEP-fluctuations retrieved from the measurement amount to 158 mrad, showing a 71 % increase in the

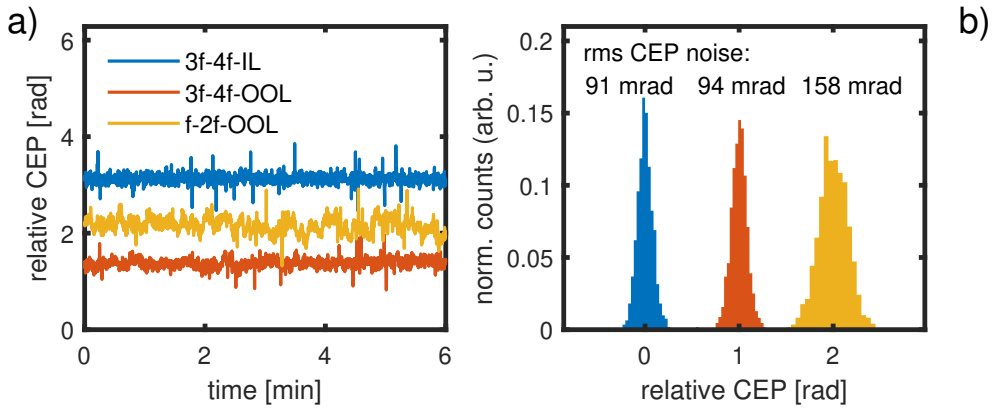

Figure 4.16: a) First 6 min of the relative CEP measurement displayed in Fig. 4.15. On this time scale, the phase drift due to the noncollinearity of the f-2f-interferometer is negligible and residual deviations in the recorded phase fluctuations from the in-loop-measurements are due to the intensity- and pointing-noise-to-phase-noise coupling. b) Histograms showing the probability spread for a measurement value recorded by the respective measurement device. In this 6 min time interval, the rms CEP noise amounts to 91 mrad for the in-loop-measurement, 94 mrad for the out-of-loop-measurement recorded with the collinear 3f-4f-interferometer and 158 mrad for the data recorded with the noncollinear f-2f-interferometer.

rms noise caused solely by detection-noise of the noncollinear f-2f-device, even on time scales where interferometric drifts in the device are negligible. This increased short-term-noise indicates the additional detection noise due to intensity- and pointing-to-phase-noise coupling prevalent in bulk filamentation. Therefore, using a 3f-4f-device improves the general CEP-stability of the SWIR-output and allows for a more accurate out-of-loop monitoring.

The relative CEP of the pulses measured by this in-loop 3f-4f-interferometer is used to generate an error signal for the active piezo mirror in the seed generation setup. A phase shift of the pump light relative to the signal beam directly translates into a shift in the CEP of the SWIR pulses generated in the DFG process [106]. For the characterization of the CEP stability achievable with this laser system, the second collinear 3f-4f-interferometer is used for out-of-loop measurements. Fig. 4.17 a) and b) show the CEP-fringe-traces simultaneously recorded by the in-loop and out-of-loop 3f-4f-interferometers respectively. The retrieved relative CEP values of the SWIR output retrieved from both data sets are displayed in Fig. 4.17 c). The measurements were taken while driving OPA stage 3 with 390 W of pump power in a double LNB crystal configuration. The total rms CEP fluctuations during the $\sim$ 75 in recording time amount to 91 mrad for the in-loop measurement and 92 mrad for the out-of-loop measurement.

Fig. 4.17 clearly shows that the slow-loop CEP control is capable to efficiently suppress slow CEP changes due to interferometric path length changes in the seed generation setup. I note that single shot detection of the relative CEP cannot be achieved here due to the limited data acquisition rate of spectrometers used to record the spectral interference fringes encoding the relative CEP. For the data shown in Fig. 4.17 the spectrometer was integrating for 20 ms per sample, corresponding to 200 laser shots of the 10 kHz laser, thus limiting us to the detection of fluctuations below 25 Hz. Faster fluctuations, however, should not be present due to the passively

CEP stable nature of the seed generation. A remaining noise source which caused the rare phase jumps that can be seen in Fig. 4.17 c), was identified to be the laser beam pointing stabilization after the compressor for the 1030 nm pump light. The device was occasionally over compensating pointing fluctuations and caused a phase shift too fast for the slow-loop-CEP stabilization to follow. It is evident from Fig. 4.17 d) that the noise observed in the out-of-loop measurement significantly exceeds the in-loop-measurement only at frequencies below 0.01 Hz. This might be caused by minor phase changes in the measurement devices due to thermal drifts of the beam position and detection setup itself which are compensated by the feedback-loop in the in-loop but not in the out-of-loop-measurement.

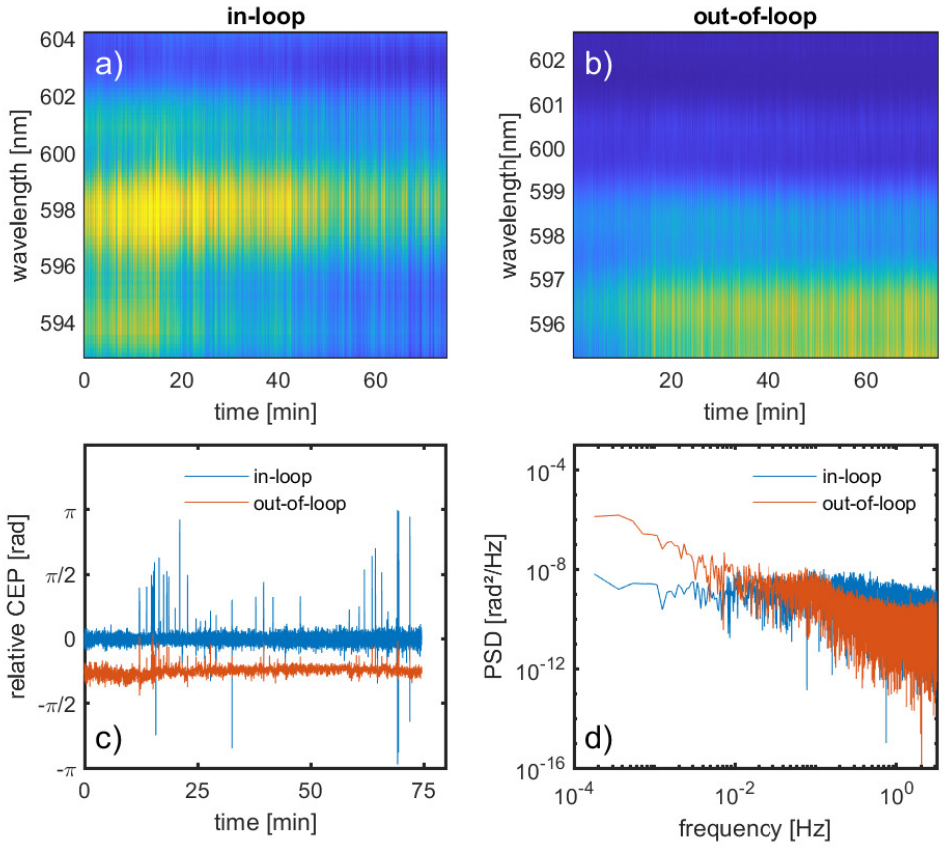

Figure 4.17: Results of two simultaneously acquired measurements of the relative CEP of the output pulses from OPA stage 3 using two collinear 3f-4f-interferometers. The retrieved relative CEP of the in-loop device was used to stabilize the CEP during the measurement while the out-of-loop device was used to just measure the CEP without connection to the feedback-loop. a) and b) show the recorded spectral fringes for the in-loop and out-of-loop measurement, respectively. c) Retrieved relative CEP for the in-loop (red) and out-of-loop (blue) measurement. The rms CEP noise during the approximately 75 min measurement time amounts to 91 mrad (in-loop) and 92 mrad (out-of-loop). The occasional phase jumps are caused by the active pointing stabilization system d) Power spectral density of the CEP-noise in-loop (red) and out-of-loop (blue), revealing a very similar noise profile for both in- and out-of-loop measurements.

4.7 Conclusion

The demonstrated laser system achieves, to the best of the authors knowledge, the highest average power among few-cycle CEP-stable SWIR-OPA light sources. Its unique combination of 5.1 mJ pulse energy, $\leq$ 20 fs pulse duration and excellent power stability with 0.8 % average power fluctuations make this setup an ideal choice for advanced attosecond spectroscopy experiments. The high power SWIR output pulses with sub-100 mrad carrier-envelope-phase noise will allow for the generation of isolated attosecond with photon energies well into the soft-X-ray regime at a repetition rate of 10 kHz

The broadband, high power amplification was only achievable by carefully managing the thermal loads throughout the setup and by avoiding nonlinear lenses emerging due to the high peak power of the pump beam. Utilizing LNB in the third OPA stage is one key aspect in for broadband high power amplification. The material combines a low absorption at the involved wavelength ranges with a high effective second-order nonlinearity and large acceptance bandwidth. Therefore, the achievable output performance exceeds that of amplifiers relying on other crystals such as YCOB. The average power stability of the OPCPA-system benefits from the compact design of the seed generation setup and the use of active beam pointing stabilization devices. The excellent CEP-stability was achieved by combining the passive CEP stabilization offered by the DFG process with an active slow-loop drift-compensation. The active CEP stabilization setup relies on the precise measurement of the relative CEP by highly accurate 3f-4f-interferometers developed as part of this thesis. A low-loss pulse compression by bulk material compression is enabled by pre-compensating the TOD accumulated throughout the setup inbetween the seed-generation and power-amplification stages. Further spectral broadening by self-phase modulation in multi-pass cells [133], arrays of thin plates [134] or hollow core fibers [135] and compression close to single-cycle duration has proven to be possible for similar pulses [133, 134, 135, 136, 137, 138] and may be implemented for this setup in the future. Scaling the pulse energy beyond the 5.1 mJ of OPA stage 3 is possible, making use of the full 1 kW potential output power of the Yb:YAG pump laser. However, this requires substantial parts of the OPCPA setup to be operated under vacuum conditions to avoid nonlinear lensing in air. Alternatively, the repetition rate of the OPCPA can be increased to achieve higher output power while keeping the pulse energies stable. Operating the OPCPA at up to 20 kHz has already been tested for the seed generation setup. Extending this repetition rate increase to the power amplification stages, however, remains challenging due to the significant increase of thermal load in the setup. The high repetition rate of the multi-mJ OPCPA allows for short measurement times and observation of rare events which would otherwise be hidden by noise. This OPCPA setup will be used as a front-end for an attosecond beamline combining the attosecond time resolution achievable with HHG sources with photon cutoff energies in the water w. Therefore, it will allow for experiments and applications in a variety of fields ranging from AMO physics, over chemical and material sciences, to biological applications.

Chapter 5

Summary and Outlook

In this work, two laser systems meant for driving SXR attosecond experiments were demonstrated. The first setup based on a nonlinear regenerative Yb:YAG thin-disk amplifier was able to achieve 2 mJ pulse energies at 100 kHz repetition rate with sub-200 fs pulse durations but the CEP of the pulses could not be stabilized. The CEP distortion mechanisms in the nonlinear regenerative amplifier have been thoroughly investigated revealing the nonlinear interactions inside the laser resonator to be the main source of additional CEP-noise. While CEP-stability could not be achieved for the developed light source, the investigation of the phase distortion mechanisms provides valuable insights for future development projects on high power, high energy, CEP-stable Yb:YAG sources. Despite the unstable CEP, the high pulse energy, short duration for an Yb:YAG-amplifier and good pulse energy stability make this laser system interesting for applications. The pulses from this source were compressed to below 10 fs duration in two nonlinear compression stages based on a gas-filled multi-pass-cell and a stretched hollow-core fiber and used to drive an intra-pulse DFG setup for generating highly-CEP-stable SWIR-pulses (not part of this work). This approach, however, is not capable of achieving CEP-stable pulses with multi-mJ energies.

While CEP-stability could not be achieved by direct amplification of CEP-stable pulses in an Yb:YAG-amplifier, the high pulse energy and output power achievable by such systems can still be utilized in generating ultrafast CEP-stable pulses. In the second laser system developed in the scope of this work, a high power, 10 kHz repetition rate CPA-based regenerative Yb:YAG thin disk amplifier delivering pulses compressible to 1.2 ps duration with up to 550 W of average power has been used to drive a high power self-seeded SWIR-OPCPA setup. The passively CEP-stable seed generated in a DFG process is amplified in three consecutive OPA stages to an average power of up to 51 W, making this OPCPA-setup, to the best of the authors knowledge, the SWIR-OPCPA source for CEP-stable few-cycle pulses providing the highest average power.

The main amplifier can potentially deliver more than 1 kW of output power of which 530 W are used up to now. While increasing the output power of the pump source would require implementing some changes in the main power amplifier resonator, the overall required changes to the setup would be minor. Power scaling of this OPCPA setup by exploiting the full potential of the pump source is possible in two different ways. The increase in the available pump power can be used in the third OPA stage to achieve higher output powers. However, the high peak power of the

pump pulses is already a problem causing self-focusing and damage to optics in the setup. Furthermore, the already large beam size in the setup does not allow for compensating much higher peak intensities by further beam size scaling. Therefore, this power scaling approach requires operating the high power parts of the setup under vacuum conditions, making substantial changes to the setup such as the implementation of vacuum chambers necessary.

The second approach for scaling the output power of the SWIR-OPCPA-setup relies not on an increase of peak power but repetition rate. The main amplifier is capable of operating at repetition rates up to 20 kHz, potentially allowing for a 100 % increase in output power while keeping the peak power constant. This approach has successfully been tested operating the OPCPA-setup up to OPA stage 1 at 20 kHz repetition rate, achieving similar results in terms of SWIR pulse energy as compared to the 10 kHz case. However, operating the power amplification stages at higher repetition rates remains challenging due to the drastic increase of thermal load on the setup. The significantly stronger thermal air currents in the box and the large beam sizes in the setup might prohibit stable operation of the laser system at such power levels. The solution to this issue might also require the implementation of vacuum chambers to avoid instabilities. Nonetheless, this approach is promising for increasing the achievable output power and be implemented by a step-wise increase of the repetition rate up to the limit set by thermal load and system stability criteria.

Further improvements of the OPCPA-setup could be achieved by introducing a phase-front-tilt to the pump beam to match the phase fronts of the pump and signal beam in the noncollinear geometry. This can result in an improved efficiency and homogeneity of the amplification process [66]. Additionally, employing a flat-top pump beam profile in space and time could result in significant improvements of the conversion efficiency [139]. Such pulses would also reduce the systems susceptibility to self-focusing and laser induced damage and thus allow for higher pump pulse energies.

This setup combines a pulse energy of up to 5.1 mJ, pulse durations of 20 fs and excellent stability with below 100 mrad CEP and only 0.8 % rms average power fluctuations. Therefore, it already constitutes an excellent driving source for HHG and isolated attosecond pulse generation with SXR-photon energies in the water window.

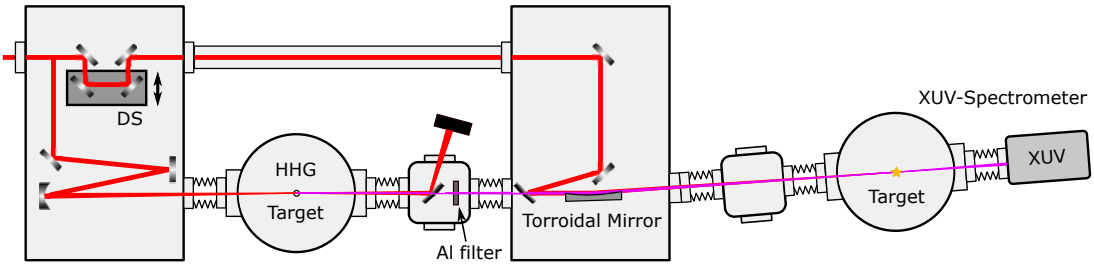

Figure 5.1: Schematic drawing of the beamline for attosecond pump probe spectroscopy with isolated SXR-attosecond pulses in the water-window energy region which will be driven by the high energy SWIR-OPCPA source developed in the scope of this work.

The attosecond beamline, depicted in Fig 5.1, has been set up and first tests on HHG using the output of the OPCPA-setup were conducted to align the setup and detection devices. Fig. 5.2 shows the ceramic HHG-target tube with a 300 μm hole and 200 mbar of argon. The plasma jet extending from the holes in the tube in both

directions is clearly visible, however, up to now, no HHG-spectrum generated from this setup could be recorded. This might be partially due to the lower generation efficiency at SWIR wavelengths as compared to Ti:sapphire driven systems and the thickness of the aluminum filters used to remove the SWIR driver after the HHG-process limiting the intensity reaching the detection electronics at the end of the beam line. Thus proper alignment of the beamline is challenging.

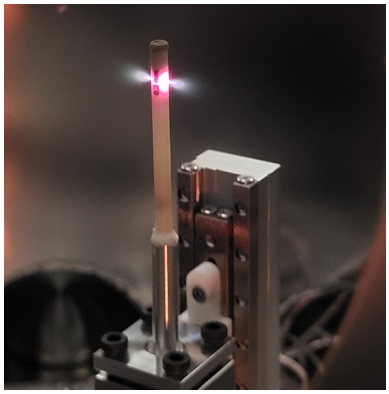

Figure 5.2: Ceramic HHG target tube with an 0.3 mm hole. The argon pressure inside the target is $\sim$ 200 mbar. The target is illuminated by 20 fs SWIR pulses with $\sim$ 1 mJ of pulse energy, generating plasma jets extending from the holes of the target tube along the beam propagation axis in both directions by ionizing the target gas.

Previous work on HHG using SWIR-pulses centered at 2 μm wavelength suggests that a better HHG-efficiency could be achieved by using higher peak intensities [119, p. 45ff] which could be reached with shorter pulse durations. Additionally, the $\sim$ 2.8-cycle pulse duration achievable from the OPCPA-setup is not short enough to allow for isolated attosecond pulse generation using amplitude gating techniques. Thus, further nonlinear compression of the output pulses will be required. To achieve compression of the SWIR-pulses to below 10 fs, a HCF-based nonlinear compression stage will be implemented before sending the beam to the attosecond beamline. With pulse durations close to a single cycle, the efficiency of the HHG can be increased and isolated attosecond generation by amplitude gating becomes feasible. Many applications such as peripheral diagnostics like CEP-phase meters [140] or experimental pump beams for the planned SXR-pump-probe-experiments benefit from shorter durations but do not require the full power of the OPCPA-setup. For such applications it might be preferable to compress only a split fraction of the available SWIR power. A useful approach for nonlinear compression of low power beams is nonlinear broadening in thin plates [138]. The feasibility of this approach for the demonstrated SWIR-source has been investigated in a test setup based on TiO_2.

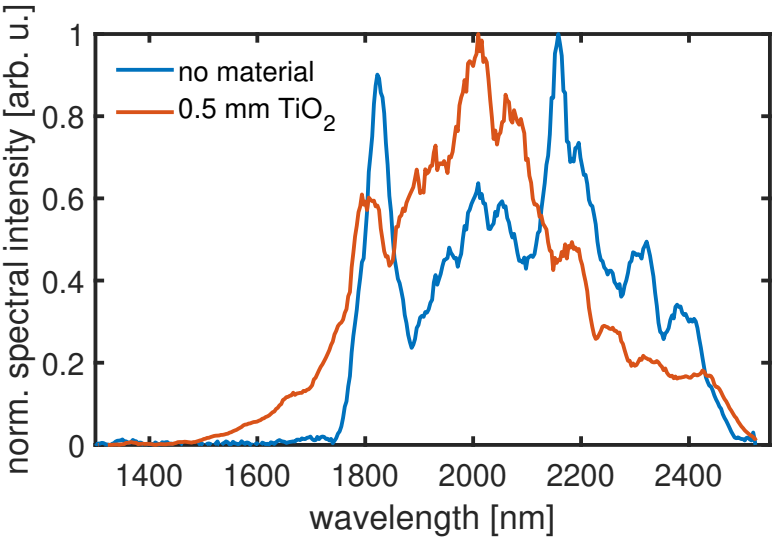

Figure 5.3: Spectra of the SWIR-output of the OPCPA setup. Depicted in blue is the spectrum directly from the third OPA stage. Approximately 750 mW of the output power were focused into an 0.5 mm thick TiO_2 plate for nonlinear broadening. The spectrum of the pulses after the nonlinear broadening stages is depicted in red showing a significant increase in bandwidth with spectral components down to 1400 nm and a decrease in Fourier-transform-limited pulse duration from $\sim$ 17 fs to below 14 fs.

Approximately 750 mW of the output power were focused into an 0.5 mm thick TiO_2 plate for nonlinear broadening. The spectra of the pulses before and after the nonlinear broadening stages are shown in Fig. 5.3 depicted in blue and red, respectively. A comparison between the fundamental and broadened spectra shows a significant increase in bandwidth by the nonlinear broadening stage, generating spectral components down to 1400 nm and a decreasing the Fourier-transform-limited pulse duration from $\sim$ 17 fs to below 14 fs. A higher compression factor with pulse durations close to single cycles may be achievable by adding additional thin plates. This technique can be utilized for nonlinear compression blow 20 fs for low power applications such as the SWIR-pump beam in the experimental beamline. However, the damage threshold of the material and nonlinear distortions of the beam quality when placed in the wrong distance to the focal spot [138, 141] make this broadening approach unfeasible for nonlinear compression of the full power available from the OPCPA setup.

Bibliography

[1] Albert Einstein. "Zur Quantentheorie der Strahlung". In: *Phys Zeit* 18 (1917), p. 121.

[2] James P Gordon, Herbert J Zeiger, and Charles H Townes. "Molecular microwave oscillator and new hyperfine structure in the microwave spectrum of N H 3". In: *Physical Review* 95.1 (1954), p. 282.

[3] TH Maiman. "Stimulated optical radiation in ruby". In: *Nature* 4736 (1960), pp. 493–494.

[4] Qian Peng et al. "Lasers in medicine". In: *Reports on Progress in Physics* 71.5 (2008), p. 056701.

[5] Franz Hillenkamp. *Lasers in biology and medicine*. Vol. 34. Springer Science & Business Media, 2013.

[6] Benjamin P Abbott et al. "Observation of gravitational waves from a binary black hole merger". In: *Physical review letters* 116.6 (2016), p. 061102.

[7] David L Andrews. *Lasers in chemistry*. Springer Science & Business Media, 2012.

[8] Marta Castillejo, Paolo M Ossi, Leonid Zhigilei, et al. *Lasers in materials science*. Springer, 2014.

[9] William M Steen and Jyotirmoy Mazumder. *Laser material processing*. springer science & business media, 2010.

[10] M Arumugam. "Optical fiber communication—An overview". In: *Pramana* 57 (2001), pp. 849–869.

[11] Charles W Gwyn et al. "Extreme ultraviolet lithography". In: *Journal of Vacuum Science & Technology B: Microelectronics and Nanometer Structures Processing, Measurement, and Phenomena* 16.6 (1998), pp. 3142–3149.

[12] eg PA Franken et al. "Generation of optical harmonics". In: *Physical review letters* 7.4 (1961), p. 118.

[13] Joseph Anthony Giordmaine and Robert C Miller. "Tunable coherent parametric oscillation in $LiNbO_3$ at optical frequencies". In: *Physical Review Letters* 14.24 (1965), p. 973.

[14] Donna Strickland and Gerard Mourou. "Compression of amplified chirped optical pulses". In: *Optics communications* 55.6 (1985), pp. 447–449.

[15] Peter F Moulton. "Spectroscopic and laser characteristics of Ti: Al 2 O 3". In: *JOSA B* 3.1 (1986), pp. 125–133.

[16] Peter F Moulton. “Spectroscopic and laser characteristics of Ti: Al 2 O 3”. In: *JOSA B* 3.1 (1986), pp. 125–133.

[17] Robert A Crowell et al. “Ultrafast processes in radiation chemistry”. In: *Radiation Physics and Chemistry* 70.4-5 (2004), pp. 501–509.

[18] Markus Braun, Peter Gilch, and Wolfgang Zinth. *Ultrashort laser pulses in biology and medicine*. Springer Science & Business Media, 2008.

[19] A McPherson et al. “Studies of multiphoton production of vacuum-ultraviolet radiation in the rare gases”. In: *JOSA B* 4.4 (1987), pp. 595–601.

[20] A L’huillier. “Multiphoton ionization and harmonic generation under strong lasers”. In: *OSA Annual Meeting*. Optica Publishing Group. 1988, MY2.

[21] Paul B Corkum. “Plasma perspective on strong field multiphoton ionization”. In: *Physical review letters* 71.13 (1993), p. 1994.

[22] Maciej Lewenstein et al. “Theory of high-harmonic generation by low-frequency laser fields”. In: *Physical Review A* 49.3 (1994), p. 2117.

[23] Pierre-Marie Paul et al. “Observation of a train of attosecond pulses from high harmonic generation”. In: *Science* 292.5522 (2001), pp. 1689–1692.

[24] M Hentschel et al. “Attosecond metrology”. In: *Nature* 414.6863 (2001), pp. 509–513.

[25] Ferenc Krausz. “The birth of attosecond physics and its coming of age”. In: *Physica Scripta* 91.6 (2016), p. 063011.

[26] Thomas Gaumnitz et al. “Streaking of 43-attosecond soft-X-ray pulses generated by a passively CEP-stable mid-infrared driver”. In: *Optics express* 25.22 (2017), pp. 27506–27518.

[27] P áB Corkum and Ferenc Krausz. “Attosecond science”. In: *Nature physics* 3.6 (2007), pp. 381–387.

[28] Manish Garg et al. “Multi-petahertz electronic metrology”. In: *Nature* 538.7625 (2016), pp. 359–363.

[29] Johannes Schötz et al. “Perspective on petahertz electronics and attosecond nanoscopy”. In: *ACS photonics* 6.12 (2019), pp. 3057–3069.

[30] Huabao Cao, Roland S Nagymihaly, and Vladimir Chvykov. “Cross thin slab kW-class Ti: Sapphire amplifiers”. In: *Laser Physics* 29.6 (2019), p. 065802.

[31] Vladimir Chvykov, John Nees, and Karl Krushelnick. “Transverse amplified spontaneous emission: The limiting factor for output energy of ultra-high power lasers”. In: *Optics Communications* 312 (2014), pp. 216–221.

[32] Thomas Nubbemeyer et al. “1 kW, 200 mJ picosecond thin-disk laser system”. In: *Optics letters* 42.7 (2017), pp. 1381–1384.

[33] P Russbueldt et al. “Compact diode-pumped 1.1 kW Yb: YAG Innoslab femtosecond amplifier”. In: *Optics letters* 35.24 (2010), pp. 4169–4171.

[34] G Bonati et al. “1.53 kW from a single Yb-doped photonic crystal fiber laser”. In: *Photonics West, San Jose, Late Breaking Developments, Session* 5709 (2005).

[35] Joerg Koerner et al. “Measurement of temperature-dependent absorption and emission spectra of Yb: YAG, Yb: LuAG, and Yb: CaF 2 between 20 C and 200 C and predictions on their influence on laser performance”. In: *JOSA B* 29.9 (2012), pp. 2493–2502.

[36] Di Sun et al. “Numerical and experimental analysis of Yb: YAG thin disk regenerative amplifier”. In: *IEEE Photonics Journal* 13.3 (2021), pp. 1–9.

[37] Young-Gyun Jeong et al. “Direct compression of 170-fs 50-cycle pulses down to 1.5 cycles with 70% transmission”. In: *Scientific reports* 8.1 (2018), p. 11794.

[38] Anne-Lise Viotti et al. “Few-cycle pulse generation by double-stage hybrid multi-pass multi-plate nonlinear pulse compression”. In: *Optics Letters* 48.4 (2023), pp. 984–987.

[39] J Rothhardt et al. “High Average Power Near-Infrared Few-Cycle Lasers”. In: *Laser & Photonics Reviews* 11.4 (2017), p. 1700043.

[40] Eugene Hecht. “Optik. 5., verbesserte Auflage”. In: *München, Ouldenbourg Wissenschaftsverlag GmbH* (2009).

[41] Robert W Boyd. *Nonlinear optics*. 3rd ed. Academic press, 2020.

[42] Georg A Reider. *Photonik: eine Einführung in die Grundlagen*. Springer-Verlag, 2013.

[43] Norman Hodgson and Horst Weber. *Laser Resonators and Beam Propagation: Fundamentals, Advanced Concepts, Applications*. Vol. 108. Springer, 2005.

[44] Orazio Svelto, David C Hanna, et al. *Principles of lasers*. 4. Vol. 1. Springer, 2010.

[45] Anthony E Siegman. “New developments in laser resonators”. In: *Optical resonators*. Vol. 1224. Spie. 1990, pp. 2–14.

[46] R Holzwarth et al. “Optical frequency synthesizer for precision spectroscopy”. In: *Physical review letters* 85.11 (2000), p. 2264.

[47] David J Jones et al. “Carrier-envelope phase control of femtosecond mode-locked lasers and direct optical frequency synthesis”. In: *Science* 288.5466 (2000), pp. 635–639.

[48] Michael Chini, Kun Zhao, and Zenghu Chang. “The generation, characterization and applications of broadband isolated attosecond pulses”. In: *Nature Photonics* 8.3 (2014), pp. 178–186.

[49] Peter Hansinger et al. “Refractive index dispersion measurement using carrier-envelope phasemeters”. In: *New Journal of Physics* 19.2 (2017), p. 023040.

[50] Chengquan Li et al. “Mechanism of phase-energy coupling in f-to-2f interferometry”. In: *Applied optics* 48.7 (2009), pp. 1303–1307.

[51] Clemens Hönninger et al. “Ultrafast ytterbium-doped bulk lasers and laser amplifiers”. In: *Applied Physics B* 69 (1999), pp. 3–17.

[52] Jiexi Zuo and Xuechun Lin. “High-Power Laser Systems”. In: *Laser & Photonics Reviews* 16.5 (2022), p. 2100741.

[53] Pavel Sidorenko, Walter Fu, and Frank Wise. "Nonlinear ultrafast fiber amplifiers beyond the gain-narrowing limit". In: *Optica* 6.10 (2019), pp. 1328–1333.

[54] Peter Russbueldt et al. "Innoslab amplifiers". In: *IEEE Journal of Selected Topics in Quantum Electronics* 21.1 (2014), pp. 447–463.

[55] Clara J Saraceno et al. "The amazing progress of high-power ultrafast thin-disk lasers". In: *Journal of the European Optical Society-Rapid Publications* 15.1 (2019), pp. 1–7.

[56] Jinliang Han et al. "High-power narrow-linewidth diode laser based on external cavity feedback technology for Yb: YAG pumping". In: *Japanese Journal of Applied Physics* 61.12 (2022), p. 120903.

[57] Anthony E Siegman. *Lasers*. University science books, 1986.

[58] Adolf Giesen and Jochen Speiser. "Fifteen years of work on thin-disk lasers: results and scaling laws". In: *IEEE Journal of selected topics in quantum electronics* 13.3 (2007), pp. 598–609.

[59] Robert R Alfano. *The supercontinuum laser source: the ultimate white light*. Springer Nature, 2023.

[60] Thibaut Sylvestre et al. "Recent advances in supercontinuum generation in specialty optical fibers". In: *JOSA B* 38.12 (2021), F90–F103.

[61] P St J Russell et al. "Hollow-core photonic crystal fibres for gas-based nonlinear optics". In: *Nature Photonics* 8.4 (2014), pp. 278–286.

[62] F Silva et al. "Multi-octave supercontinuum generation from mid-infrared filamentation in a bulk crystal". In: *Nature communications* 3.1 (2012), p. 807.

[63] N Bloembergen. "The influence of electron plasma formation on superbroadening in light filaments". In: *Optics Communications* 8.4 (1973), pp. 285–288.

[64] Maximilian Bradler. "Bulk continuum generation: the ultimate tool for laser applications and spectroscopy". PhD thesis. lmu, 2014.

[65] MV Hobden. "Phase-matched second-harmonic generation in biaxial crystals". In: *Journal of Applied Physics* 38.11 (1967), pp. 4365–4372.

[66] Cristian Manzoni and Giulio Cerullo. "Design criteria for ultrafast optical parametric amplifiers". In: *Journal of Optics* 18.10 (2016), p. 103501.

[67] R Dabu. "Very broad gain bandwidth parametric amplification in nonlinear crystals at critical wavelength degeneracy". In: *Optics Express* 18.11 (2010), pp. 11689–11699.

[68] VV Lozhkarev et al. "Study of broadband optical parametric chirped pulse amplification in a DKDP crystal pumped by the second harmonic of a Nd: YLF laser". In: *LASER PHYSICS-LAWRENCE-* 15.9 (2005), p. 1319.

[69] Rick Trebino. *Frequency-Resolved Optical Gating: The Measurement of Ultrashort Laser Pulses: The Measurement of Ultrashort Laser Pulses*. Springer Science & Business Media, 2000.

[70] Rick Trebino and Daniel J Kane. "Using phase retrieval to measure the intensity and phase of ultrashort pulses: frequency-resolved optical gating". In: *JOSA A* 10.5 (1993), pp. 1101–1111.

[71] Victor Wong and Ian A Walmsley. "Phase retrieval in time-resolved spectral phase measurement". In: *Generation, Amplification, and Measurement of Ultrashort Laser Pulses II*. Vol. 2377. SPIE. 1995, pp. 178–186.

[72] Tibor Wittmann et al. "Single-shot carrier–envelope phase measurement of few-cycle laser pulses". In: *Nature Physics* 5.5 (2009), pp. 357–362.

[73] M Möller et al. "Precise, real-time, single-shot carrier-envelope phase measurement in the multi-cycle regime". In: *Applied Physics Letters* 99.12 (2011).

[74] Nay Oo and Woon-Seng Gan. "On harmonic addition theorem". In: *International Journal of Computer and Communication Engineering* 1.3 (2012), p. 200.

[75] Tamas Nagy et al. "Generation of three-cycle multi-millijoule laser pulses at 318 W average power". In: *Optica* 6.11 (2019), pp. 1423–1424.

[76] G Fan et al. "70 mJ nonlinear compression and scaling route for an Yb amplifier using large-core hollow fibers". In: *Optics Letters* 46.4 (2021), pp. 896–899.

[77] Moritz Ueffing et al. "Nonlinear pulse compression in a gas-filled multipass cell". In: *Optics letters* 43.9 (2018), pp. 2070–2073.

[78] Marc Hanna et al. "Nonlinear optics in multipass cells". In: *Laser & Photonics Reviews* 15.12 (2021), p. 2100220.

[79] Moritz Ueffing. "Direct amplification of femtosecond pulses". PhD thesis. LMU München, 2018.

[80] Benjamin Dannecker et al. "Exploiting nonlinear spectral broadening in a 400 W Yb: YAG thin-disk multipass amplifier to achieve 2 mJ pulses with sub-150 fs duration". In: *Optics Communications* 429 (2018), pp. 180–188.

[81] Moritz Ueffing et al. "Direct regenerative amplification of femtosecond pulses to the multimillijoule level". In: *Optics letters* 41.16 (2016), pp. 3840–3843.

[82] Sebastian Gröbmeyer et al. "Carrier-Envelope-Offset Frequency Stable 100 W-Level Femtosecond Thin-Disk Oscillator". In: *Laser & Photonics Reviews* 13.3 (2019), p. 1800256.

[83] Steffen Hädrich et al. "Carrier-envelope phase stable few-cycle laser system delivering more than 100 W, 1 mJ, sub-2-cycle pulses". In: *Optics Letters* 47.6 (2022), pp. 1537–1540.

[84] Tamas Nagy, Michael Forster, and Peter Simon. "Flexible hollow fiber for pulse compressors". In: *Applied Optics* 47.18 (2008), pp. 3264–3268.

[85] Giedrius Sinkevicius and Algirdas Baskys. "Investigation of piezoelectric ringing frequency response of beta barium borate crystals". In: *Crystals* 9.1 (2019), p. 49.

[86] Nicholas Karpowicz. *LightWave Explorer*. `https://github.com/NickKarpowicz/LightwaveExplorer`.

[87] Maximilian Seeger et al. "49 W Carrier-Envelope-Phase-Stable Few-Cycle 2.1 μm OPCPA at 10 kHz". In: *Optics Express* (June 2023). DOI: 10.1364/OE.493326.

[88] Stefan Witte and Kjeld SE Eikema. "Ultrafast optical parametric chirped-pulse amplification". In: *IEEE Journal of Selected Topics in Quantum Electronics* 18.1 (2011), pp. 296–307.

[89] Tenio Popmintchev et al. "Bright coherent ultrahigh harmonics in the keV x-ray regime from mid-infrared femtosecond lasers". In: *science* 336.6086 (2012), pp. 1287–1291.

[90] M van Mörbeck-Bock et al. "High average power OPCPA MIR-systems for coherent soft x-ray generation accessing absorption edges of metals". In: *High Power Lasers and Applications*. Vol. 11777. SPIE. 2021, pp. 11–16.

[91] Matthew KR Windeler et al. "High Average Power 106 W, 1.75 μm, 100 kHz Optical Parametric Chirped Pulse Amplifier". In: *CLEO: Applications and Technology*. Optica Publishing Group. 2019, JM1E–3.

[92] Tianli Feng et al. "27 W 2.1 μm OPCPA system for coherent soft X-ray generation operating at 10 kHz". In: *Optics Express* 28.6 (2020), pp. 8724–8733.

[93] Tiago de Faria Pinto et al. "Optical parametric chirped pulse amplifier producing ultrashort 10.5 mJ pulses at 1.55 μm". In: *Optics Express* 27.21 (2019), pp. 29829–29837.

[94] Yuxi Fu, Eiji J Takahashi, and Katsumi Midorikawa. "High-energy infrared femtosecond pulses generated by dual-chirped optical parametric amplification". In: *Optics Letters* 40.21 (2015), pp. 5082–5085.

[95] Giedrius Andriukaitis et al. "90 GW peak power few-cycle mid-infrared pulses from an optical parametric amplifier". In: *Optics letters* 36.15 (2011), pp. 2755–2757.

[96] Kun Zhao et al. "Generation of 120 GW mid-infrared pulses from a widely tunable noncollinear optical parametric amplifier". In: *Optics letters* 38.13 (2013), pp. 2159–2161.

[97] Valentina Shumakova et al. "Multi-millijoule few-cycle mid-infrared pulses through nonlinear self-compression in bulk". In: *Nature communications* 7.1 (2016), p. 12877.

[98] Kyung-Han Hong et al. "Multi-mJ, kHz, 2.1 μm optical parametric chirped-pulse amplifier and high-flux soft x-ray high-harmonic generation". In: *Optics letters* 39.11 (2014), pp. 3145–3148.

[99] Bruno E Schmidt et al. "Frequency domain optical parametric amplification". In: *Nature communications* 5.1 (2014), p. 3643.

[100] Yanchun Yin et al. "High-efficiency optical parametric chirped-pulse amplifier in BiB 3 O 6 for generation of 3 mJ, two-cycle, carrier-envelope-phase-stable pulses at 1.7 μm". In: *Optics letters* 41.6 (2016), pp. 1142–1145.

[101] Yunpei Deng et al. "Carrier-envelope-phase-stable, 1.2 mJ, 1.5 cycle laser pulses at 2.1 μm". In: *Optics letters* 37.23 (2012), pp. 4973–4975.

[102] Jan Heye Buss et al. “High-power OPCPAs at 1450–2400 nm wavelength”. In: *Nonlinear Frequency Generation and Conversion: Materials and Devices XX*. Vol. 11670. SPIE. 2021, pp. 121–130.

[103] Thomas Nubbemeyer et al. “1 kW, 200 mJ picosecond thin-disk laser system”. In: *Optics letters* 42.7 (2017), pp. 1381–1384.

[104] Reimund Martin Kaumanns. “Generation of energetic femtosecond pulses at high average power”. PhD thesis. lmu, 2020.

[105] Sergei G Grechin. “Integral criterion for selecting nonlinear crystals for frequency conversion”. In: *Quantum Electronics* 39.2 (2009), p. 171.

[106] M Neuhaus et al. “10 W CEP-stable few-cycle source at 2 μm with 100 kHz repetition rate”. In: *Optics express* 26.13 (2018), pp. 16074–16085.

[107] Dongxiang Zhang, Yufei Kong, and Jing-yuan Zhang. “Optical parametric properties of 532-nm-pumped beta-barium-borate near the infrared absorption edge”. In: *Optics communications* 184.5-6 (2000), pp. 485–491.

[108] Nobuhiro Umemura, Kentaro Miyata, and Kiyoshi Kato. “New data on the optical properties of BiB3O6”. In: *Optical Materials* 30.4 (2007), pp. 532–534.

[109] David E Zelmon, David L Small, and Dieter Jundt. “Infrared corrected Sellmeier coefficients for congruently grown lithium niobate and 5 mol.% magnesium oxide–doped lithium niobate”. In: *JOSA B* 14.12 (1997), pp. 3319–3322.

[110] P Segonds et al. “Optical characterizations of YCa4O (BO3) 3 and Nd: YCa4O (BO3) 3 crystals”. In: *Optical Materials* 29.8 (2007), pp. 975–982.

[111] Michael M Choy and Robert L Byer. “Accurate second-order susceptibility measurements of visible and infrared nonlinear crystals”. In: *Physical Review B* 14.4 (1976), p. 1693.

[112] Jean-Philippe Fève et al. “Phase-matching measurements and Sellmeier equations over the complete transparency range of KTiOAsO 4, RbTiOAsO 4, and CsTiOAsO 4”. In: *JOSA B* 17.5 (2000), pp. 775–780.

[113] Arlee Smith. *Introduction to SNLO software*. `https://as-photonics.com/products/snlo/`. 2015.

[114] GC Bhar, U Chatterjee, and S Das. “Tunable near-infrared radiation by difference frequency mixing in beta barium borate crystal”. In: *Applied physics letters* 58.3 (1991), pp. 231–233.

[115] AV Cherepakhin et al. “Optical and nonlinear optical properties of orthorhombic BiB3O6”. In: *Optical Materials* 34.5 (2012), pp. 790–792.

[116] M Carrascosa et al. “Understanding light intensity thresholds for catastrophic optical damage in $LiNbO_3$”. In: *Optics Express* 16.1 (2008), pp. 115–120.

[117] P Sen et al. “The effect of MgO doping on optical properties of $LiNbO_3$ single crystals”. In: *Solid state communications* 129.11 (2004), pp. 747–752.

[118] Achut Giree et al. “Numerical study of spatiotemporal distortions in noncollinear optical parametric chirped-pulse amplifiers”. In: *Optics express* 25.4 (2017), pp. 3104–3121.

[119] Clemens Jakubeit. “High harmonic generation using a 2 μm OPCPA”. PhD thesis. lmu, 2019.

[120] Gunnar Arisholm. “General numerical methods for simulating second-order nonlinear interactions in birefringent media”. In: *JOSA B* 14.10 (1997), pp. 2543–2549.

[121] Gunnar Arisholm. “Advanced numerical simulation models for second-order nonlinear interactions”. In: *Laser Optics’ 98: Fundamental Problems of Laser Optics*. Vol. 3685. SPIE. 1999, pp. 86–97.

[122] Gunnar Arisholm and Helge Fonnum. “Simulation System For Optical Science (SISYFOS)–tutorial, version 2”. In: (2021).

[123] Jingui Ma et al. “Origin and suppression of back conversion in a phase-matched nonlinear frequency down-conversion process”. In: *Chinese Optics Letters* 15.2 (2017), p. 021901.

[124] Guan Gui et al. “Strong optical nonlinearities in dispersive dielectric chirped mirrors below the damage threshold”. In: *Laser Science*. Optica Publishing Group. 2020, JW6A–18.

[125] Hélène Krol et al. “Study of laser-induced damage at 2 microns on coated and uncoated ZnSe substrates”. In: *Laser-Induced Damage in Optical Materials: 2006*. Vol. 6403. SPIE. 2007, pp. 382–389.

[126] Jiahui Gu et al. “Random quasi-phase-matching in polycrystalline media and its effects on pulse coherence properties”. In: *Optics Express* 29.5 (2021), pp. 7479–7493.

[127] Zuofei Hong, Han Zhang, and Shaolin Ke. “Efficient Generation of Spectrum-Manipulated Few-Cycle Laser Pulses through Cascaded Dual-Chirped OPA”. In: *International Journal of Molecular Sciences* 22.13 (2021), p. 6887.

[128] AnnMarie L Oien et al. “Efficient, low-threshold collinear and noncollinear β-barium borate optical parametric oscillators”. In: *Optics letters* 22.12 (1997), pp. 859–861.

[129] Jian Wang, Malcolm H Dunn, and Cameron F Rae. “Polychromatic optical parametric generation by simultaneous phase matching over a large spectral bandwidth”. In: *Optics letters* 22.11 (1997), pp. 763–765.

[130] Luis Plaja, Ricardo Torres, and Amelle Zaïr. “Attosecond physics”. In: *Springer Series in Optical Sciences* 177 (2013).

[131] Andrius Baltuska et al. “Phase-controlled amplification of few-cycle laser pulses”. In: *IEEE Journal of Selected Topics in Quantum Electronics* 9.4 (2003), pp. 972–989.

[132] Benjamin Maingot et al. “Spectral coherence properties of continuum generation in bulk crystals”. In: *Optics Express* 30.12 (2022), pp. 20311–20320.

[133] Junyu Qian et al. “Few-cycle mid-infrared laser based on nonlinear self-compression in solid thin plates”. In: *Optics Letters* 46.19 (2021), pp. 5075–5078.

[134] Gaëtan Jargot et al. “Self-compression in a multipass cell”. In: *Optics Letters* 43.22 (2018), pp. 5643–5646.

[135] Pierre Béjot et al. “Mechanism of hollow-core-fiber infrared-supercontinuum compression with bulk material”. In: *Physical Review A* 81.6 (2010), p. 063828.

[136] Vincent Cardin et al. “0.42 TW 2-cycle pulses at 1.8 μ m via hollow-core fiber compression”. In: *Applied Physics Letters* 107.18 (2015), p. 181101.

[137] Pengfei Wang et al. “2.6 mJ/100 Hz CEP-stable near-single-cycle 4 μm laser based on OPCPA and hollow-core fiber compression”. In: *Optics Letters* 43.9 (2018), pp. 2197–2200.

[138] Tamas Nagy, Peter Simon, and Laszlo Veisz. “High-energy few-cycle pulses: post-compression techniques”. In: *Advances in Physics: X* 6.1 (2021), p. 1845795.

[139] Xiao Zou et al. “Three-fold efficiency improvement via temporal and spatial pulse shaping in 3μm OPCPA”. In: *Conference on Lasers and Electro-Optics/Pacific Rim*. Optica Publishing Group. 2017, s2252.

[140] Maximilian Kubullek et al. “Single-shot carrier–envelope-phase measurement in ambient air”. In: *Optica* 7.1 (2020), pp. 35–39.

[141] John E Beetar, Shima Gholam-Mirzaei, and Michael Chini. “Spectral broadening and pulse compression of a 400 μJ, 20 W Yb: KGW laser using a multi-plate medium”. In: *Applied Physics Letters* 112.5 (2018), p. 051102.

Acknowledgements

I'd like to thank Matthias Kling for giving me the opportunity to do research in an amazing environment. I thank Harald Fuest for welcoming me to the group. I thank Marcel Neuhaus and Pawel Wnuk for introducing me to laser physics with optical parametric amplifiers and for being great colleagues. I thank Moritz Ueffing for the breakfast and for teaching me some very valuable lessons. I thank Thomas Nubbemeyer for his great supervision, his guidance and for all the effort he took to make this thesis happen. I thank Johannes Blöchl for the coffee and for always helping me out in times of need. I thank Nicholas Karpowicz for answering my questions again and again and again. I thank Najd for the dates and all the other sweet stuff. I thank Dominik Kammerer for giving me a chance to teach. I thank Hadil Kassab for being a great office mate. I thank Simon Reiger for being a nice colleague who even responded to a mail of mine once upon a time. As I'm writing this in an airplane somewhere above Canada, I'd like to thank the bears for being down there and not up here and the crew of the airplane for getting me where I need to go safely...fingers crossed. I'd also like to thank the reader for dealing with my questionable sense of humor. Finally, there is one person I'd like to thank above all others. Ellen, you made this possible. You made this enjoyable. You made this worth it.